

NASA/CR- 1998 208312

11-92-OR
289720

THE STRUCTURE AND DYNAMICS OF THE SOLAR CORONA

NASA SPACE PHYSICS THEORY CONTRACT NAS5-96081

SECOND YEAR PROGRESS REPORT

Covering the period July 16, 1997 to June 15, 1998

Submitted by:

Zoran Mikić
Principal Investigator
Science Applications International Corporation
10260 Campus Point Drive
San Diego, CA 92121

June 15, 1998

TABLE OF CONTENTS

<u>Section</u>	<u>Page</u>
1. INTRODUCTION.....	1
2. ACHIEVEMENTS	1
2.1. Modeling the Large-Scale Structure of the Corona and Inner Heliosphere.....	1
2.1.1. Coronal Evolution in Response to Changes in Photospheric Magnetic Fields ..	2
2.1.2. Comparison with Eclipse Observations.....	3
2.1.3. MHD Modeling for Whole Sun Month	3
2.1.4. Modeling the Solar Wind.....	7
2.1.5. Simulated Disk and Coronal Emission Images.....	7
2.2 Coronal Mass Ejections.....	8
2.2.1. Emerging Flux as a Trigger for CMEs.....	8
2.3 Three-Dimensional Active Region Modeling.....	8
2.3.1. Interaction of Twisted Coronal Loops	8
2.3.2. Eruption of an Active Region as a Result of Flux Emergence.....	10
2.4 Massively Parallel Computing	10
2.5. Simulation of the MRX Laboratory Reconnection Experiment	12
3. REFERENCES	13
4. PUBLICATIONS SUPPORTED BY CONTRACT NAS5-96081.....	14
APPENDIX: Selected Reprints.....	16

SECOND YEAR PROGRESS REPORT

This report covers technical progress during the second year of the NASA Space Physics Theory contract "The Structure and Dynamics of the Solar Corona," NAS5-96081, between NASA and Science Applications International Corporation, and covers the period July 16, 1997 to June 15, 1998. Under this contract SAIC, the University of California, Irvine (UCI), and the Jet Propulsion Laboratory (JPL), have conducted research into theoretical modeling of active regions, the solar corona, and the inner heliosphere, using the MHD model. During the period covered by this report we have published 17 articles in the scientific literature. These publications are listed in Section 4 of this report. In the Appendix we have attached reprints of selected articles.

1. INTRODUCTION

Our program centers around the theoretical modeling of active regions, the solar corona, and the inner heliosphere, using the MHD model. During the second year, we have placed increasing emphasis in advancing from *qualitative* comparisons of our results with observations to *quantitative* comparisons. Quantitative comparisons are important because they allow us to deduce solar parameters that are beyond our theoretical understanding at present (such as coronal heating). Our long-term goal is to develop a model that can be compared directly to observations with increasing fidelity.

We have steadily increased the number of our collaborations with other solar physics groups. These have been largely driven by the success of our global coronal model. To date, we have compared our models with WIND and Ulysses spacecraft data, IPS measurements, radio emission, energetic particle events, coronal hole estimates, eclipse and coronagraph images, and a magnetic reconnection laboratory experiment.

During the second year we have added the capability to follow the real-time evolution of the solar corona as it responds to changes in the photospheric magnetic field. We have used this capability to study the evolution of the corona during the rising phase of the new solar cycle (see Section 2.1.1). We have also made some important theoretical advances in the basic theory of the initiation of coronal mass ejections (CMEs). We have shown that emerging magnetic flux can be a very effective mechanism for the destabilization of coronal streamers and active regions (see Sections 2.2.1 and 2.3.2).

2. ACHIEVEMENTS

In this section we summarize the accomplishments made by our group during the second year of our Space Physics Theory Program contract. The descriptions are primarily intended to illustrate our principal results. A full account can be found in the referenced publications.

2.1. Modeling the Large-Scale Structure of the Corona and Inner Heliosphere

We have previously described an improved thermodynamic MHD model (in the First Year Progress Report) that has considerably extended the realism with which we can model the large-scale solar corona. In this section we describe the application of this improved model, as well as our polytropic model, to studies of the structure and dynamics of the solar corona.

2.1.1. Coronal Evolution in Response to Changes in Photospheric Magnetic Fields

Frequently we use our model to compute steady-state coronal solutions for a given distribution of photospheric magnetic field (e.g., as supplied by a synoptic map of the radial magnetic field from observations; see Secs. 2.1.2 and 2.1.3). This approach is limited to the study of the long-time properties of the solar corona. In reality, even if we neglect large-scale eruptions like coronal mass ejections, the corona is changing continuously, even during times of solar minimum, as evidenced by the recent Whole Sun Month campaign and as seen in SOHO observations. This changing structure is driven by changes in the photospheric magnetic field; active regions emerge and disperse continuously during the solar cycle. We have extended our model to incorporate the evolution of the photospheric magnetic field (a boundary condition for our model), so that we can now follow the evolution of the corona. This has given us the capability to study the long-term evolution of the corona (see below), the detailed evolution during a time period of interest (e.g., during Whole Sun Month), as well as the ability to study theoretically the coronal consequences of the emergence of magnetic flux (see Sec. 2.2.1).

When we seek steady-state solutions (of Eqs. (1)–(9) in the First Year Progress Report), we set the tangential component of the electric field at the boundary, E_{t0} , to zero. This keeps B_{r0} (the radial magnetic field at the solar boundary) fixed in time. To make the flux evolve to match observed changes, it is necessary to specify a non-zero E_{t0} . In general, E_{t0} can be expressed as $\nabla_t \times \Psi \hat{r} + \nabla_t \Phi$, where Ψ and Φ are arbitrary functions (of θ and ϕ) and ∇_t indicates tangential derivatives (in the θ – ϕ plane at $r = R_s$). The potential Φ changes E_{t0} without changing the flux B_{r0} , and can be used to control the transverse magnetic field (i.e., the shear and the normal electric current), whereas the potential Ψ changes the flux. We first consider the case $\Phi = 0$. In this case, $c\nabla_t^2 \Psi = \partial B_{r0}/\partial t$, which can be solved for Ψ for the flux change specified by $\partial B_{r0}/\partial t$. Therefore, Ψ is evaluated as new solar magnetic field measurements become available, specifying the evolution of E_{t0} , which is used as a boundary condition for the MHD equations.

Thus, rather than computing a sequence of steady-state solutions for each set of magnetic field boundary values, our time-dependent MHD model now represents the actual state of the corona corresponding to the evolving magnetic field measured on the surface of the Sun.

It is important to note that a fundamental aspect of the state of the solar magnetic field is not provided by line-of-sight magnetograms. Since line-of-sight magnetograms do not provide information about the transverse component of the magnetic field, configurations with different levels of magnetic field twist cannot be distinguished (Mikić & Linker 1997). A *vector* magnetogram is required to uniquely specify the magnetic field (e.g., Mikić & McClymont 1994). In general, magnetic twist may change as a result of magnetic flux emergence or shearing flows at the photosphere. In principle, full-disk vector magnetograms can provide information about the evolution of the transverse magnetic field.

We have used a sequence of synoptic Kitt Peak observations to study the evolution of the corona during the period Feb. 1, 1997–Mar. 18, 1998 (15 Carrington rotations). This time interval covers the beginning of the new solar cycle, as the Sun emerges from solar minimum, with the appearance of high-latitude active regions. To model the evolution over a time interval of over a year is computationally prohibitive at present. In order to study the quasi-static evolution of the corona, we changed the photospheric magnetic field at a rate that was enhanced by approximately

ten times compared to real time. (This simulation took ~ 65 hours of CPU time on a single processor of the Cray-T90 supercomputer. A real-time solution would take about 10 times longer. It may be possible to perform a real-time simulation once our code is ported to a massively parallel computer; see Sec. 2.4) This approximation makes it impossible to study the detailed evolution of individual events, though it is still meaningful to study the quasi-static evolution of the large-scale structure of the corona. For this simulation we used a “minimum shear” specification, $\Phi = 0$, since measurements of the transverse field do not exist.

Figure 1 shows the evolution of the streamer structure, the coronal hole boundaries, and the heliospheric current sheet during this time period. Note the increase in complexity of the coronal magnetic field as the Sun emerges from solar minimum. Movies of the evolution of the corona were presented at the 1998 Spring AGU/SPD meeting in Boston (Tarditi, Linker, & Mikić 1998).

2.1.2. Comparison with Eclipse Observations

We have continued our tradition of using our 3D MHD model to predict the state of the corona during forthcoming total solar eclipses. (Our eclipse comparisons can be seen on our Web page, <http://iris023.saic.com:8000/corona/modeling.html>.) We have recently made a new prediction for the eclipse of February 26, 1998, observed in the Caribbean. In Figure 2 we compare our prediction to an observation by HAO.

We are planning to predict the state of the corona during the forthcoming total solar eclipse in August 1999, which will be seen in Central and Eastern Europe, the Middle-East, and Western Asia. This prediction will be our most challenging yet, since this eclipse will occur close to solar maximum, when the structure of the corona will be considerably more complicated than in previous eclipses that we have simulated.

2.1.3. MHD Modeling for Whole Sun Month

MHD modeling is particularly useful for studying the solar corona and solar wind when a coordinated set of observations is available, since it can help to synthesize different measurements into a coherent picture. The Whole Sun Month campaign (WSM; Aug. 10–Sep. 8, 1996) brought together a wide range of space and ground-based observations during solar minimum. Our 3D MHD model played a central role in the interpretation of these observations. Comparisons of our model with WSM observations are described by Linker *et al.* (1998), Breen *et al.* (1998), Gibson *et al.* (1998), and Posner *et al.* (1998).

Figure 3 shows a comparison between synoptic images from our model and white-light observations from the Mauna Loa MK3 coronameter and the LASCO coronagraph aboard SOHO. The simulated and actual synoptic images show many similar overall features, indicating that the structure of the streamer belt during WSM has been captured by the MHD model. Both sets of images show a dark region breaking up the streamer belt near 270° longitude; this phenomenon is associated with the “elephant’s trunk,” an equatorial extension of the northern polar coronal hole. The elephant’s trunk was perhaps the most conspicuous coronal feature observed during WSM, and was apparent in several different wavelengths, including SOHO EIT images, NSOKP He 10830 maps, and Yokhoh soft X-rays. It was most visible around August 26–27, 1996. Figure 4 shows tracings of the magnetic field from the MHD model as they would appear on August 27, 1996, with coronal holes (black) and closed-field regions (gray) mapped on the surface of the Sun.

Evolution of the Solar Corona During Feb. 1997–Mar. 1998

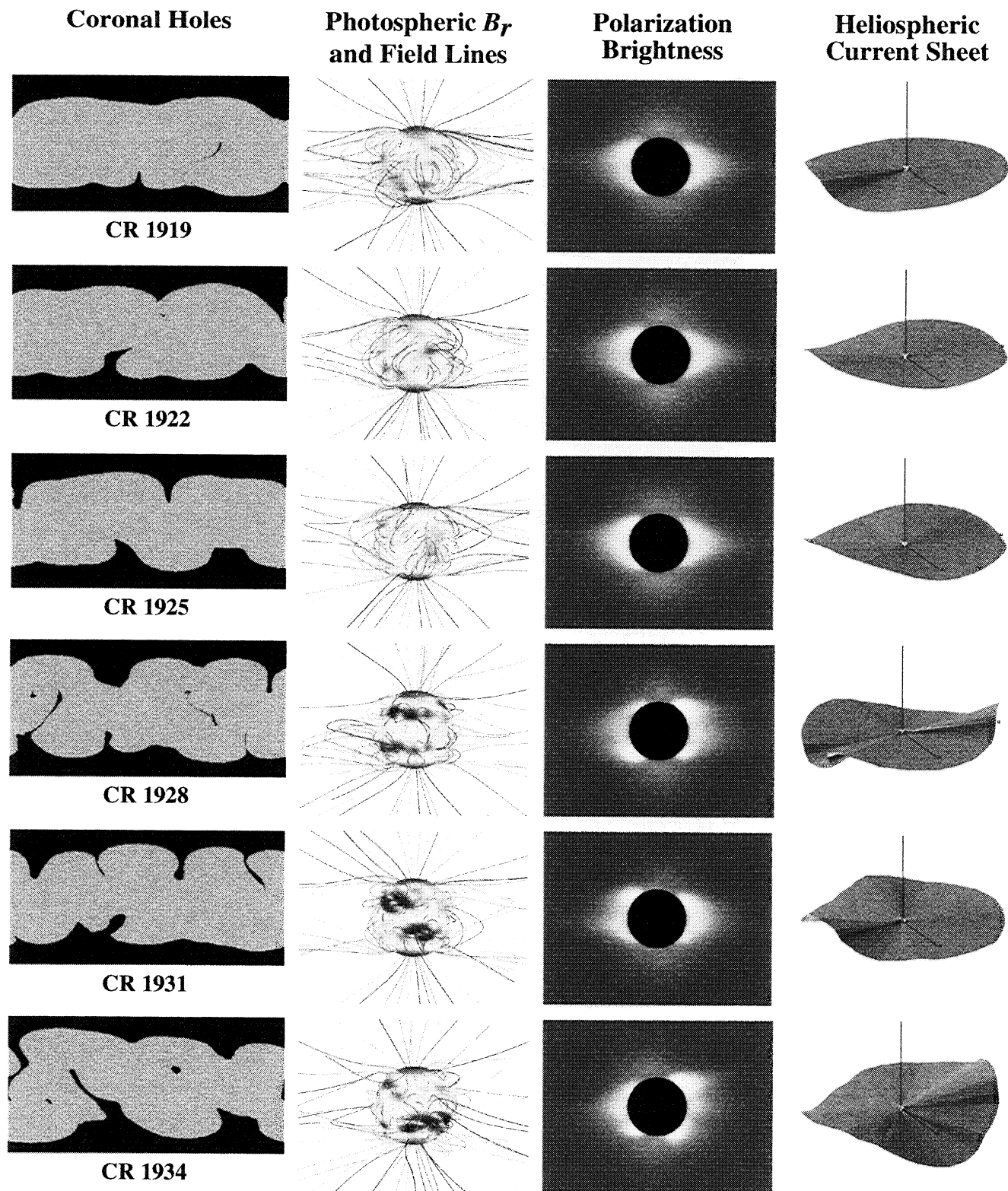


Figure 1. The changing structure of the solar corona during the period Feb. 1997–Mar. 1998 (Carrington rotations 1919–1934), as illustrated by coronal hole maps (longitude vs. latitude, with gray/black indicating closed/open field regions), field line traces with the radial magnetic field shown on the surface of the Sun, polarization brightness, and the shape of the heliospheric current sheet. This time period represents the rising phase of the new solar cycle. The photospheric magnetic field was set as a time-dependent boundary condition on the 3D MHD simulation using Kitt Peak synoptic maps.

Eclipse Prediction

February 26, 1998

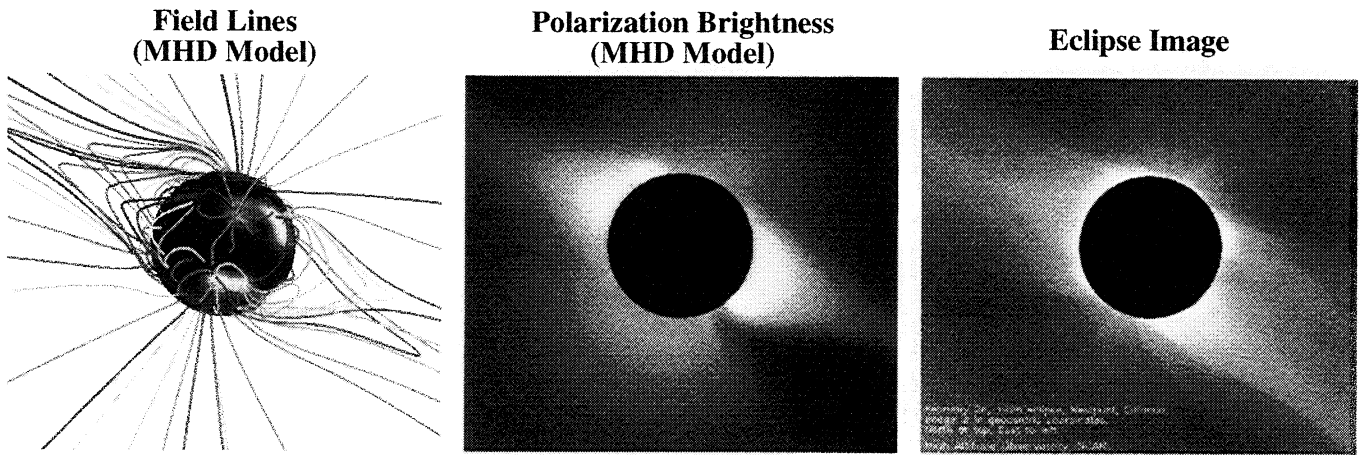


Figure 2. Comparison of an MHD prediction of the solar corona with a total solar eclipse observation. The prediction of the state of the corona was done using a 3D MHD simulation with boundary conditions on the magnetic field supplied by Kitt Peak observations collected during the period January 18 – February 12, 1998. The eclipse was visible in the Carribean. The eclipse image is courtesy of the the High Altitude Observatory, NCAR, Boulder, Colorado, USA. NCAR is sponsored by NSF.

MHD Modeling of the Solar Corona During Whole Sun Month

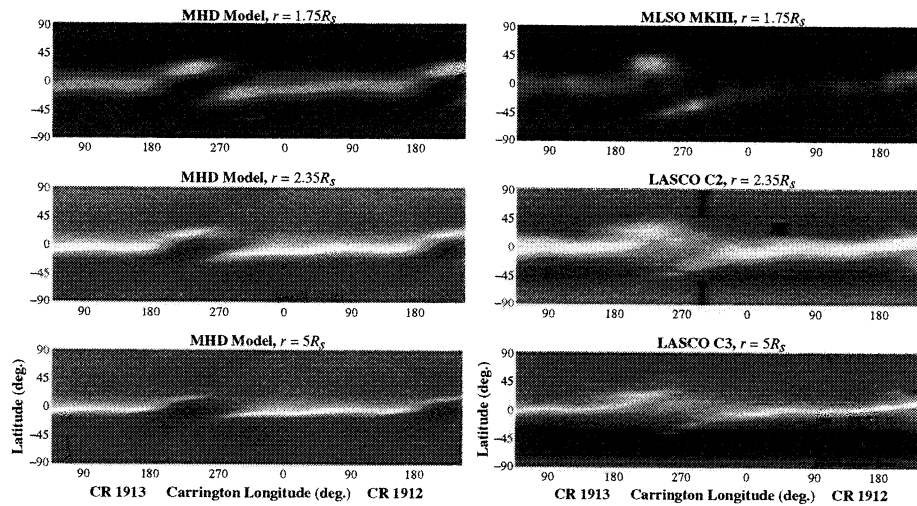


Figure 3. Comparison of simulated and actual white light synoptic images. Synoptic images are white light measurements that have been assembled throughout a rotation into a chart of brightness vs. latitude and longitude. The simulated and actual images show similar features, including the coronal hole that breaks up the streamer belt near 270 degrees.

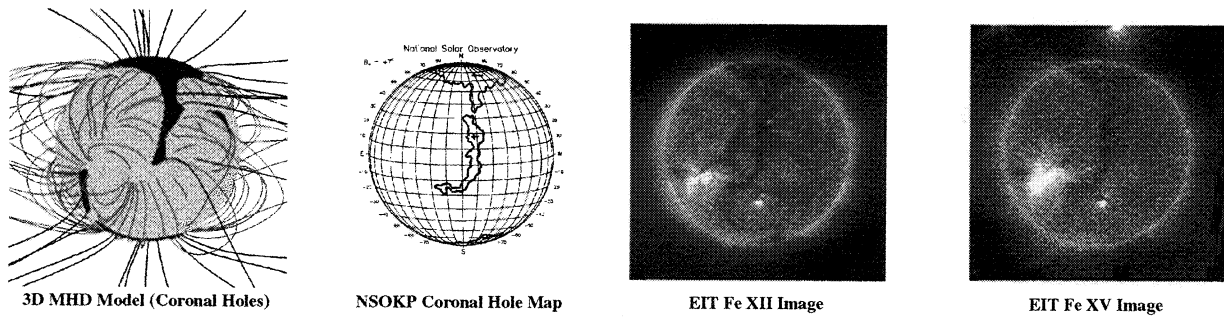


Figure 4. Comparison of the MHD model with coronal holes seen in disk measurements on August 27, 1996. The "elephant's trunk" coronal hole (extending from the northern pole past the equator) can be seen in both the simulation and the data.

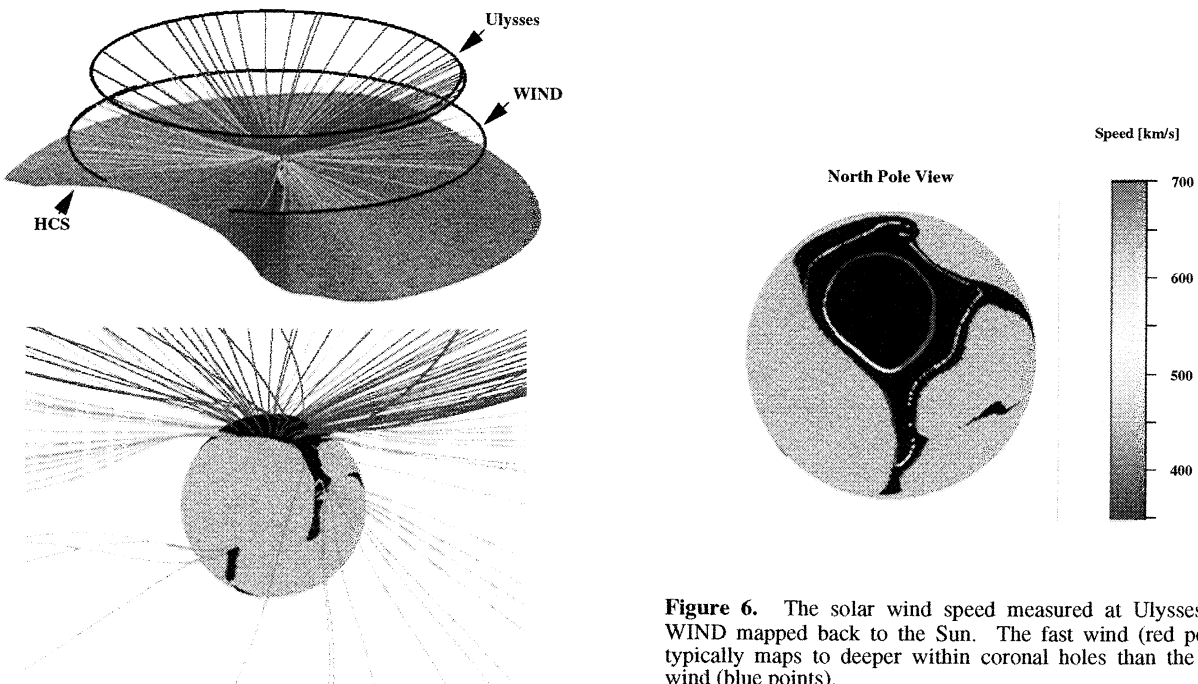


Figure 5. Magnetic field lines traced back to the Sun from Ulysses (green) and WIND (blue), together with the heliospheric current sheet and Ulysses and WIND trajectories mapped back to 15 R_{\odot} .

Figure 6. The solar wind speed measured at Ulysses and WIND mapped back to the Sun. The fast wind (red points) typically maps to deeper within coronal holes than the slow wind (blue points).

For comparison, the NSOKP coronal hole boundaries and EIT images are also shown. It is apparent that the MHD model has captured the elephant's trunk coronal hole, although the observations show the coronal hole extending to lower latitudes than predicted by the model.

We also investigated the solar origins of features observed by the Ulysses and WIND spacecraft during WSM. Figure 5 shows tracings of field lines from Ulysses (green) and WIND (blue), as well as the heliospheric current sheet (HCS) predicted by the MHD model, and the Ulysses and WIND trajectories in the Sun's rotating frame (mapped to the simulation domain). The model predicts HCS crossings by WIND (but not by Ulysses) during the WSM time period. WIND HCS crossings similar to those predicted were in fact observed. Figure 6 shows the observed solar wind speed, mapped back to its source at the Sun, with red points indicating the fastest observed speeds and blue the slowest. It is apparent that the slow wind maps back close to coronal hole boundaries, while the fast wind typically comes from deeper within coronal holes. This result was also seen during the Ulysses fast latitude scan (reported in the First Year Progress Report).

2.1.4. Modeling the Solar Wind

We have continued to perform extensive modeling in 2D (axisymmetric) geometry in order to self-consistently model the solar wind from its origins in the low corona to its expansion into interplanetary space. Our results show promising matches with generic *in situ* observations of the fast and slow solar wind, as well as the observed properties in the low corona. Full details were presented at the 1998 Spring AGU/SPD meeting in Boston (Lionello, Linker, & Mikić 1998).

Our improved thermodynamic model significantly advances our capabilities to study the large-scale corona and inner heliosphere. In the new model, the high and low temperature regions in the corona are determined self-consistently by the open/closed field topology and the coronal heating profile. The closed-field regions naturally become hotter due to the insulating effect of parallel thermal conduction. Our 2D computations have shown that we can obtain the correct density contrast between coronal holes and streamers. As we move to a 3D model, we will investigate how the plasma density (through the polarization brightness) compares *quantitatively* to Mauna Loa and LASCO data for specific observations, and we will compare the solar wind parameters predicted by the computation (density, temperature, and velocity) with WIND and Ulysses data.

2.1.5. Simulated Disk and Coronal Emission Images

Our theory program has focused on the importance of developing diagnostics that are as close as possible to actual measurements, so that direct comparison between models and observations can be achieved whenever possible. The improved thermodynamic description in our MHD model opens up the possibility of modeling disk emission, just as we have previously done for polarization brightness. For example, as part of our comparisons for the Whole Sun Month campaign (Sec. 2.1.3), we compared coronal holes observed in EIT with the open-field regions predicted by the MHD model. While the dark emission features identified as coronal holes are clearly associated with magnetically open regions on the Sun, the observations do not directly measure field topology, and at times images in different wavelengths can yield different

interpretations of the coronal hole boundary. To make a quantitative comparison between coronal models and coronal hole observations requires reproducing the emission measurement itself.

The emission lines observed by EIT arise from the excitation of iron ions, a trace species in the coronal plasma. The iron population in the corona is especially sensitive to temperature and has been modeled in the CHIANTI package (Dere *et al.* 1998) that is publicly available. Using the plasma temperature predicted by our improved MHD model, we can model the EIT emission for different lines. An example is shown in Figure 7. To generate this image, we used the polytropic MHD model (since our improved model is not operational in 3D yet), so that the temperature contrast in the model is not as large as expected. (This is a known deficiency of the polytropic model. We are merely using the polytropic model here to illustrate the technique.) The contrast observed in the synthesized emission (from the model) is produced by the contrast in plasma density (since the emission is proportional to the line-of-sight integral of the square of the electron density). We expect the agreement between our synthesized emission images and EIT observations to improve significantly when we incorporate the improved thermodynamics into our model, since this will allow the important effect of temperature on the iron population to be included.

2.2. Coronal Mass Ejections

2.2.1. Emerging Flux as a Trigger for CMEs

Recently we have explored the effect of emerging flux on the stability and evolution of helmet streamers. In an influential paper, Feynman and Martin (1995) observed that CMEs (as deduced from disappearing filaments on the disk) are closely correlated with newly emerging magnetic flux in the neighborhood. Our emerging flux capability (described in Section 2.1.1) has allowed us to study the coronal effects of the emergence of subphotospheric magnetic flux. We have found that a sheared helmet streamer (i.e., with twisted magnetic field lines) erupts when magnetic flux with the opposite magnetic polarity emerges near the neutral line. This phenomenon has a threshold: when the amount of emerged flux is below a critical level, the helmet streamer is stable, and evolves quasi-statically; when a critical level of emerged flux is exceeded, the helmet streamer erupts violently, liberating almost all of its free magnetic energy, and ejecting a plasmoid outward with considerable kinetic energy (i.e., reminiscent of a fast CME). Note that it is necessary for the helmet streamer to be twisted for the eruption to occur—streamers with no twist do not erupt.

Equilibria below the threshold naturally form a “filament” (or “flux rope”) above the neutral line. We have performed extensive simulations of this effect in 2D axisymmetric geometry (Mikić & Linker 1998), and we have begun to study the effect in 3D geometry. The (stable) “flux rope” (when the emerged flux is below the threshold) in 3D geometry is shown in Figure 8. The eruption in 3D geometry is shown in Figure 9. This is a very promising theoretical model for the initiation of CMEs by emerging flux.

2.3. Three-Dimensional Active Region Modeling

2.3.1. Interaction of Twisted Coronal Loops

We have also modeled a more complicated situation in which two coronal loops interact during their emergence. We begin with a fully emerged twisted loop in an equilibrium state. A

Simulated EIT Emission

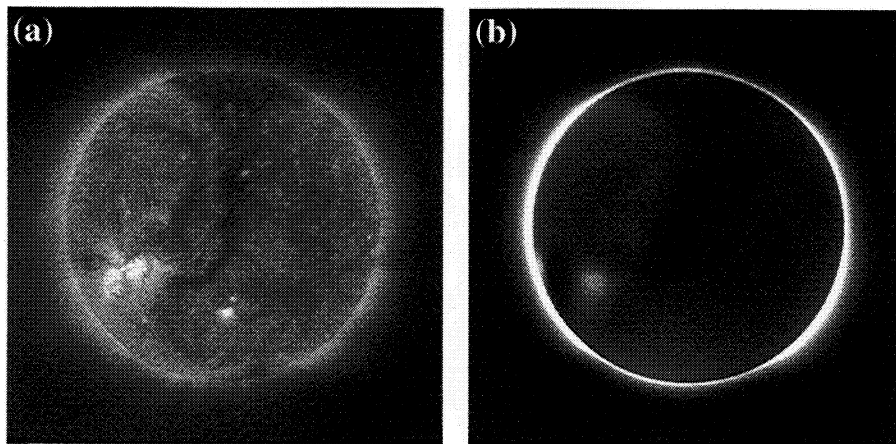


Figure 7. (a) Disk emission at 195A (Fe XII) from SOHO EIT on August 26, 1996. (b) Simulated disk emission using the polytropic MHD model (see text).

3D MHD Simulation of a CME Triggered by Emerging Flux

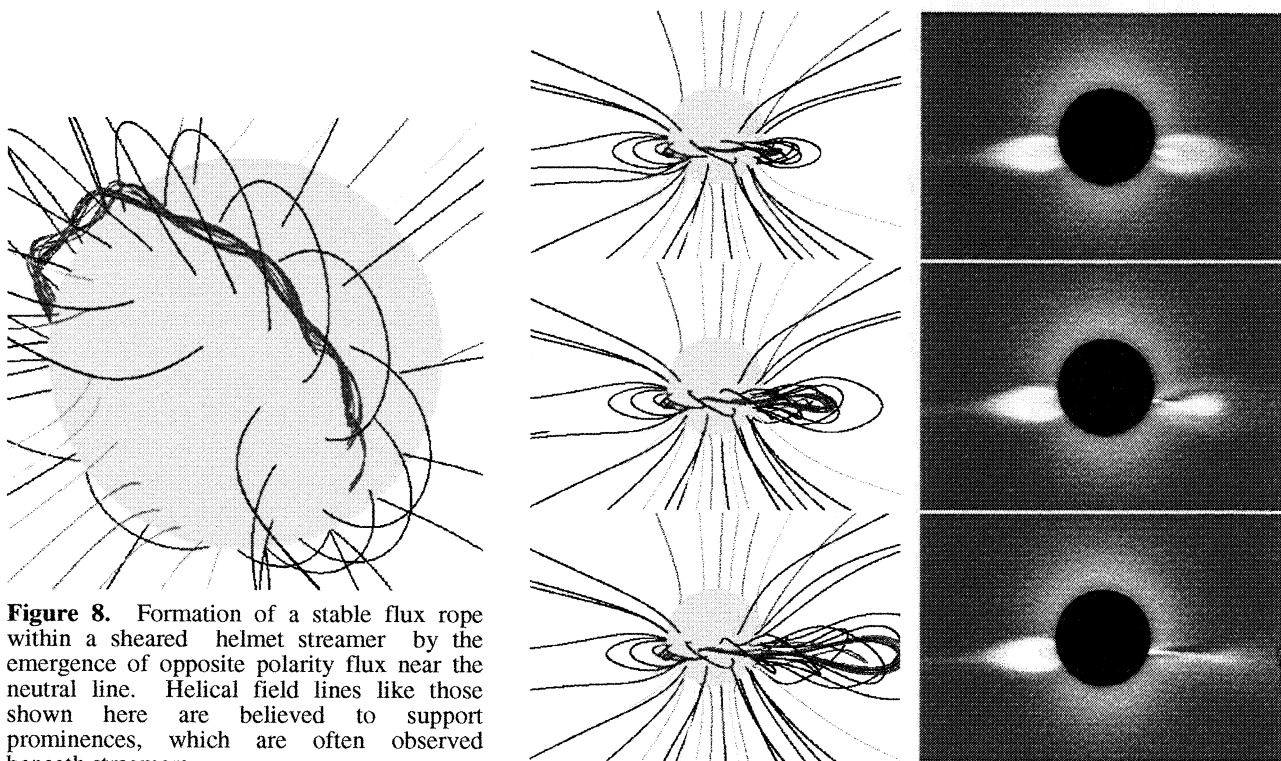


Figure 8. Formation of a stable flux rope within a sheared helmet streamer by the emergence of opposite polarity flux near the neutral line. Helical field lines like those shown here are believed to support prominences, which are often observed beneath streamers.

Figure 9. Continued emergence of opposite polarity flux leads to the eruption of the flux rope and helmet streamer (i.e., a coronal mass ejection). No flux was emerged on the opposite side of the Sun, so this part of the streamer remains stable.

second loop, intended to model a rising flux tube emerging from below the photosphere, with different characteristics and physical orientation, emerges in the neighborhood. We have investigated several cases for the orientation of the second loop. In Figure 10 we show the evolution when the second loop emerges at an angle of 15° with respect to, and directly under, the first loop (with both loops having helicity of the same sign). We are continuing to investigate the details of the evolution and interaction of such loops.

2.3.2. Eruption of an Active Region as a Result of Flux Emergence

In Section 2.2.1 we showed that a twisted large-scale coronal arcade can erupt when flux of the opposite sign emerges near the neutral line. We have investigated the evolution of an active region arcade with respect to the same phenomenon, and we find that the arcade can erupt under similar circumstances. We first create a 3D twisted force-free field with a bipolar magnetic field distribution (by applying photospheric shear to a potential field), as shown in Fig. 11a. We then emerge magnetic flux in such a way as to reduce the net flux in the active region (i.e., flux with opposite sign to the existing flux). When the amount of emerged flux is below a threshold, a stable “filament” is produced in the magnetic field above the neutral line (Fig. 11b). The twisted field lines in this 3D “filament” may be able to support a dense prominence. (Of course, this is not a filament in the traditional sense, since the model described here presently uses the zero-beta equations for simplicity. In the future, a more complete MHD model of this configuration may prove to be fruitful.) Note that the field line topology has not been prescribed: the formation of the “filament” is a natural consequence of the self-consistent evolution of the field, and has not been prescribed in any way. When the amount of emerged flux exceeds a critical threshold, the configuration erupts upward. We are continuing to study this configuration, which is a very promising candidate to explain the triggering of flares and possibly the eruption of filaments.

2.4. Massively Parallel Computing

Our spherical 3D MHD code was originally developed to take full advantage of vector computers (like the Cray-C90). In recent years, it has become clear that in order to perform more ambitious calculations (e.g., with increased spatial resolution and to simulate longer physical time periods), it has become necessary to use massively parallel computers (like the Cray-T3E). Unfortunately, it is not a trivial task to port an existing code to a massively parallel computer, since present compilers are not sophisticated enough to efficiently distribute the workload on multiple CPUs.

To efficiently utilize a massively parallel computer it is necessary to parallelize the algorithm at a relatively low level. The *de facto* standards for parallel computing are High Performance Fortran (HPF) and Message Passing Interface (MPI). In order to decide which system was most efficient for our code, we parallelized a 3D potential field solver with HPF and MPI. This code is representative of our 3D MHD code, since both codes utilize a conjugate gradient solver for the inversion of matrices (where most of the CPU time is spent).

Even though it took less time to implement HPF than MPI, our tests on the Cray-T3E show that the performance of MPI is superior to that of HPF. Ideally, the execution time (i.e., the average CPU time spent by each processor) should be inversely proportional to the number of processors. Overhead associated with communication between processors can cause deviation

Interaction of Two Coronal Loops

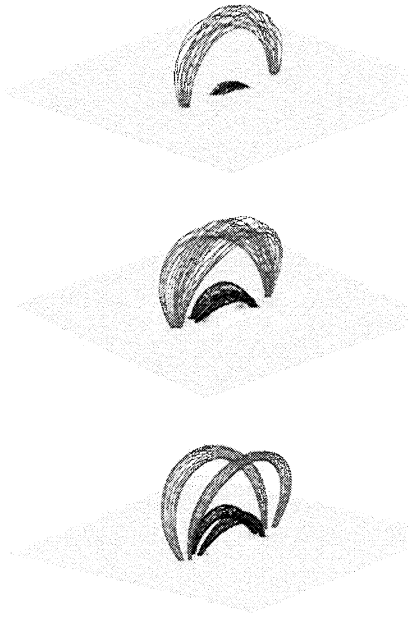
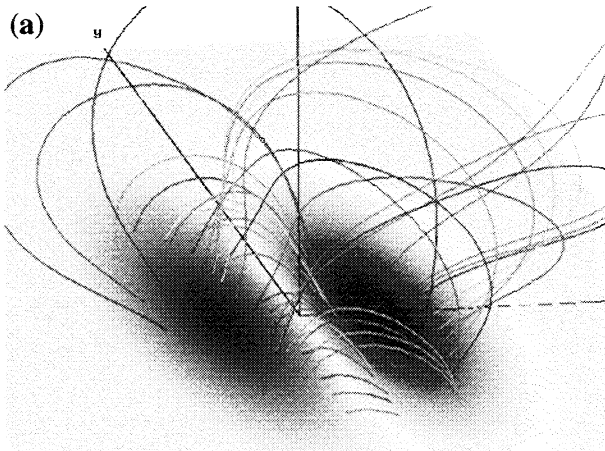


Figure 10. The red loop is a twisted pre-existing coronal loop. The black loop emerges (with twist) underneath it and interacts with it.

Initial Sheared Arcade Field



Field with a "Flux Rope" after Flux Emergence

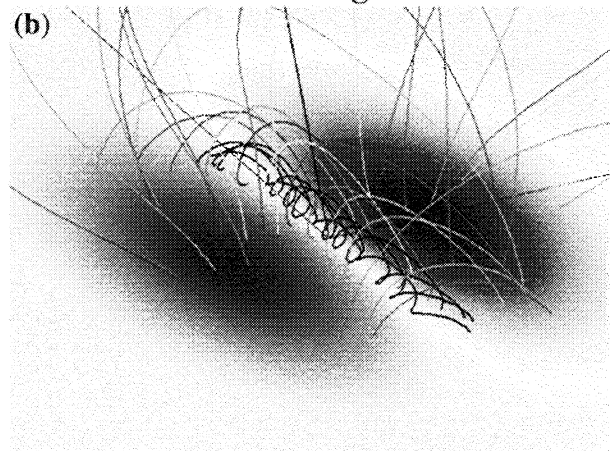


Figure 11. (a) The initial sheared field in a 3D model of an active region. The magnetic field is in a force-free equilibrium. (b) After flux emerges near the neutral line (with opposite polarity to the existing flux), a stable equilibrium with a flux rope (black field lines) is formed. The arcade erupts if additional flux is emerged.

from this ideal “scaling.” Our results show that the scaling for MPI is closer to the ideal than for HPF. In fact, the CPU time for HPF “saturates” quickly as the number of CPUs is increased, and is not even able to match the execution time of the Cray-C90. (The CPU time for MPI also begins to saturate when the number of grid points per processor falls below ~ 300 .)

This evaluation has helped us to decide to use MPI to implement the parallel version of our 3D MHD code. Even though implementing MPI is more complicated than implementing HPF, obtaining optimum efficiency is our most important concern. MPI appears to be the emerging standard for massively parallel computation, and is available on a wide variety of machines.

2.5. Simulation of the MRX Laboratory Reconnection Experiment

We have begun to apply innovative numerical techniques based on unstructured triangular grids to solar and astrophysical phenomena. We have successfully simulated a laboratory experiment that has been designed to study magnetic reconnection, especially as it relates to astrophysics. This technique is based on adaptive grids in which the mesh resolution is dynamically refined and coarsened to best represent the evolving solution.

The MRX experiment at the Princeton Plasma Physics Laboratory (Yamada *et al.* 1997) has been constructed to systematically investigate the fundamental physics of magnetic reconnection in a well-controlled laboratory setting. The boundary conditions can be controlled externally, and the Lundquist number can be varied by controlling the plasma density and the magnetic field strength. Magnetic reconnection is induced by the forced merging of two toroidal plasmas. The plasmas are hot enough to be in an interesting parameter regime ($10^2 < S \leq 10^3$), but cold enough to allow the insertion of diagnostic probes to make detailed internal measurements of the magnetic field and plasma properties. This experiment, which is funded in part by NASA, can shed light on the fundamental processes involved in magnetic reconnection.

We have used the nonlinear MHD code TRIM (Schnack, Lottati, Mikić, & Satyanarayana 1998) to carry out direct numerical simulation of the MRX experiment. TRIM solves the time-dependent resistive MHD equations in axially symmetric geometry (although the plasma dynamics may be fully three-dimensional). TRIM uses an innovative algorithm based on an unstructured mesh of triangles. This allows the geometry of MRX to be accurately captured. TRIM also uses adaptive mesh refinement to dynamically refine and coarsen the mesh in the vicinity of evolving small scale structures, such as current sheets.

The simulations show that the reconnection rate γ as a function of the Lundquist number S scales as $S^{-\alpha}$, with $\alpha \sim 0.3$, over the range $10^2 \leq S \leq 10^4$, implying that the reconnection rate is faster than the Sweet-Parker rate. We have used dynamically adaptive gridding to enhance the accuracy of these calculations. Our simulations show that a secondary magnetic island forms during the reconnection. A similar structure is seen in MRX under certain operating conditions. The secondary island is not observed in our calculations unless we use the enhanced resolution that is enabled by the adaptive grid.

3. REFERENCES

- Breen, A. R., Mikić, Z., Linker, J. A., Lazarus, A. J., Thompson, B. J., Moran, P. J., Varley, C. A., Williams, P. J. S., Biesecker, D. A., & Lecinski, A. 1998, *J. Geophys. Res.*, submitted.
- Dere, K. P., Landi, E., Mason, H. E., Monsignori Fossi, B. C., & Young, P. R. 1998, *Astron. Astrophys. Suppl.*, in press.
- Feynman, J., & Martin, S. F. 1995, *J. Geophys. Res.*, **100**, 3355.
- Gibson, S. E., Biesecker, D. A., Guhathakurta, M., Hoeksema, J. T., Lazarus, A. J., Linker, J. A., Mikić, Z., Pisanko, Yu., Steinberg, J. T., Thompson, B. J., & Zhao, X. P. 1998, *Science*, submitted.
- Linker, J. A., Mikić, Z., Biesecker, D. A., Forsyth, R. J., Gibson, S. E., Lazarus, A. J., Lecinski, A., Riley, P., Szabo, A., & Thompson, B. J. 1998, *J. Geophys. Res.*, submitted.
- Lionello, R., Linker, J. A., & Mikić, Z. 1998, Spring AGU/SPD Meeting, Boston.
- Mikić, Z., & Linker, J. A. 1996, in *Solar Wind Eight: Proc. of the Eight Intl. Solar Wind Conf.* (D. Winterhalter, J. T. Gosling, S. R. Habbal, W. S. Kurth, and M. Neugebauer, eds.), AIP Conf. Proceedings **382**, AIP Press, Woodbury, N. Y., p. 104.
- Mikić, Z., & Linker, J. A. 1997, in *Coronal Mass Ejections* (N. Crooker, J. Joselyn, and J. Feynman, eds.), *Geophysical Monograph* **99**, American Geophysical Union, p. 57.
- Mikić, Z., & Linker, J. A. 1998, in preparation.
- Mikić, Z., & McClymont, A. N. 1994, in *Solar Active Region Evolution: Comparing Models with Observations* (K. S. Balasubramaniam and G. W. Simon, eds), Astron. Soc. Pac., Conf. Series, **68**, 225.
- Posner, A., Bothmer, V., Thompson, B. J., Kunow, H., Heber, B., Muller-Mellin, R., Lazarus, A. J., Szabo, A., & Mikić, Z. 1998, *J. Geophys. Res.*, submitted.
- Schnack, D. D., Lottati, I., Mikić, Z., & Satyanarayana, P. 1998, *J. Comp. Phys.*, **140**, 71.
- Tarditi, A., Linker, J. A., & Mikić, Z. 1998, Spring AGU/SPD Meeting, Boston.
- Yamada, M., Ji, H., Carter, T., Kulsrud, R., Ono, Y., & Perkins, F. 1997, *Phys. Rev. Lett.*, **78**, 3117.

4. PUBLICATIONS SUPPORTED BY SPT CONTRACT NAS5-96081 DURING THE SECOND YEAR

1. A. R. Breen, Z. Mikić, J. A. Linker, A. J. Lazarus, B. J. Thompson, P. J. Moran, C. A. Varley, P. J. S. Williams, D. A. Biesecker, and A. Lecinski, "Interplanetary Scintillation Measurements of the Solar Wind During Whole Sun Month: Linking Coronal and *In-Situ* Observations," *J. Geophys. Res.*, submitted (1998).
2. N. U. Crooker, A. H. McAllister, R. J. Fitzenreiter, J. A. Linker, D. E. Larson, K. W. Ogilvie, R. P. Lepping, A. Szabo, J. T. Steinberg, A. J. Lazarus, Z. Mikić, and R. P. Lin, "Sector Boundary Transformation by an Open Magnetic Cloud" *J. Geophys. Res.*, submitted (1998).
3. S. E. Gibson, D. A. Biesecker, M. Guhathakurta, J. T. Hoeksema, A. J. Lazarus, J. A. Linker, Z. Mikić, Yu. Pisanko, J. T. Steinberg, B. J. Thompson, and X. P. Zhao, "The Three-Dimensional Coronal Magnetic Field During Whole Sun Month" *Science*, submitted (1998).
4. J. Lee, A. N. McClymont, Z. Mikić, S. M. White, and M. R. Kundu, "Coronal Currents, Magnetic Loops and Heating in a Solar Active Region," *Astrophys. J.* **501**, in press (1998).
5. J. Lee, S. M. White, M. R. Kundu, Z. Mikić, and A. N. McClymont, "Microwave Mode Coupling above Active Regions as a Coronal Density Diagnostic," *Solar Phys.*, in press (1998).
6. J. Lee, S. M. White, M. R. Kundu, Z. Mikić, and A. N. McClymont, "A Test for Coronal Magnetic Field Extrapolations" *Astrophys. J.*, submitted (1998).
7. J. A. Linker, Z. Mikić, D. A. Biesecker, R. J. Forsyth, S. E. Gibson, A. J. Lazarus, A. Lecinski, P. Riley, A. Szabo, and B. J. Thompson, "Magnetohydrodynamic Modeling of the Solar Corona During Whole Sun Month," *J. Geophys. Res.*, submitted (1998).
8. J. A. Linker, and Z. Mikić, "Magnetohydrodynamic Modeling of the Large-Scale Solar Corona," in preparation (1998).
9. R. Lionello, J. A. Linker, and Z. Mikić, "Stability of Algorithms for Magnetohydrodynamics with Large Flows," in preparation (1998).
10. R. Lionello, D. D. Schnack, G. Einaudi, and M. Velli, "Current sheet formation due to nonlinear kink modes in periodic and line-tied configurations," *Phys. Plasmas*, submitted (1998).
11. R. Lionello, Z. Mikić, and D. D. Schnack, "Magnetohydrodynamics of Solar Coronal Plasmas in Cylindrical Geometry," *J. Comput. Phys.* **140**, 172 (1998).
12. R. Lionello, M. Velli, G. Einaudi, and Z. Mikić, "Nonlinear Magnetohydrodynamic Evolution of Line-Tied Coronal Loops," *Astrophys. J.* **494**, 840 (1998).
13. Z. Mikić and J. A. Linker, "Emerging Flux as a Trigger for Coronal Mass Ejections," in preparation, (1998).
14. M. Neugebauer, R. J. Forsyth, A. B. Galvin, K. L. Harvey, J. T. Hoeksema, A. J. Lazarus, R. P. Lepping, J. A. Linker, Z. Mikić, J. T. Steinberg, R. von Steiger,

- Y.-M. Wang, and R. Wimmer-Schweingruber, "The Spatial Structure of the Solar Wind and Comparisons with Solar Data and Models," *J. Geophys. Res.*, in press (1998).
15. A. Posner, V. Bothmer, B. J. Thompson, H. Kunow, B. Heber, R. Muller-Mellin, A. J. Lazarus, A. Szabo, and Z. Mikić, "In-ecliptic CIR-associated Energetic Particle Events and Polar Coronal Hole Structures: SOHO/COSTEP Observations for the Whole Sun Month Campaign," *J. Geophys. Res.*, submitted (1998).
 16. D. D. Schnack, I. Lottati, Z. Mikić, and P. Satyanarayana, "A Finite-Volume Algorithm for Three-Dimensional Magnetohydrodynamics on an Unstructured, Adaptive Grid in Axially Symmetric Geometry," *J. Comput. Phys.* **140**, 71 (1998).
 17. D. D. Schnack, Z. Mikić, and D. L. Hendrix, "Current Filaments Induced in a Resistive Corona by Continuous Footpoint Motions," in preparation (1998).

APPENDIX

SELECTED REPRINTS

immersed in a uniform-pressure plasma still remains an equilibrium.) Since the magnetic field strength in the Gold–Hoyle equilibrium falls with the radial distance from the axis, the plasma beta increases with the radius, reaching $\beta = 1$ at $r \sim 10a$. We have chosen a finite beta to make the nonlinear evolution correspond more closely to the solar corona, where the plasma β is small, but finite.

Since we expect the twist in the solar corona to be introduced by slow magnetic field footpoint motions in the photosphere, the appropriate initial state ought to be one in which the twist is only slightly larger than the critical value for linear instability. There is no more footpoint shearing at $z = \pm L/2$ and the applied surface flow considered is $\mathbf{V} = 0$ (see Eq. (6)), because the time-scale evolution of the configuration (due to the kink) is smaller than the one for the photospheric flow. We selected a twist of $\Phi = 3\pi$ in order to produce a distinguishable linear phase of the instability, while at the same time keeping the excess twist (i.e., that above the stability threshold) small. In other simulations we have found that the nature of the nonlinear state does not seem to be sensitively dependent on the excess twist, as long as it is not too large [26]. The loop length is set by the condition $L = \Phi a$, giving a loop with aspect ratio $L/a = 9.42$ in this case. The (radial) Alfvén time is defined by $\tau_A = a/v_A^0$, where the Alfvén speed on the axis is given by $v_A^0 = B_0/\sqrt{4\pi\rho_0}$. A uniform viscosity is used, corresponding to a viscous dissipation time $\tau_v \equiv a^2/\nu = 100\tau_A$.

We study the ideal MHD evolution of this equilibrium (with $\eta = 0$) in order to investigate whether the nonlinear evolution of the kink instability leads to the formation of current sheets. When strong gradients develop in the magnetic field during ideal MHD numerical simulations, it may be necessary to introduce plasma resistivity. In the case of the Gold–Hoyle field, as discussed below and as noted by Baty and Heyvaerts [25], the nonlinear evolution of the kink instability does not introduce current sheets, so that it is not necessary to introduce resistivity into the calculation. This is in contrast to other equilibria that we have studied, of which the zero net-current equilibrium is a particular example, for which we have found that the nonlinear evolution of the kink leads to the formation of current sheets [26], requiring the introduction of finite resistivity during the later stages of the calculation. We were thus able to perform the present calculation with the ideal MHD model. (We note that a small amount of numerical resistivity is introduced during the calculation by the upwind treatment of the advection, as described in Appendix B.)

We start the calculation at $t=0$ with the $m=0$ equilibrium field given by Eqs. (58)–(60), to which we add a small $m=1$ perturbation with an amplitude $v \sim 3 \times 10^{-4} v_A^0$. (The perturbation was chosen to be the eigenfunction corresponding to the most unstable linear mode in a periodic cylinder, modified suitably to have zero displacement at the axial boundaries, as required by line tying. Any small initial perturbation could have been used without affecting the nonlinear results.) The equations were integrated for $500\tau_A$, requiring about three CPU hours on the Cray YMP/C-90 at NERSC. This code has also been implemented on the Cray T3D at CINECA in Bologna.

The initial time step was chosen to be $0.1\tau_A$. The time step remained $0.1\tau_A$ during the linear part of the run, decreasing to $0.05\tau_A$ during the initial phase of the nonlinear evolution as a result of the advective flow limit on the time step (Eq. 19) and increasing back to $0.1\tau_A$ after saturation of the kink toward a new equilibrium. The advantage of using the semi-implicit scheme is illustrated by the fact that the wave Courant number (i.e., the ratio of the time step to the time step required by an explicit calculation) remains significantly larger than 1 during this calculation. Initially, the wave Courant number is 16, and it increases to 30 by the end of the calculation.

Note that the three components of \mathbf{A} are coupled for $m \geq 1$. We prefer to hold η constant for the sake of simplicity. We shall drop the temporal index and write the right-hand side of Eq. (45) just as S_i , whose form is easily deduced from the left-hand side. The equation for the radial component is

$$\begin{aligned} & \left(\frac{r_i dr_i dz_{h,j}}{\eta} + \Delta t \omega \frac{m^2}{r_i} dr_i dz_{h,j} + \Delta t \omega \frac{r_i dr_i}{dz_j} + \Delta t \omega \frac{r_i dr_i}{dz_{j-1}} \right) A_{r,i,j} \\ & - \Delta t \omega \frac{r_i dr_i}{dz_j} A_{r,i,j+1} - \Delta t \omega \frac{r_i dr_i}{dz_{j-1}} A_{r,i,j-1} + i \Delta t \omega m \frac{dz_{h,j} r_{h,i+1}}{r_i} A_{\theta,i+1,j} \\ & - i \Delta t \omega m \frac{dz_{h,j} r_{h,i}}{r_i} A_{\theta,i,j} + \Delta t \omega r_i A_{z,i+1,j} - \Delta t \omega r_i A_{z,i,j} \\ & - \Delta t \omega r_i A_{z,i+1,j-1} + \Delta t \omega r_i A_{z,i,j-1} = S_{r,i,j}. \end{aligned} \quad (49)$$

The equation for θ -component is

$$\begin{aligned} & \left(\frac{r_{h,i} dr_{h,i} dz_{h,j}}{\eta} + \Delta t \omega \frac{r_{h,i}^2 dz_{h,j}}{r_i dr_i} + \Delta t \omega \boxed{\frac{r_{h,i}^2 dz_{h,j}}{r_{i-1} dr_{i-1}}} + \Delta t \omega \frac{r_{h,i} dr_{h,i}}{dz_j} \right. \\ & \left. + \Delta t \omega \frac{r_{h,i} dr_{h,i}}{dz_{j-1}} \right) A_{\theta,i,j} - \Delta t \omega \frac{r_{h,i} r_{h,i+1} dz_{h,j}}{r_i dr_i} A_{\theta,i+1,j} \\ & - \Delta t \omega \boxed{\frac{r_{h,i} r_{h,i-1} dz_{h,j}}{r_{i-1} dr_{i-1}}} A_{\theta,i-1,j} - \Delta t \omega \frac{r_{h,i} dr_{h,i}}{dz_j} A_{\theta,i,j+1} \\ & - \Delta t \omega \frac{r_{h,i} dr_{h,i}}{dz_{j-1}} A_{\theta,i,j-1} + i \Delta t \omega m dr_{h,i} A_{z,i,j} - i \Delta t \omega m dr_{h,i} A_{z,i,j-1} \\ & + i \Delta t \omega m \frac{r_{h,i} dz_{h,j}}{r_i} A_{r,i,j} - i \Delta t \omega m \boxed{\frac{r_{h,i} dz_{h,j}}{r_{i-1}}} A_{r,i-1,j} = S_{\theta,i,j}. \end{aligned} \quad (50)$$

Finally, we write the equation for the z -component as

$$\begin{aligned} & \left(\frac{r_{h,i} dr_{h,i} dz_j}{\eta} + \Delta t \omega m^2 \frac{dr_{h,i} dz_j}{r_{h,i}} + \Delta t \omega \frac{r_i dz_j}{dr_i} + \Delta t \omega \frac{r_{i-1} dz_j}{dr_{i-1}} \right) A_{z,i,j} \\ & - \Delta t \omega \frac{r_i dz_j}{dr_i} A_{z,i+1,j} - \Delta t \omega \frac{r_{i-1} dz_j}{dr_{i-1}} A_{z,i-1,j} + \Delta t \omega r_i A_{r,i,j+1} \\ & - \Delta t \omega r_i A_{r,i,j} - \Delta t \omega r_{i-1} A_{r,i-1,j+1} + \Delta t \omega r_{i-1} A_{r,i-1,j} \\ & + i \Delta t \omega m dr_{h,i} A_{z,i,j+1} - i \Delta t \omega m dr_{h,i} A_{z,i,j} = S_{z,i,j}. \end{aligned} \quad (51)$$

Note that in Eq. (50) there are diverging terms when $i = 2$. We have marked them with a , b , and c . When $m = 0$ only the first two are present. They derive from the finite difference representation of

$$\frac{1}{r} \frac{\partial}{\partial r} r A_{\theta} \Big|_1 \quad (52)$$

Thus we write

$$\begin{aligned}
v_{r;1,j} &= \begin{cases} 0 & \text{if } m \neq 1 \\ -i v_{\theta;2,j} & \text{if } m = 1 \end{cases} \\
v_{\theta;1,j} &= \begin{cases} -v_{\theta;2,j} & \text{if } m = 0, 2 \\ v_{\theta;2,j} & \text{otherwise} \end{cases} \\
v_{z;1,j} &= \begin{cases} v_{z;2,j} & \text{if } m \neq 1 \\ -v_{z;2,j} & \text{if } m = 1 \end{cases} \\
v_{r;N,j} &= V_{r;R,j} \\
v_{\theta;N,j} &= -v_{\theta;N-1,j} + 2V_{\theta;R,j} \\
v_{z;N,j} &= -v_{z;N-1,j} + 2V_{z;R,j} \\
v_{r;i,1} &= -v_{r;i,2} + 2V_{r;i,-L/2} \\
v_{\theta;i,1} &= -v_{\theta;i,2} + 2V_{\theta;i,-L/2} \\
v_{z;i,1} &= V_{z;i,-L/2} \\
v_{r;i,M} &= -v_{r;i,M-1} + 2V_{r;i,+L/2} \\
v_{\theta;i,M} &= -v_{\theta;i,M-1} + 2V_{\theta;i,+L/2} \\
v_{z;i,M} &= V_{z;i,+L/2}.
\end{aligned} \tag{43}$$

The first method to implement the boundary conditions, as explained in Subsection 3.1, can be used. In fact, the coupling of v_r and v_θ in our scheme does not spoil the self-adjoint nature of the operator.

3.3. The Induction Equation in Cylindrical Coordinates

Let us consider how to solve the induction equation

$$\frac{1}{\eta} \frac{\partial \mathbf{A}}{\partial t} = -\nabla \times \nabla \times \mathbf{A} + \mathbf{S}, \tag{44}$$

where the diffusive “curl–curl” operator is self-adjoint. We are not interested now in the ideal part of Eq. (1), which is treated separately with the predictor–corrector and merely adds a source term to the right-hand side of

$$dV \left(\frac{1}{\eta} + \omega \Delta t \nabla \times \nabla \times \right) \mathbf{A}^{(n+1)} = dV \left(\frac{1}{\eta} - (1 - \omega) \Delta t \nabla \times \nabla \times \right) \mathbf{A}^{(n)}. \tag{45}$$

The equation above is the finite-difference and self-adjoint representation of Eq. (44) when $\mathbf{S} = \mathbf{0}$. It can be shown that to have stability for all Δt it must be $\frac{1}{2} \leq \omega \leq 1$. In the code we choose $\omega = \frac{1}{2}$, which is also second-order accurate in time. The analytical form of the curl–curl operator, in cylindrical coordinates and after a Fourier transform in θ , is

$$\nabla \times \nabla \times \mathbf{A}|_r = \frac{m^2}{r^2} A_r - \frac{\partial^2 A_r}{\partial z^2} + i \frac{m}{r^2} \frac{\partial}{\partial r} (r A_\theta) + \frac{\partial^2 A_z}{\partial r \partial z}, \tag{46}$$

$$\nabla \times \nabla \times \mathbf{A}|_\theta = i m \frac{\partial}{\partial r} \frac{A_r}{r} - \frac{\partial}{\partial r} \frac{1}{r} \frac{\partial}{\partial r} r A_\theta - \frac{\partial^2 A_\theta}{\partial z^2} + i \frac{m}{r} \frac{\partial A_z}{\partial z}, \tag{47}$$

$$\nabla \times \nabla \times \mathbf{A}|_z = \frac{1}{r} \frac{\partial}{\partial r} r \frac{\partial A_r}{\partial z} + i \frac{m}{r} \frac{\partial A_\theta}{\partial z} - \frac{1}{r} \frac{\partial}{\partial r} r \frac{\partial A_z}{\partial r} + \frac{m^2}{r^2} A_z. \tag{48}$$

obtain

$$\begin{aligned}
& \left(\bar{\rho}_{i,j} r_{h,i} dr_{h,i} dz_j + \omega_1 \Delta t m^2 \frac{dr_{h,i} dz_j \bar{\alpha}_{i,j}}{r_{h,i}} + \omega_1 \Delta t \frac{r_i dz_j \hat{\alpha}_{i,j}}{dr_i} \right. \\
& \quad \left. + \omega_1 \Delta t \frac{r_{i-1} dz_j \hat{\alpha}_{i-1,j}}{dr_{i-1}} + \omega_1 \Delta t \frac{r_{h,i} dr_{h,i} \alpha_{i,j+1}}{dz_{h,j+1}} + \omega_1 \Delta t \frac{r_{h,i} dr_{h,i} \alpha_{i,j}}{dz_{h,j}} \right) v_{z,i,j} \\
& \quad - \omega_1 \Delta t \frac{r_i dz_j \hat{\alpha}_{i,j}}{dr_i} v_{z,i+1,j} - \omega_1 \Delta t \frac{r_{i-1} dz_j \hat{\alpha}_{i-1,j}}{dr_{i-1}} v_{z,i-1,j} \\
& \quad - \omega_1 \Delta t \frac{r_{h,i} dr_{h,i} \alpha_{i,j+1}}{dz_{h,j+1}} v_{z,i,j+1} - \omega_1 \Delta t \frac{r_{h,i} dr_{h,i} \alpha_{i,j}}{dz_{h,j}} v_{z,i,j-1} = S_{z,i,j}. \quad (36)
\end{aligned}$$

Let us consider the boxed line in Eq. (35); it contains r_{i-1} at denominator which diverges for $i = 2$. The boxed derivatives in Eq. (32) produce that term. Using the results in Appendix A we can rewrite the representation for $m = 1$ of the second diverging derivative in Eq. (32) as

$$\left. \frac{\partial}{\partial r} \frac{v_r}{r} \right|_2 = -\frac{a_0}{r_{h;2}} + a_1 + O(r^2) = \frac{v_{r;2}/r_2 - Y}{dr_{h;2}} \quad (37)$$

$$v_{r;2} = a_0 + a_1 r_{h;2} + O(r^4). \quad (38)$$

Now Y can be easily found, taking into account that

$$2r_{h;2} = r_2 = dr_{h;2}. \quad (39)$$

The first derivative can be treated in the same way. Hence, the boxed line of Eq. (35) when $i = 2$ and $m = 1$ becomes

$$+i\omega_1 \Delta t (\alpha_{2,j} + \hat{\alpha}_{1,j}) \left(-\frac{5}{2} \frac{r_{h;2}}{r_2} \right) v_{r;1,j}. \quad (40)$$

When $m = 2$ we can write

$$\left. \frac{v_r}{r} \right|_1 = \left. \frac{\partial v_r}{\partial r} \right|_1 = -i \left. \frac{\partial v_\theta}{\partial r} \right|_1 = -i \frac{v_{\theta;2,j} - v_{\theta;1,j}}{dr_1}. \quad (41)$$

The boxed line of Eq. (35) then becomes

$$-\omega_1 \Delta t (\alpha_{2,j} + \hat{\alpha}_{1,j}) r_{h;2} \frac{v_{\theta;2,j} - v_{\theta;1,j}}{dr_1}. \quad (42)$$

For $m \geq 3$ the above-cited line equals zero for $i = 2$. It is quite easy to verify that the equations for the components of \mathbf{v} have been written in a self-adjoint form. Once we have fixed the boundary conditions we can deliver the equations to the CG solver.

The field \mathbf{v} may assume (in principle) arbitrary values \mathbf{V} at $z = \pm L/2$ and $r = R$, while for the singular boundary at $r = 0$ the values are dictated by conditions in Appendix A.

And, finally, for the z component we obtain

$$\nabla \cdot \alpha \nabla \mathbf{v}|_z = \frac{1}{r} \frac{\partial}{\partial r} r \alpha \frac{\partial v_z}{\partial r} - m^2 \alpha \frac{v_z}{r^2} + \frac{\partial}{\partial z} \alpha \frac{\partial v_z}{\partial z}. \quad (33)$$

We choose as a natural grid for α the same as that used for ρ_0 . This grid is shown in Fig. 4. When interpolated values are needed on other grids we put a $\hat{\cdot}$ or a $\bar{\cdot}$ over the symbol to indicate respectively interpolation along r or z . We can now write the numerical representation of Eq. (30). We shall drop the temporal index for brevity. The right-hand side is indicated with just an S_i , but its formula is analogous to the left-hand side, the only differences being the use of the old values of \mathbf{v} and the factor $-\omega_2$, instead of ω_1 . The equation for the v_r component is

$$\begin{aligned} & \left(r_i dr_i dz_{h,j} \hat{\rho}_{i,j} + \omega_1 \Delta t \frac{r_i^2 dz_{h,j} \alpha_{i+1,j}}{r_{h,i+1} dr_{h,i+1}} + \omega_1 \Delta t \frac{r_i^2 dz_{h,j} \alpha_{i,j}}{r_{h,i} dr_{h,i}} + \omega_1 \Delta t \alpha_{i+1,j} dz_{h,j} \right. \\ & \quad \left. - \omega_1 \Delta t \alpha_{i,j} dz_{h,j} + \omega_1 \Delta t m^2 \frac{\hat{\alpha}_{i,j} dr_i dz_{h,j}}{r_i} + \omega_1 \Delta t \frac{r_i dr_i \hat{\alpha}_{i,j}}{dz_j} + \omega_1 \Delta t \frac{r_i dr_i \hat{\alpha}_{i,j-1}}{dz_{j-1}} \right) v_{r,i,j} \\ & \quad - \omega_1 \Delta t \frac{r_{i+1} r_i dz_{h,j} \alpha_{i+1,j}}{r_{h,i+1} dr_{h,i+1}} v_{r,i+1,j} - \omega_1 \Delta t \frac{r_{i-1} r_i dz_{h,j} \alpha_{i,j}}{r_{h,i} dr_{h,i}} v_{r,i-1,j} \\ & \quad - \omega_1 \Delta t \frac{r_i dr_i \hat{\alpha}_{i,j}}{dz_j} v_{r,i,j+1} - \omega_1 \Delta t \frac{r_i dr_i \hat{\alpha}_{i,j-1}}{dz_{j-1}} v_{r,i,j-1} \\ & \quad - i \omega_1 \Delta t \frac{m}{2} (\alpha_{i+1,j} + \hat{\alpha}_{i,j}) \left(\frac{r_i}{r_{h,i+1}} - \frac{r_{h,i+1}}{r_i} \right) v_{\theta,i+1,j} \\ & \quad + i \omega_1 \Delta t \frac{m}{2} (\alpha_{i,j} + \hat{\alpha}_{i,j}) \left(\frac{r_i}{r_{h,i}} - \frac{r_{h,i}}{r_i} \right) v_{\theta,i,j} = S_{r,i,j}. \end{aligned} \quad (34)$$

The one for the v_θ component is

$$\begin{aligned} & \left(r_{h,i} dr_{h,i} dz_{h,j} \rho_{i,j} + \omega_1 \Delta t (1 + m^2) \frac{dr_{h,i} dz_{h,j} \alpha_{i,j}}{r_{h,i}} + \omega_1 \Delta t \frac{r_i dz_{h,j} \hat{\alpha}_{i,j}}{dr_i} \right. \\ & \quad \left. + \omega_1 \Delta t \frac{r_{i-1} dz_{h,j} \hat{\alpha}_{i-1,j}}{dr_{i-1}} + \omega_1 \Delta t \frac{r_{h,i} dr_{h,i} \bar{\alpha}_{i,j}}{dz_j} + \omega_1 \Delta t \frac{r_{h,i} dr_{h,i} \bar{\alpha}_{i,j-1}}{dz_{j-1}} \right) v_{\theta,i,j} \\ & \quad - \omega_1 \Delta t \frac{r_i dz_{h,j} \hat{\alpha}_{i,j}}{dr_i} v_{\theta,i+1,j} - \omega_1 \Delta t \frac{r_{i-1} dz_{h,j} \hat{\alpha}_{i,j}}{dr_{i-1}} v_{\theta,i-1,j} - \omega_1 \Delta t \frac{r_{h,i} dr_{h,i} \bar{\alpha}_{i,j}}{dz_j} v_{\theta,i,j+1} \\ & \quad - \omega_1 \Delta t \frac{r_{h,i} dr_{h,i} \bar{\alpha}_{i,j-1}}{dz_{j-1}} v_{\theta,i,j-1} \left[+ i \omega_1 \Delta t \frac{m}{2} (\alpha_{i,j} + \hat{\alpha}_{i-1,j}) \left(\frac{r_{i-1}}{r_{h,i}} - \frac{r_{h,i}}{r_{i-1}} \right) v_{r,i-1,j} \right] \\ & \quad - i \omega_1 \Delta t \frac{m}{2} (\alpha_{i,j} + \hat{\alpha}_{i,j}) \left(\frac{r_i}{r_{h,i}} - \frac{r_{h,i}}{r_i} \right) v_{r,i,j} = S_{\theta,i,j}. \end{aligned} \quad (35)$$

Note that when $m > 0$ the equations for v_r and v_θ are coupled. For the v_z component we

3. Get $(\mathbf{M} \cdot \Psi^{(b)})_i$, $i = 2, N - 1$. The only nonzero components are $(\mathbf{M} \cdot \Psi^{(b)})_2 = \mathcal{M}_{+,1} \mathcal{V}_0$ and $(\mathbf{M} \cdot \Psi^{(b)})_{N-1} = \mathcal{M}_{+,N} \mathcal{V}_L$.

4. Find boundary contributions to the right-hand side of (27), $\tilde{S}_i = S_i - (\mathbf{M} \cdot \Psi^{(b)})_i$, $i = 2, N - 1$.

During the main iteration loop we calculate the “homogeneous part” of the solution, setting $\mathcal{V} = 0$. At each iteration of the CG solver the matrix–vector product $(\mathbf{M} \cdot \Psi)_i$ is evaluated in two steps:

1. Set the boundary points on Ψ . Since $\mathcal{V} = 0$, $\Psi_1 = -\mathcal{C}_0 \Psi_2$, and $\Psi_N = -\mathcal{C}_L \Psi_{N-1}$.
2. Get $(\mathbf{M} \cdot \Psi)_i$, $i = 2, N - 1$.

After the CG algorithm iterations, when the solution Φ_i is retrieved, its values for $i = 1$ and $i = N$ are easily deduced from Eq. (28).

3.2. Viscosity Equation in Cylindrical Coordinates

In order to solve Eq. (4) the viscosity and semi-implicit operators must be inverted. If we write the finite difference equivalents of Eqs. (16)–(17) as we have the numerical counterpart for the one-dimensional model in Eq. (24), we obtain matrices that are no longer self-adjoint as the analytical operators and require a slow algorithm for their inversion. However, it is possible to implement a general numerical scheme for inverting both operators. We shall represent them as symmetric and positive-definite matrices, using Subsection 3.1 as a guideline. We write

$$(\rho dV - \Delta t \omega_1 dV \nabla \cdot \alpha \nabla) \mathbf{v}^{(n+1)} = [\rho dV + \Delta t \omega_2 dV \nabla \cdot \alpha \nabla] \mathbf{v}^{(n)}. \quad (30)$$

For the viscosity operator α is $\nu\rho$ (we write ρ instead of ρ_0 to avoid subscript overloading). Since we use a fully implicit advancement to ensure an efficient damping of the small unresolved scales, we take $\omega_1 = 1$ and $\omega_2 = 0$. For the semi-implicit algorithm $\alpha = C^2 \Delta t \rho_0$ and $\omega_1 = 1$, $\omega_2 = -1$. Note that it is necessary to multiply both sides of the equation by the element of volume dV in order to obtain a self-adjoint matrix. This enables us to use the CG algorithm. The differential operator $dV \nabla \cdot \alpha \nabla$ must be represented in a discrete form without spoiling the symmetry of the matrix. Thus, we first write this operator in cylindrical coordinates in the following form: for the r component it is

$$\begin{aligned} \nabla \cdot \alpha \nabla \mathbf{v}|_r = & \frac{\partial}{\partial r} \alpha \frac{\partial}{\partial r} (r v_r) - \frac{\partial \alpha}{\partial r} \frac{v_r}{r} - \frac{m^2 \alpha}{r^2} v_r + \frac{im}{2} \left(\frac{\partial}{\partial r} \left(\frac{\alpha v_\theta}{r} \right) - \frac{1}{r^2} \frac{\partial}{\partial r} (r \alpha v_\theta) \right) \\ & + \frac{im}{2} \left(\alpha \frac{\partial}{\partial r} \left(\frac{v_\theta}{r} \right) - \frac{\alpha}{r^2} \frac{\partial}{\partial r} (v_\theta r) \right) + \frac{\partial}{\partial z} \alpha \frac{\partial v_r}{\partial z}. \end{aligned} \quad (31)$$

For the θ component it is

$$\begin{aligned} \nabla \cdot \alpha \nabla \mathbf{v}|_\theta = & \frac{1}{r} \frac{\partial}{\partial r} r \alpha \frac{\partial v_\theta}{\partial r} - (1 + m^2) \alpha \frac{v_\theta}{r^2} - \frac{im}{2} \left(\frac{\partial}{\partial r} \left(\frac{\alpha v_r}{r} \right) - \frac{1}{r^2} \frac{\partial}{\partial r} (r \alpha v_r) \right) \\ & - \frac{im}{2} \left(\alpha \frac{\partial}{\partial r} \left(\frac{v_r}{r} \right) - \frac{\alpha}{r^2} \frac{\partial}{\partial r} (v_r r) \right) + \frac{\partial}{\partial z} \alpha \frac{\partial v_\theta}{\partial z}. \end{aligned} \quad (32)$$

Note that in this form the matrix \mathbf{M} is explicitly symmetric. Here we have dropped the temporal index and have indicated the known term just with S_i . In computing $(\mathbf{M} \cdot \Psi)_i$ (where Ψ_i is either the guess solution or a temporary vector used by the CG algorithm), the index i may vary only in the range $2 \leq i \leq N - 1$. When we know how to fix the proper boundary conditions, without spoiling the self-adjoint nature of the operator, we shall be able to apply the CG algorithm.

Boundary conditions are generally *Dirichlet conditions* (values specified at boundary points) or *Neumann conditions* (normal gradients at the boundaries). But even a combination of both is possible if we write them as

$$\begin{aligned}\Psi_1 + C_0 \Psi_2 &= \mathcal{V}_0 \quad \text{for } x = 0, \\ \Psi_N + C_L \Psi_{N-1} &= \mathcal{V}_L \quad \text{for } x = L.\end{aligned}\tag{28}$$

Where $\mathcal{V}_{0,L}$ and $C_{0,L}$ are constants whose values determine whether Dirichlet ($C=0$) or Neumann ($C=-1$) conditions apply. A proof that the matrix \mathbf{M} is positive definite, with constraints as in Eq. (28), is given in Appendix C.

The way we implement the boundary conditions in our algorithm depends on how we intend to calculate the matrix–vector product at each iteration. We shall examine two methods: the first one modifies the matrix itself, the second one modifies the vector Ψ_i .

To implement the first scheme we store the main diagonal $\mathcal{M}_{0,i}$ and one offset diagonal $\mathcal{M}_{+,i}$ of the matrix. The diagonal values and the right-hand side S_i must be modified according to Eq. (28) when $i=2$ and when $i=N-1$ as

$$\begin{aligned}\tilde{\mathcal{M}}_{0,2} &= \mathcal{M}_{0,2} - C_0 \mathcal{M}_{+,1}, \\ \tilde{S}_2 &= S_2 - \mathcal{V}_0 \mathcal{M}_{+,1}; \\ \tilde{\mathcal{M}}_{0,N-1} &= \mathcal{M}_{0,N-1} - C_L \mathcal{M}_{+,N}, \\ \tilde{S}_{N-1} &= S_{N-1} - \mathcal{V}_L \mathcal{M}_{+,N}.\end{aligned}\tag{29}$$

For $3 \leq i \leq N-2$, $\tilde{S}_i = S_i$, and $\tilde{\mathcal{M}}_{0,i} = \mathcal{M}_{0,i}$. Now only values of Ψ_i with $2 \leq i \leq N-1$ enter into the calculation of $\mathbf{M} \cdot \Psi$ and \mathbf{M} is a symmetric positive definite matrix. After the CG algorithm iterations, when we have found the solution Φ_i for the internal points, we set Φ_1 and Φ_N according to Eq. (28).

However, the previous method might not work when we deal with 2D or 3D problems and more complicated operators such as “curl–curl.” Then it is possible that boundary conditions couple two different components of a vector field. In those cases, when we cannot write the modified diagonals for the self-adjoint matrix as in (29), we rely on the following method that has the advantage that we do not need to explicitly write the diagonals.

We have implemented a subroutine to set the boundary points of the vector Ψ according to Eq. (28). Another subroutine calculates $(\mathbf{M} \cdot \Psi)_i$, receiving an N component vector in input and yielding an $N-2$ component vector in output. We split the calculation of the solution of Eq. (27) into two parts. First, we calculate the “inhomogeneous part,” fixing the boundary condition for the right-hand side. We take finite \mathcal{V} terms and use $\Psi^{(b)}$ as a work-array. The steps we perform are:

1. Set $\Psi^{(b)} = \mathbf{0}$.
2. Set the boundary points on $\Psi^{(b)}$. Since internal points are all zero we obtain $\Psi_1^{(b)} = \mathcal{V}_0$ and $\Psi_N^{(b)} = \mathcal{V}_L$.

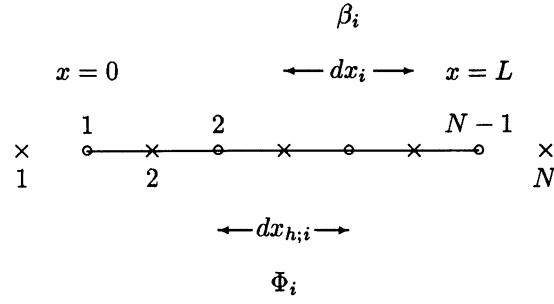


FIG. 7. Mesh used to represent Eq. (22). The physical region is between 0 and L . Φ lies on the mesh whose points are marked with \times ; β lies on the one indicated with \circ 's. dx_i and $dx_{h,i}$ are the distances between neighbor points for each mesh.

$$\begin{aligned} \Phi_i^{n+1} - \omega \Delta t \frac{\beta_i \frac{\Phi_{i+1}^{n+1} - \Phi_i^{n+1}}{dx_i} - \beta_{i-1} \frac{\Phi_i^{n+1} - \Phi_{i-1}^{n+1}}{dx_{i-1}}}{dx_{h,i}} \\ = \Phi_i^n + (1 - \omega) \Delta t \frac{\beta_i \frac{\Phi_{i+1}^n - \Phi_i^n}{dx_i} - \beta_{i-1} \frac{\Phi_i^n - \Phi_{i-1}^n}{dx_{i-1}}}{dx_{h,i}}, \end{aligned} \quad (24)$$

where the distance between two mesh points on the half-integer and on integer mesh are indicated with dx_i and $dx_{h,i}$, respectively. If we write Eq. (24) in matrix form as it stands, we find that the matrix A is not symmetric. Hence, we cannot apply the CG algorithm (actually the matrix is tridiagonal, and we might use a fast *ad hoc* direct solver for such cases. However it loses this property when we increase the number of dimensions).

We know that for functions that are zero at the boundaries the following equality holds:

$$\int_0^L X D_\beta \Phi dx = \int_0^L \Phi D_\beta X dx. \quad (25)$$

We can write the numerical representation of Eq. (25) as a product between matrices and vectors,

$$X \cdot \mathbf{dx} \mathbf{D}_\beta \cdot \Phi = \Phi \cdot \mathbf{dx} \mathbf{D}_\beta \cdot X. \quad (26)$$

Here \mathbf{dx} is a diagonal matrix whose elements are $dx_{h,i}$. With the discretization given by (24), we find that $\mathbf{dx} \mathbf{D}_\beta$ is a self-adjoint matrix. When β is positive, the matrix is also positive definite.

Therefore, if we multiply both sides of Eq. (24) by $dx_{h,i}$, we obtain

$$\begin{aligned} (\mathbf{M} \cdot \Phi)_i &\equiv \mathcal{M}_{0;i} \Phi_i + \mathcal{M}_{+;i} \Phi_{i+1} + \mathcal{M}_{-;i} \Phi_{i-1} = S_i; \\ \mathcal{M}_{0;i} &= dx_{h,i} + \omega \Delta t \left(\frac{\beta_i}{dx_i} + \frac{\beta_{i-1}}{dx_{i-1}} \right); \\ \mathcal{M}_{+;i} &= -\omega \Delta t \frac{\beta_i}{dx_i}; \\ \mathcal{M}_{-;i} &= \mathcal{M}_{+;i-1}. \end{aligned} \quad (27)$$

3. SELF-ADJOINT REPRESENTATION OF THE DIFFUSIVE AND SEMI-IMPLICIT TERMS

The differential operators in the MHD equations have the property of being self-adjoint. Let us concentrate only on the diffusive terms that appear in Eq. (1) (resistive diffusion operator) and in Eq. (4) (semi-implicit and viscous). When these equations are advanced in time implicitly the problem requires solving the algebraic equation

$$Ax = b, \quad (21)$$

where A is the coefficient matrix, x is the unknown vector, and b is the known term. In our case the dimension of the matrix A is $3IJ \times 3IJ$ at worst, when the equations for the three vector components are coupled.

We shall show that it is possible to write for all the above-cited operators a matrix A that is self-adjoint and positive-definite. This preserves an important property of the analytical equation and has also a desirable numerical advantage; we can apply the conjugate gradient (CG) algorithm to rapidly compute the solution x , instead of more complicated and general methods. The theory of the CG method is given in [16], and an application to a problem similar to ours is in [17]. Briefly, the CG method is an iterative algorithm to find the solution vector of the linear system (21) through successive approximations. It involves the matrix A only in the context of matrix–vector multiplication. Differently from other iterative methods, estimates of the largest and smallest eigenvalues of the iteration matrix are not needed. However rapid convergence occurs when the ratio between the maximum and minimum eigenvalues of A (known as the condition number) is small. Since our matrix is diagonally dominant, we apply diagonal preconditioning and obtain a matrix with a smaller condition number. The techniques described in this section make the code about 10 times faster than its previous version in [15], which uses the biconjugate gradient method [17].

3.1. One-Dimensional Model

We present now a discussion about how to implement a self-adjoint representation of a diffusive operator in one dimension. We consider the following diffusion equation:

$$\frac{\partial \Phi}{\partial t} = \frac{\partial}{\partial x} \left(\beta \frac{\partial \Phi}{\partial x} \right) \equiv D_\beta \Phi; \quad (22)$$

x is assumed to vary between 0 and L . We want to solve the equation above numerically. First we fix two staggered meshes as in Fig. 7. Φ is defined on the half-integer mesh (marked with \times 's), while β lies on the integer mesh (marked with \circ 's). The grid points need not be uniform. A general finite difference method for solving Eq. (22) is

$$\frac{\Phi^{n+1} - \Phi^n}{\Delta t} = \omega \mathbf{D}_\beta \cdot \Phi^{n+1} + (1 - \omega) \mathbf{D}_\beta \cdot \Phi^n. \quad (23)$$

Operators and vectors are in bold when we refer to them as a whole; when we consider their components we write them in normal type. The value of ω can be any number between 0 (fully explicit) and 1 (fully implicit). $\omega = \frac{1}{2}$ corresponds to a (centered) second-order accurate in Δt time discretization. We rewrite the previous equation in components as

$$\frac{\mathbf{v}^{n+1} - \mathbf{v}^{**}}{\Delta t} = \frac{\nabla v \rho_0^{n+1/2} \nabla \mathbf{v}^{n+1}}{\rho_0^{n+1/2}}. \quad (17)$$

We have marked with P's and C's respectively the predictor and corrector steps in the equations for \mathbf{A} , ρ , p , and \mathbf{v} . Quantities marked with a * or a ** index are provisional values needed in the predictor–corrector schemes and for a fully implicit treatment of the viscous term in Eq. (17).

The constant C^2 is the semi-implicit coefficient. The semi-implicit method is described in [13]. This method is unconditionally stable with respect to all magneto–acoustic and shear Alfvén modes. Hence, accuracy becomes the most relevant consideration in the choice of the time step. Briefly, the method consists of adding to the original momentum equation (4) a linear term multiplied by a coefficient proportional to the time step,

$$\frac{1}{\rho_0} \nabla \cdot C^2 \Delta t^2 \rho_0 \nabla \frac{\partial \mathbf{v}}{\partial t}. \quad (18)$$

This removes the small time-step restriction originally introduced by the wave term. Inverting the linear operator above is much less complex and requires less computer memory than using a fully implicit scheme. The advective terms in (1)–(4) are formally only first-order accurate in Δt , while the wave-like terms are second-order accurate (centered). The use of the semi-implicit method for the wave terms leaves only the stability condition

$$|(kV)_{\max} \Delta t| < 1, \quad (19)$$

due to the explicit treatment of advection. The quantity k is the magnitude of the largest wave vector compatible with the grid size at the point (r_i, z_j, θ_k) ,

$$k = \sqrt{k_\theta^2 + k_r^2 + k_z^2} = \sqrt{\left(\frac{M}{3r_i}\right)^2 + \left(\frac{1}{dr_i}\right)^2 + \left(\frac{1}{dz_j}\right)^2}. \quad (20)$$

Note the presence of the factor “3” in the expression for k_θ , due to the dealiasing algorithm which restricts the largest poloidal mode to $M/3$.

In order to address the stability limits imposed by the advective terms in Eqs. (1)–(4) and to give a heuristic justification of Eqs. (19), (20), we present a one-dimensional Von Neumann stability analysis of the advection part of the algorithm in Appendix B.

A stability analysis of our algorithm indicates that the wave-like terms are stable for any choice of time step, and the advective terms are stable when Eq. (19) is satisfied. However, we have recently found that the coupling of the leapfrog advance of the wave-like terms with a predictor–corrector for the advective terms may introduce numerical instability. This instability does not develop when there is sufficient viscosity in the algorithm. The calculations we describe in Section 4 have sufficient viscosity to prevent this numerical instability from occurring. We have analyzed this coupling, and we have devised an algorithm that does not suffer from this instability [19]. The fully implicit differencing of diffusive terms in Eqs. (1) and (4) does not introduce any stability limitation in the time step.

divergence of a curl and the curl of a gradient vanish identically. The components of \mathbf{B} and \mathbf{J} are naturally specified on integer or half-integer meshes according to their definition. The components of the nonlinear terms in Eqs. (1)–(4) are evaluated on the same grid of the field components on the left-hand side, using simple averaging where necessary.

Physical boundary conditions for \mathbf{A} and \mathbf{v} are specified at $z = \pm L/2$ and $r = R$ according to Eqs. (5)–(6).

Boundary values for p and ρ are not required to be specified in our formulation, but they can be evaluated for diagnostic purposes using extrapolation. At $r = 0$ we apply geometric boundary conditions as shown in Appendix A. It is not completely straightforward to implement such boundary conditions, as they tend to spoil the symmetry properties of the operators we have to invert. See Section 3 for further discussion.

2.2. Temporal Approximation

The right-hand sides of Eqs. (1)–(4) have advective, dissipative, and wave-like terms that are treated using predictor–corrector, implicit, and semi-implicit methods. We introduce a leapfrog time discretization for the various fields, defining \mathbf{A} (together with ρ and p) and \mathbf{V} at staggered time intervals. The resulting algorithm is

$$\frac{\mathbf{A}^* - \mathbf{A}^{n-1/2}}{\Delta t} = \mathbf{v}^n \times \mathbf{B}^{n-1/2}, \quad \text{P} \quad (9)$$

$$\begin{aligned} \frac{\mathbf{A}^{n+1/2} - \mathbf{A}^{n-1/2}}{\Delta t} &= \mathbf{v}^n \times \mathbf{B}^* \\ &\quad - \eta \frac{\nabla \times \nabla \times \mathbf{A}^{n+1/2}}{2} \\ &\quad - \eta \frac{\nabla \times \nabla \times \mathbf{A}^{n-1/2}}{2}, \end{aligned} \quad \text{C} \quad (10)$$

$$\frac{\rho^* - \rho^{n-1/2}}{\Delta t} = -\nabla \cdot (\rho^{n-1/2} \mathbf{v}^n), \quad \text{P} \quad (11)$$

$$\frac{\rho^{n+1/2} - \rho^{n-1/2}}{\Delta t} = -\nabla \cdot (\rho^* \mathbf{v}^n), \quad \text{C} \quad (12)$$

$$\frac{p^* - p^{n-1/2}}{\Delta t} = -\nabla \cdot (p^{n-1/2} \mathbf{v}^n), \quad \text{P} \quad (13)$$

$$\begin{aligned} \frac{p^{n+1/2} - p^{n-1/2}}{\Delta t} &= -\nabla \cdot (p^* \mathbf{v}^n) \\ &\quad - (\gamma - 1) p^{n-1/2} \nabla \cdot \mathbf{v}^n, \end{aligned} \quad \text{C} \quad (14)$$

$$\frac{\mathbf{v}^* - \mathbf{v}^n}{\Delta t} = -\mathbf{v}^n \cdot \nabla \mathbf{v}^n, \quad \text{P} \quad (15)$$

$$\begin{aligned} \frac{\mathbf{v}^{**} - \mathbf{v}^n}{\Delta t} &= -\mathbf{v}^n \cdot \nabla \mathbf{v}^* \\ &\quad + \frac{\mathbf{J}^{n+1/2} \times \mathbf{B}^{n+1/2}}{\rho^{n+1/2}} - \frac{\nabla p^{n+1/2}}{\rho^{n+1/2}} \\ &\quad + \frac{\nabla \cdot C^2 \Delta t^2 \rho_0^{n+1/2} \nabla (\mathbf{v}^{**} - \mathbf{v}^n)}{\Delta t \rho_0^{n+1/2}}, \end{aligned} \quad \text{C} \quad (16)$$

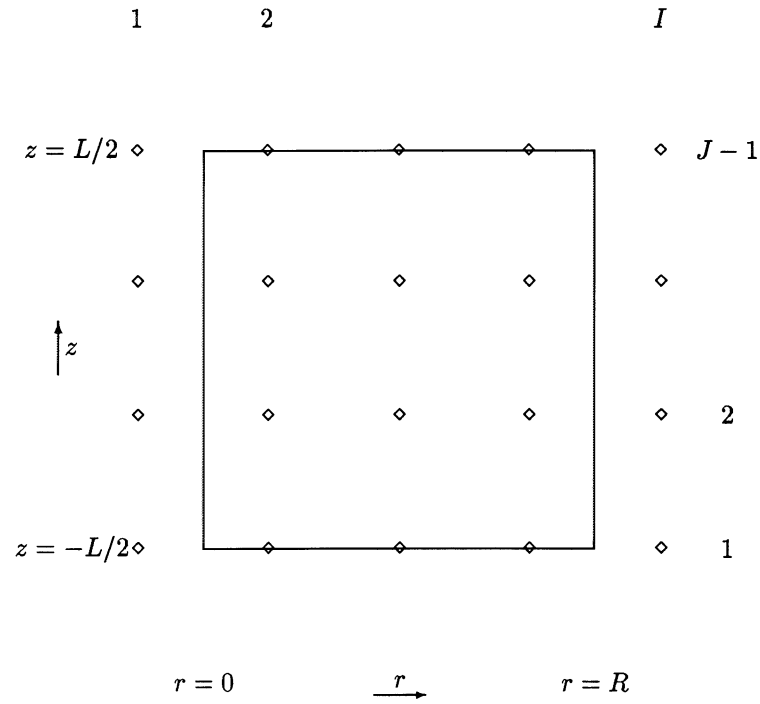


FIG. 5. Mesh for v_z , A_z , B_r , and J_z . The square represents the physical domain in r and z . Mesh points are indicated with \diamond .

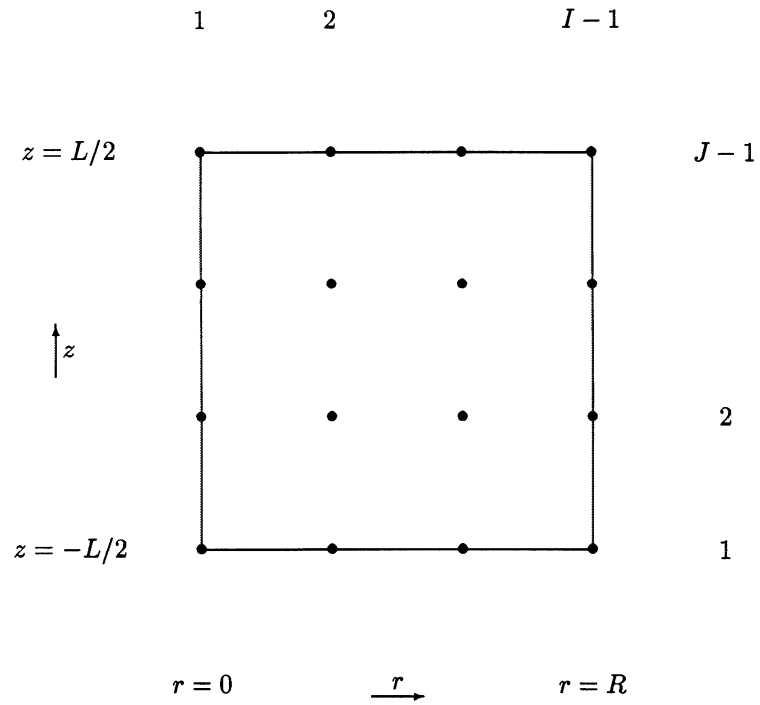


FIG. 6. Mesh for B_θ , v , and η . The square represents the physical domain in r and z . Mesh points are indicated with \bullet .

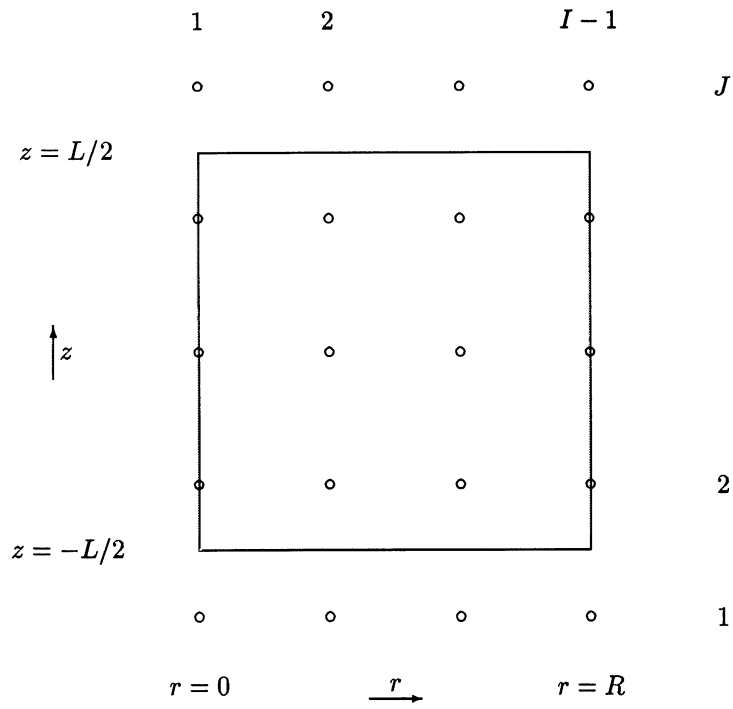


FIG. 3. Mesh for v_r , A_r , B_z , and J_r . The square represents the physical domain in r and z . Mesh points are indicated with \circ .

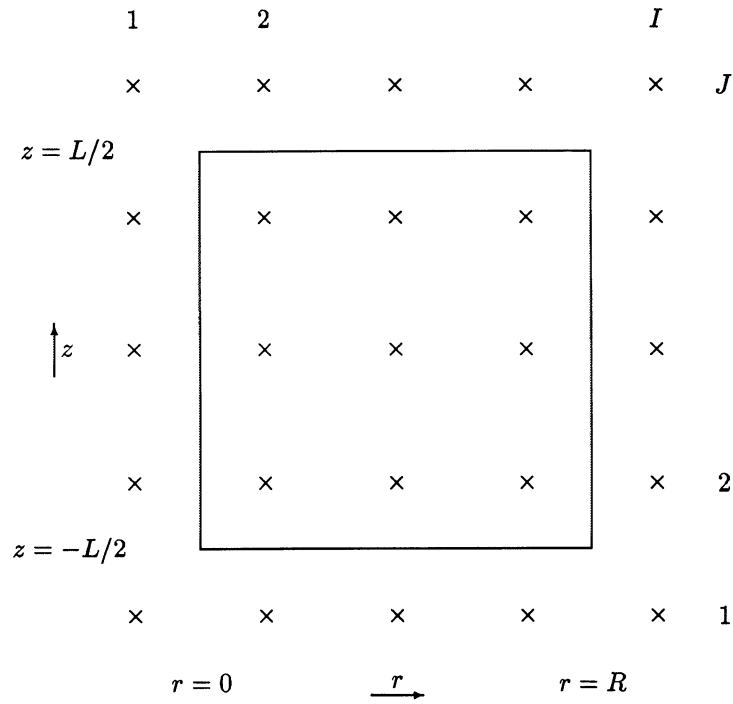


FIG. 4. Mesh for v_θ , A_θ , J_θ , ρ , and p . The square represents the physical domain in r and z . Mesh points are indicated with \times .

The reality of f requires that $f_m = f_{-m}^*$, where f_m^* is the complex conjugate of f_m . Moreover, f_0 and $f_{m/2+1}$ have zero imaginary parts. We apply (8) to the MHD equations (1)–(4), obtaining a set of M nonlinear partial differential equations in the variables (r, z, t) describing the evolution of the Fourier components of \mathbf{A} , \mathbf{v} , ρ , and p .

We evaluate the nonlinear terms in Eqs. (1)–(4) with a fully dealiased pseudospectral algorithm, as described in [20]. The pseudospectral method consists of computing operations either in Fourier space or in real space, according to where it is more convenient. Thus multiplication is performed in real space to avoid convolution, and derivatives in θ are evaluated in Fourier space. We use a fast Fourier transform to transform between the two representations. However, multiplication generates aliasing errors, due to quadratic and higher nonlinearities. Hence, we truncate the θ -spectrum (dealiasing) and retain only two-thirds of available Fourier space.

In order to simplify an implicit treatment, we assume that η and ν do not depend on θ . This choice makes the implicit viscous and resistive operators linear in θ , and, consequently, poloidal modes decouple in Fourier space.

We choose two staggered meshes for each nonperiodic direction, r and z . Beside being second-order accurate in calculating derivatives (when uniform meshes are specified), in this method boundary conditions are specified naturally: for the magnetic field only the normal component is specified, while the tangential one is computed, and for the electric field the tangential component is specified, while the normal component is computed. Moreover, the algorithm has the property that the longitudinal and transverse parts of vectors are effectively decoupled, so that initially vanishing longitudinal and transverse components will vanish all the time. A consequence of this is that $\nabla \cdot \mathbf{B} = 0$.

Current sheets may form during the nonlinear phase of instabilities in our simulations. We therefore allow the mesh points in the radial direction to have nonuniform spacing in order to have locally enhanced resolution in the proximity of the center of the loop. The axial mesh is normally (but not necessarily) uniformly spaced. Radial mesh points on the integer mesh are indicated with $(r_i, i = 1, I - 1)$, where $r_1 = 0$ and $r_{I-1} = R$. On the half-integer mesh we write $(r_{h,i}, i = 1, I)$. The relationship between the two set of mesh points is $r_{h,i} = (r_i + r_{i-1})/2$. We define also the finite increments $(dr_{h,i} = r_i - r_{i-1}, i = 2, I - 1)$ and $(dr_i = r_{h,i+1} - r_{h,i}, i = 1, I - 1)$. In the axial direction we define $(z_j, j = 1, J - 1)$, with $z_1 = -L/2$ and $z_{J-1} = L/2$, with analogous definitions for $z_{h,j}$, dz_j , and $dz_{h,j}$. Figures 3, 4, 5, and 6 show how the dependent variables are defined on each mesh.

Derivatives are defined on integer or half-integer meshes according to Table 1. With these definitions the gradient, divergence, and curl operator can be implemented so that the

TABLE 1
Differential Operators and Their Corresponding
Finite Difference Representations

Operator	Integer mesh	Half-integer mesh
$\frac{1}{r} \frac{\partial}{\partial \theta}$	$i \frac{m}{r_i} C_{i,j}$	$i \frac{m}{r_{h,i}} D_{i,j}$
$\frac{\partial}{\partial r}$	$\frac{E_{i,j} - E_{i-1,j}}{dr_{h,i}}$	$\frac{F_{i+1,j} - F_{i,j}}{dr_i}$
$\frac{\partial}{\partial z}$	$\frac{G_{i,j} - G_{i,j-1}}{dz_{h,j}}$	$\frac{H_{i,j+1} - H_{i,j}}{dz_j}$

applying the condition at the boundaries $z = \pm L/2$,

$$\frac{\partial \mathbf{A}_t}{\partial t} = (\mathbf{V} \times \mathbf{B})_t, \quad (5)$$

$$\mathbf{v} = \mathbf{V}, \quad (6)$$

where the subscript t indicates the tangential component of vectors (the normal component of \mathbf{A} is advanced as in Eq. (1)). Hence boundary conditions are specified only on the tangential electric field and normal magnetic field. Equations (5)–(6) are also valid at the radial boundary at $r = R$, where a conducting wall is present and $\mathbf{V} = \mathbf{0}$. The wall is placed far enough from the plasma not to affect the physics being studied.

In order to translate from nondimensional to physical quantities we have to specify three normalization variables for length, magnetic field, and density. For example, when modeling coronal loops, we can set $L_o = 10^8$ cm, $B_o = 10$ G, and $\rho_o = 10^{-15}$ g cm $^{-3}$. Then fields and scalars in Eqs. (1)–(4) can be measured in terms of

$$\begin{aligned} A_o &\equiv B_o L_o && \text{G cm,} \\ V_o &\equiv B_o (4\pi \rho_o)^{-1/2} && \text{cm s}^{-1}, \\ J_o &\equiv c B_o (4\pi L_o)^{-1} && \text{statamp cm}^{-2}, \\ P_o &\equiv B_o^2 (4\pi)^{-1} && \text{dyne cm}^{-2}, \\ t_o &\equiv L_o B_o^{-1} (4\pi \rho_o)^{1/2} && \text{s,} \\ \eta_o &\equiv (4\pi)^{1/2} c^{-2} \rho_o^{-1/2} B_o L_o && \text{s,} \\ \nu_o &\equiv B_o L_o (4\pi \rho_o)^{-1/2} && \text{cm}^2 \text{s}^{-1}. \end{aligned}$$

In terms of this normalization, we have: the Alfvén velocity $v_A = V_o \sim 9 \times 10^9$ cm s $^{-1}$, the Alfvén time $\tau_A = L_o/v_A \sim 1$ s, the mass scale $M = \rho_o L_o^3 = 1 \times 10^9$ g, etc.

2.1. Spatial Approximation

We use cylindrical coordinates (r, θ, z) , with $0 \leq r \leq R$, $0 \leq \theta \leq 2\pi$, $-L/2 \leq z \leq L/2$, to model large aspect-ratio coronal loops. A sketch of the coordinate system is presented in Fig. 2. The θ coordinate is periodic, so we introduce a discrete mesh $\theta_j = 2\pi(j-1)/M$, $j = 1, 2, \dots, M$, and write any field f as a finite Fourier series,

$$f(r, \theta_j, z) = \sum_{m=-M/2+1}^{M/2+1} f_m(r, z) e^{im\theta_j}. \quad (7)$$

It is well known that the discrete Fourier series converges rapidly if the solution is smooth [18]. Furthermore, time advancement in Fourier space is facilitated because the poloidal (m) modes for linear operators decouple. Hence, implicit terms, which are present in the induction and momentum equations and must be inverted, will be represented as distinct small submatrices (one for each Fourier mode), instead of a single large matrix.

The complex coefficients f_m are given by

$$f_m(r, z) = \frac{1}{M} \sum_{j=1}^M f(r, \theta_j, z) e^{-im\theta_j}. \quad (8)$$

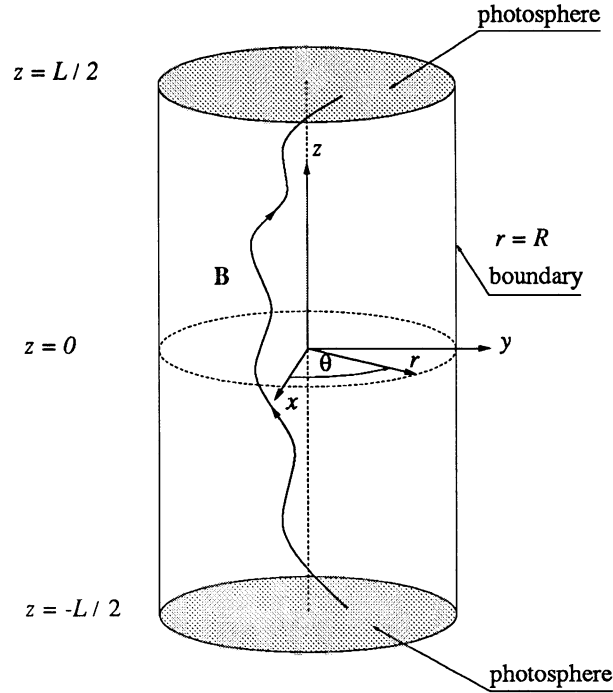


FIG. 2. Coordinates and boundaries for modeling coronal loops. Field lines are anchored in the photosphere at $z = \pm L/2$. The loops in the code are “straightened out,” since we ignore the curvature observed in real loops (see Fig. 1).

The induction equation (1) allows us to select between ideal ($\eta = 0$) or resistive MHD ($\eta \neq 0$). An ideal run is possible only in particular conditions, for example, to study the linear phase of an instability. In general, the grid resolution dictates the minimum values of η and ν that may be used. For example, for a $64 \times 32 \times 64$ grid, we have found on a particular problem that they must be at least $\sim 10^{-3}$, and sometimes $\sim 10^{-2}$, for the solution to be physically valid.

When we discuss the zero-beta model, in which we assume that $p = 0$, we specify the density to be uniform and fixed in time, so that the mass continuity equation (2) is not solved. Similarly, we do not advance the energy equation (3) in the zero-beta model. Note that we neglect the influence of viscous and resistive heating, since we use an adiabatic energy equation. We plan to add the viscous and resistive heating terms, as well as thermal conduction, in future versions of the code.

The viscosity in the momentum equation (4) is mainly used to damp short-wavelength modes in the calculation. In this term we have used $\rho_0 = 1/(2\pi) \int \rho d\theta$, instead of ρ , to allow the matrix inversion to proceed mode by mode.

The equations describe the long-wavelength and long time-scale evolution of the corona, including magneto-acoustic waves, ideal and resistive instabilities, and resistive and viscous damping. However, particle acceleration and X-ray emission require kinetic models that are not part of the code.

In a coronal loop, the dense photosphere anchors the footpoints of the magnetic field lines, so that they are dragged by applied surface flows \mathbf{V} . This footpoint shearing is modeled by

a description of the implementation of a conjugate gradient algorithm for the inversion of the implicit spatial operators; in Section 4 we describe an application of the code, and in Section 5 we summarize our conclusions.

2. COMPUTATIONAL MODEL

Coronal loops consist of a hot, tenuous plasma embedded in a strong magnetic field. A most important feature of the loops is that their ends are firmly anchored in the dense photosphere. A sketch of a coronal loop is shown in Fig. 1.

The resistive MHD model is appropriate for our study of solar coronal plasmas. The MHD equations are written in cylindrical coordinates, neglecting for simplicity the curvature effect. Hence, loops in our analysis are “straightened out” as in Fig. 2. This is clearly an approximation and important effects are neglected in principle. This description is expected to be appropriate when the aspect ratio (i.e., the ratio between the radial and the axial length scales) is large. We write the MHD equations in a convenient nondimensional form as

$$\frac{\partial \mathbf{A}}{\partial t} = \mathbf{v} \times \mathbf{B} - \eta \nabla \times \nabla \times \mathbf{A}, \quad (1)$$

$$\frac{\partial \rho}{\partial t} = -\nabla \cdot (\rho \mathbf{v}), \quad (2)$$

$$\frac{\partial p}{\partial t} = -\nabla \cdot (p \mathbf{v}) - (\gamma - 1)p \nabla \cdot \mathbf{v}, \quad (3)$$

$$\frac{\partial \mathbf{v}}{\partial t} = -\mathbf{v} \cdot \nabla \mathbf{v} + \frac{\mathbf{J} \times \mathbf{B}}{\rho} - \frac{\nabla p}{\rho} + \frac{\nabla \cdot \nu \rho_0 \nabla \mathbf{v}}{\rho_0}, \quad (4)$$

where \mathbf{A} is the vector potential of the magnetic field $\mathbf{B} = \nabla \times \mathbf{A}$, $\mathbf{J} = \nabla \times \mathbf{B}$ is the current density, \mathbf{v} is the velocity, p the pressure, ρ the mass density, η the resistivity, and ν the viscosity.

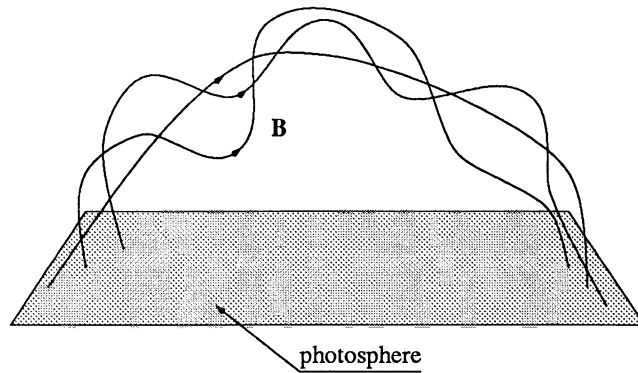


FIG. 1. A schematic representation of the magnetic field of a loop in the solar corona. Note that all the field lines are anchored in the photosphere at both ends. In our code we neglect the curvature and the loop appears “straightened out” (see Fig. 2).

its structure and evolution. Loops of tenuous magnetized plasma are observed frequently in the corona. The ends of these coronal loops are anchored in the dense photosphere below, a situation that has been referred to as *line tying*. The slow motions in the photosphere drive the footpoints of the loops, which evolve through series of equilibria. Rapid evolution may occur when an unstable equilibrium is reached, possibly leading to the development of current sheets, magnetic reconnection, and the release of magnetic energy that may heat the corona. If such “disruptions” are sufficiently impulsive, they may be identified with solar flares. Recent observational and theoretical results on flares and coronal heating can be found in [1–4].

A complete description of these processes requires a three-dimensional model that includes the slow, long-wavelength evolution prior to disruption, as well as the rapid short-wavelength evolution in the nonlinear phase. The resistive magnetohydrodynamic (MHD) model is appropriate to describe much of the physics associated with these phenomena (except in places where the gradient scale-length is smaller than the gyroradius and a kinetic treatment must be adopted). For simplicity we will restrict our attention to geometries that are best described in a cylindrical coordinate system. When modeling coronal loops, we will therefore neglect the important effect of loop curvature [5], studying instead straight flux tubes as an approximation to large-aspect-ratio coronal loops.

Although the linear stability properties of cylindrical flux tubes have been studied analytically [6–9], a description of the nonlinear evolution requires a computational approach. Several cylindrical MHD codes, with axially periodic boundary conditions, have been used to model laboratory plasmas [10–14]. However, we cannot use such codes for our studies because we need to impose line-tied boundary conditions to properly model coronal loops, and a new algorithm must be developed for this purpose.

The goal of the present paper is to describe a fast, accurate, and reliable algorithm for the advancement of the full resistive and viscous MHD equations in cylindrical geometry which allows for the specification of driving photospheric motions at the magnetic footpoints. The code is an improved version of the algorithm employed in [15]. Quantities are evaluated on grids: the azimuthal variation (θ) is represented using Fourier series, with pseudospectral calculation of derivatives; the r and z coordinates are discretized on staggered meshes, which allows us to define a curl operator whose divergence vanishes identically. A leapfrog scheme is used for the time advancement of the wave terms. We employ a semi-implicit operator in the momentum equation, following the method described in [13], while treating advection with a predictor–corrector scheme. The semi-implicit scheme allows us to set the time step through considerations of accuracy rather than stability of the algorithm and leads to a substantial saving of CPU time, compared to a fully explicit algorithm.

The resistive and viscous diffusion terms are advanced implicitly. The resulting implicit equations and the semi-implicit operator are inverted using a preconditioned conjugate gradient method [16,17]. We have attempted to preserve many of the analytical properties of the MHD equations in the discretized equations. In particular, we have taken special care to preserve the self-adjointness of spatial difference operators. Since the proper differencing of a self-adjoint operator results in a symmetric matrix, we are therefore able to use the efficient methods that exist for inverting symmetric matrices. As an illustration of the properties of our algorithm, we describe its application to the linear and nonlinear evolution of a kink instability in a twisted flux tube.

The paper is organized as follows: in Section 2 we describe the MHD equations and the spatial and temporal approximations employed to advance them in time; Section 3 contains

Magnetohydrodynamics of Solar Coronal Plasmas in Cylindrical Geometry

Roberto Lionello,^{*,†,1} Zoran Mikić,^{*} and Dalton D. Schnack^{*}

^{*}*Science Applications International Corporation, San Diego, California 92121-1578; †Department of Physics and Astronomy, University of California, Irvine, California 92697-4575*

E-mail: lionel@iris023.saic.com

Received November 18, 1996; revised August 16, 1997

We describe a three-dimensional algorithm for the advancement of the resistive MHD equations in cylindrical geometry with line-tied boundary conditions. This code has been developed to simulate the behavior of solar coronal plasmas. A finite-difference discretization is used for the radial and axial coordinates; a pseudospectral method is used for the azimuthal coordinate. The dependent variables are defined on finite-difference meshes that are staggered with respect to each other to facilitate the application of boundary conditions. The time-advance algorithm features a semi-implicit leapfrog scheme for the wave terms, a predictor–corrector treatment of advection, and an implicit advance of the resistive and viscous diffusion terms. The semi-implicit and implicit operators are inverted using a preconditioned conjugate gradient method. Special care is taken in maintaining the self-adjointness of the discretized operators, so that a fast inversion algorithm applicable to symmetric matrices can be used. By way of illustration, we describe the application of the code to the linear and nonlinear evolution of a kink instability in a twisted flux tube. © 1998 Academic Press

Key Words: partial differential equations; initial value and time-dependent initial-boundary value problems; numerical linear algebra; iterative methods for linear systems; astronomy and astrophysics; hydrodynamic and hydromagnetic problems; fluid mechanics; magnetohydrodynamics and electrohydrodynamics.

1. INTRODUCTION

The solar corona abounds with interesting phenomena of controversial physical interpretation. Although it is not understood why the corona is so hot (around 10^6 K) and what causes flares to occur, it is believed that magnetic reconnection plays a crucial role in determining

¹ Formerly at Dipartimento di Astronomia e Scienza dello Spazio, Università di Firenze, I-50125 Firenze, Italy.

In Figs. 8 and 9 we plot the magnetic energy and the kinetic energy in various modes as a function of time. Initially, the $m = 0$ mode shows the relaxation of the analytic equilibrium to the mesh (since it is not a perfect equilibrium of the discretized equations). The $m = 1$ mode grows exponentially in time, with a growth rate $\gamma\tau_A = 0.022$. The higher- m modes show growth associated with the coupling to the $m = 1$ mode. Beginning at $t \sim 200\tau_A$, when the $m = 1$ mode reaches a significant amplitude, there is a nonlinear interaction during which the higher- m modes become sizable. This phase corresponds to the observed kinking of the axis of the flux tube. Eventually, the kink mode appears to saturate, indicating that the kinked flux tube is settling toward a new equilibrium.

The linear growth rate of the $m = 1$ mode at $\Phi = 3\pi$ is lower than previous estimates because of the effect of finite beta. For the case with zero beta, the growth rate has been estimated previously as $\gamma\tau_A = 0.034$ by Mikić *et al.* [15], $\gamma\tau_A = 0.027$ by Foote and Craig [23], and $\gamma\tau_A = 0.037$ by Baty and Heyvaerts [25]. Apparently, even though the plasma beta is small on the axis, the growth rate is changed significantly by the plasma pressure. This is because the magnetic field strength falls far from the axis in this equilibrium, so that even a small pressure can affect the kinking motion of the flux tube. Indeed, when we repeated the calculation with the zero-beta model (i.e., with $p_o = 0$ and a constant density), we found the linear growth rate of the $m = 1$ mode to be $\gamma\tau_A = 0.038$, in good agreement with previous zero-beta results. (The growth rate determined by Foote and Craig is only intended to be a rough approximation for this equilibrium near the marginal stability point [23].) The finite pressure leads to a reduction of the growth rate, apparently due to the fact that beta is greater than one at a large radius, as described above. The finite-beta case is a more realistic representation of the solar corona than the force-free case (with $\beta = 0$), in which the flux tube kinking in the weak-field region is not impeded.

Figures 8 and 9 show that the kinked flux tube appears to settle to a new equilibrium state. This state does not appear to have any current sheets; the magnetic field remains smooth and free of discontinuities. In Fig. 10 we show the evolution of the total

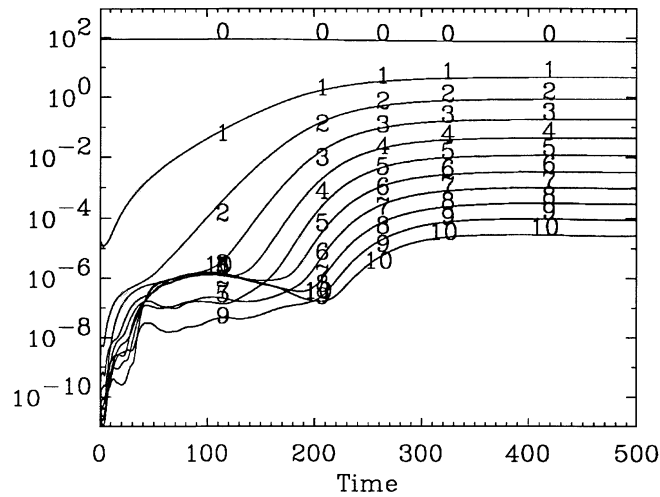


FIG. 8. Magnetic energy in various Fourier modes as a function of time for the nonlinear kink. The energy is normalized by the factor $E_o = B_o^2 a^3 / (8\pi)$.

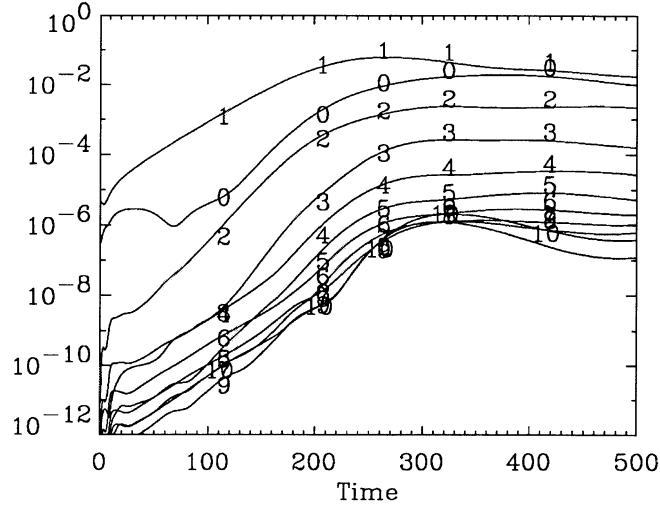


FIG. 9. Kinetic energy in various Fourier modes as a function of time for the nonlinear kink. The energy is normalized by the factor $E_0 = B_0^2 a^3 / (8\pi)$.

magnetic, kinetic, and thermal energies (defined by $W = \int [B^2 / 8\pi] dV$, $K = \int \frac{1}{2} \rho v^2 dV$, and $E = \int [p / (\gamma - 1)] dV$, respectively). Note that as the flux tube kinks, the magnetic energy is converted into kinetic energy and, finally, into thermal energy. The kinked flux tube approaches an equilibrium that has smaller magnetic energy than the initial state.

The large-scale kinking of the flux tube is best illustrated by traces of the magnetic field lines. In Fig. 11 we show traces at four instants of time. At $t = 100\tau_A$, during the linear stage, the kink is barely perceptible in the field line plot. At $t = 250\tau_A$ the kinking pattern is clearly visible. The traces at $t = 400\tau_A$ and $t = 500\tau_A$ show that the kink is saturating to a new equilibrium state.

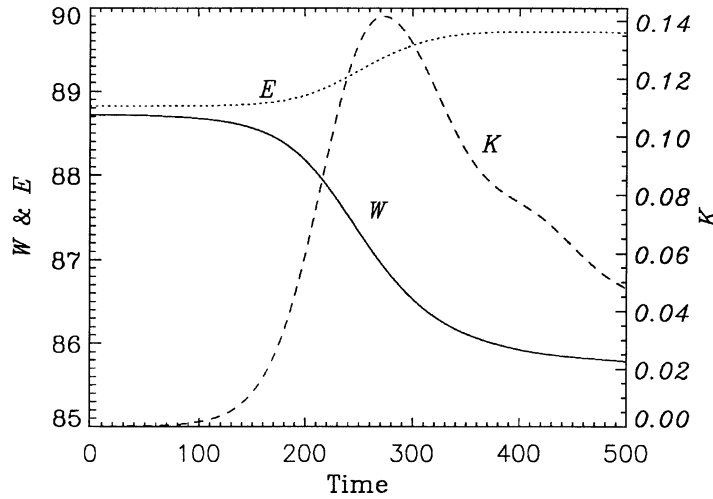


FIG. 10. The total magnetic, kinetic, and thermal energies (indicated respectively with W , K , and E) as functions of time for the nonlinear kink. The energy is normalized by the factor $E_0 = B_0^2 a^3 / (8\pi)$.

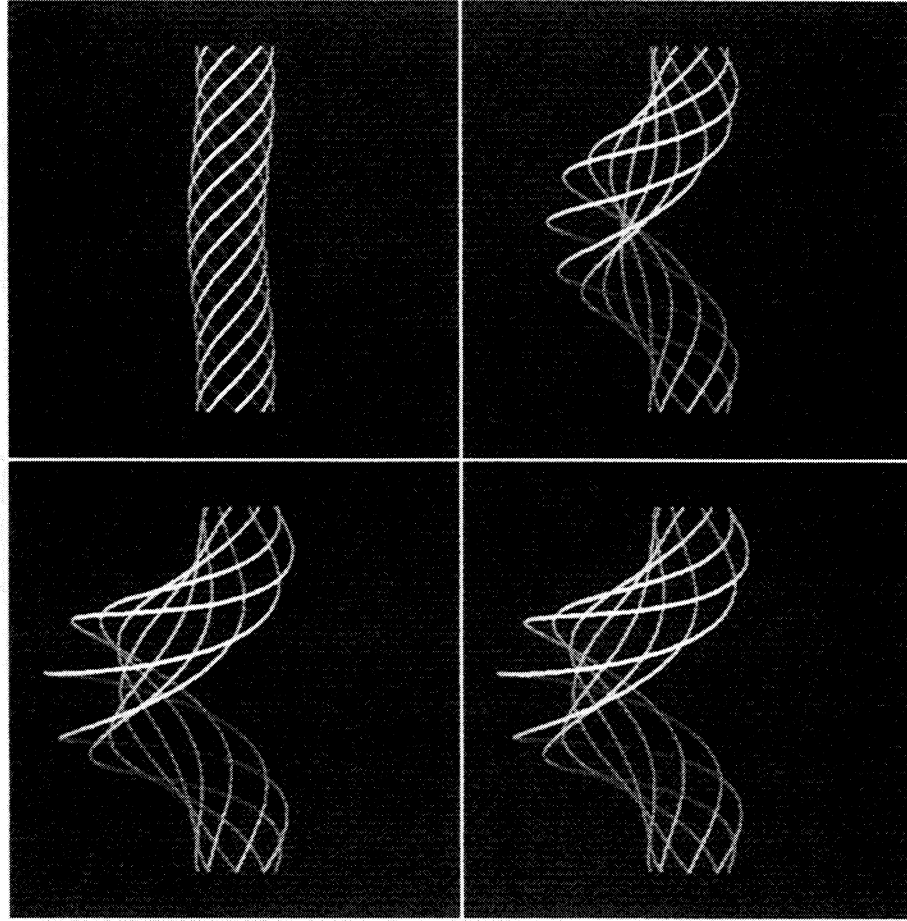


FIG. 11. Field line plots at $t = 100\tau_A$, $t = 250\tau_A$, $t = 400\tau_A$, and $t = 500\tau_A$. Field lines start from the bottom of the loop from a circle of radius a . Initially the kink pattern is barely visible, but when the instability saturates to a new equilibrium (third and fourth panel), the center of the loop has moved outward to about $r = 4a$.

5. CONCLUSIONS

We have presented a fast and accurate algorithm for the solution of the full resistive and viscous MHD equations in cylindrical coordinates in the presence of line-tied boundary conditions. The computer code based on this algorithm has been applied to the study of solar coronal flux tubes. In particular, the techniques are suited to the simulation of flux tubes whose footpoints are driven by slow photospheric motions.

The algorithm is implemented using finite differences in two dimensions, with pseudospectral derivatives along the third (periodic) dimension. The use of staggered finite-difference meshes preserves the solenoidal nature of the magnetic field and leads to a natural specification of boundary conditions on the tangential electric field and the normal magnetic field. Time advancement of the wave-like terms is performed with a leapfrog scheme. A semi-implicit operator is used in the momentum equation to give unconditional stability to wave-like terms. Advective terms are advanced using a predictor-corrector scheme, and therefore limit the time step by a Courant condition based on the flow speed. This allows

us to use significantly larger time steps than those achievable by a fully explicit algorithm. The viscous and resistive terms are discretized using a fully implicit time advance. The semi-implicit, viscous, and resistive operators are inverted using a preconditioned conjugate gradient method. Special care has been taken to maintain the self-adjointness of the discretized operators, so that a fast inversion algorithm applicable to symmetric matrices can be used.

To illustrate the application of the code, we have presented the nonlinear evolution of the ideal kink instability in the Gold–Hoyle uniform-twist field. Our results show that it is possible to follow the linear and nonlinear evolution of the kink instability. In the case of the Gold–Hoyle equilibrium, it appears that the kink instability saturates nonlinearly as the flux tube evolves to a new kinked equilibrium without the formation of current sheets. This result is in agreement with the results of Baty and Heyvaerts [25]. In contrast, Craig and Sneyd [24] concluded that the kink instability in the Gold–Hoyle field causes current sheets to form, a conclusion that is based on a calculation on a Lagrangian mesh whose accuracy is impaired when the mesh becomes significantly distorted by the finite-amplitude kink displacement. The evolution observed here for the Gold–Hoyle equilibrium contrasts sharply with the nonlinear evolution of the kink mode in a tokamak in which the nonlinear evolution causes current sheets (i.e., true discontinuities in the magnetic field) to form [27], a difference that has been attributed to the effect of line tying in the case of the coalescence instability by Longcope and Strauss [28]. In our case, it was thus possible to study the ideal MHD evolution. In general, instabilities can introduce current sheets, in which case it is necessary to study the resistive evolution. Equilibria in which the kink instability creates current sheets are discussed in [26, 29]. The role of a resonant surface in the formation of current sheets as a result of the nonlinear evolution of kink instabilities has been addressed previously [9, 25].

Therefore, the kink instability in the Gold–Hoyle equilibrium is not likely to play an important role in the solar corona, since it does not appear to cause significant heating or to lead to impulsive motions. On the other hand, other equilibria, in particular those in which the nonlinear evolution causes current sheets to form, leading to significant plasma heating, magnetic reconnection, and particle acceleration, are likely to be of interest in understanding coronal phenomena. Numerical algorithms and codes such as the one detailed here will be an important tool in this endeavor.

The code has also been used elsewhere [29, 26] to study the nonlinear evolution of instabilities in more realistic equilibria that are intended to model coronal loops formed by the twisting of uniform ambient fields and from the emergence of magnetic flux tubes from the photosphere. In these cases we have modeled the formation of current sheets, magnetic reconnection, and fast energy release.

APPENDIX A: FOURIER COEFFICIENTS IN POLAR COORDINATES

Let us consider a scalar function $F(x, y)$. We assume it is regular near the origin and we expand it in Taylor series

$$F(x, y) = F_0 + x \left. \frac{\partial F}{\partial x} \right|_0 + y \left. \frac{\partial F}{\partial y} \right|_0 + \frac{x^2}{2} \left. \frac{\partial^2 F}{\partial x^2} \right|_0 + \frac{y^2}{2} \left. \frac{\partial^2 F}{\partial y^2} \right|_0 + xy \left. \frac{\partial^2 F}{\partial x \partial y} \right|_0 + \cdots \quad (62)$$

Since $x = r \cos \theta$ and $y = r \sin \theta$, We can rewrite Eq. (62) as

$$\begin{aligned} F(x, y) = F_0 + r & \left[\frac{1}{2} \left(\frac{\partial F}{\partial x} \Big|_0 - i \frac{\partial F}{\partial y} \Big|_0 \right) e^{i\theta} + \frac{1}{2} \left(\frac{\partial F}{\partial x} \Big|_0 + i \frac{\partial F}{\partial y} \Big|_0 \right) e^{-i\theta} \right] \\ & + r^2 \left[\frac{1}{8} \left(\frac{\partial^2 F}{\partial x^2} \Big|_0 - 2i \frac{\partial^2 F}{\partial x \partial y} \Big|_0 - \frac{\partial^2 F}{\partial y^2} \Big|_0 \right) e^{i2\theta} + \frac{1}{4} \left(\frac{\partial^2 F}{\partial x^2} \Big|_0 + \frac{\partial^2 F}{\partial y^2} \Big|_0 \right) \right. \\ & \left. + \frac{1}{8} \left(\frac{\partial^2 F}{\partial x^2} \Big|_0 + 2i \frac{\partial^2 F}{\partial x \partial y} \Big|_0 - \frac{\partial^2 F}{\partial y^2} \Big|_0 \right) e^{-i2\theta} \right] + \dots \end{aligned} \quad (63)$$

Hence the r^n term is a certain combination of exponential functions $e^{im\theta}$, with $-n \leq m \leq n$. Since $e^{im\theta}$ may appear only when $n \geq |m|$ when we calculate the Fourier series of F , we obtain

$$\tilde{F}^{(m)}(r) = \sum_{n=|m|}^{\infty} c_n^{(m)} r^n. \quad (64)$$

Thus we have $\tilde{F}^{(m)}(r) = O(r^{|m|})$ for small r .

Let us consider now only one term of the Fourier series $a^{(m)}(x, y) = \tilde{F}^{(m)}(r) e^{im\theta}$. Notwithstanding r is always defined to be greater than zero, we notice that in an algebraic point of view we are allowed to write

$$r \rightarrow -r, \quad (65)$$

$$\theta \rightarrow \theta + \pi. \quad (66)$$

In this case x and y do not change and so

$$\tilde{F}^{(m)} e^{im\theta}(r) = \tilde{F}^{(m)}(-r) e^{im\theta} (-1)^m. \quad (67)$$

Let us expand both members of Eq. (67) in Taylor series around $r = 0$, obtaining

$$\sum_{n=|m|}^{\infty} c_n^{(m)} r^n (1 - (-1)^{n+m}) = 0. \quad (68)$$

This imposes the following condition on the Taylor series terms of the m th Fourier coefficient of $F(x, y)$,

$$c_n^{(m)} = 0 \begin{cases} n + m = 2k + 1 \\ k = 0, 1, 2, \dots \end{cases} \quad (69)$$

This means that the Taylor series of an even coefficient has only even terms and, vice versa, if m is odd only odd terms are found.

Let us examine now a vector $\mathbf{U} = (U_x, U_y)$, where the vector components $U_x(x, y)$ and $U_y(x, y)$ are scalar functions with the same properties of $F(x, y)$. The components of \mathbf{U} in polar coordinates are

$$U_r = U_x \cos \theta + U_y \sin \theta, \quad (70)$$

$$U_\theta = -U_x \sin \theta + U_y \cos \theta. \quad (71)$$

From this follows that the Fourier series coefficients are

$$\tilde{U}_r^{(m)} = \frac{1}{2} \left(\tilde{U}_x^{(m-1)} + \tilde{U}_x^{(m+1)} - i\tilde{U}_y^{(m-1)} + i\tilde{U}_y^{(m+1)} \right), \quad (72)$$

$$\tilde{U}_\theta^{(m)} = \frac{1}{2} \left(i\tilde{U}_x^{(m-1)} - i\tilde{U}_x^{(m+1)} + \tilde{U}_y^{(m-1)} + \tilde{U}_y^{(m+1)} \right). \quad (73)$$

Thus $\tilde{U}_r^{(m)}$ and $\tilde{U}_\theta^{(m)}$ are $O(r^{\min(|m-1|, |m+1|)})$. When m is even only odd terms of the Taylor series are found and vice versa. Note that for $r = 0$ and $m \geq 1$ the following equality holds:

$$\tilde{U}_r^{(m)} = -i\tilde{U}_\theta^{(m)}. \quad (74)$$

In cylindrical coordinates the third component U_z behaves as a scalar function.

APPENDIX B: STABILITY OF PREDICTOR-CORRECTOR ADVECTION ALGORITHMS

The typical advection equation in one dimension is

$$\frac{\partial f}{\partial t} + v \frac{\partial f}{\partial x} = 0. \quad (75)$$

To solve the equation above we employ the predictor-corrector algorithm

$$\begin{aligned} \frac{f_j^* - f_j^n}{\Delta t} &= -v Df^n, \\ \frac{f_j^{n+1} - f_j^n}{\Delta t} &= -\alpha v Df^* - (1 - \alpha)v Df^n, \end{aligned} \quad (76)$$

where $0 \leq \alpha \leq 1$. For centered differences

$$Df = \frac{f_{j+1} - f_{j-1}}{2\Delta x}, \quad (77)$$

while for upwind differences

$$Df = \begin{cases} \frac{f_j - f_{j-1}}{\Delta x} & \text{if } v > 0, \\ \frac{f_{j+1} - f_j}{\Delta x} & \text{if } v < 0. \end{cases} \quad (78)$$

The scheme above is first-order accurate in time. In order to perform a Von Neumann stability analysis we suppose that a local solution behaves like $f(j\Delta x, t_n) = z^n \exp(ikj\Delta x)$ and we assume for simplicity that $v > 0$. The amplification factor $z(k)$ must have modulus less than 1 for stability (see [30] for a more complete discussion of the method). Substituting f into Eq. (76) we obtain

$$z = 1 - \frac{v\Delta t}{\Delta x} Q \left(\alpha \frac{v\Delta t}{\Delta x} Q - 1 \right); \quad (79)$$

$$Q = \begin{cases} i \sin(k\Delta x) & \text{centered differences} \\ 1 - \cos(k\Delta x) + i \sin(k\Delta x) & \text{upwind differences.} \end{cases}$$

The case of centered differences and no predictor–corrector ($\alpha = 0$) yields $|z|$ always greater than one and is unconditionally unstable. If we introduce upwind differences then we have $|z| \leq 1$ when

$$v \frac{\Delta t}{\Delta x} \leq 1, \quad (80)$$

the so-called Courant condition. With the predictor–corrector and centered differences we obtain

$$\frac{2\alpha - 1}{\alpha^2} \geq \left(\frac{v \Delta t}{\Delta x} \right)^2 \quad (81)$$

for stability. For a fully advanced corrector ($\alpha = 1$) we find again the Courant condition. Using these methods introduces a numerical viscosity term

$$\nu_n \frac{\partial^2 f}{\partial x^2} \quad (82)$$

into Eq. (75), which is useful to damp small unresolved scales. Let us write $z = \exp(-i\omega_r \Delta t + \gamma \Delta t)$ and then find γ from Eq. (79), limiting ourselves to the case $k \Delta x \ll 1$. From Eq. (82) it follows that the numerical viscosity coefficient is $\nu_n = -\gamma/k^2$. With upwind differences and $\alpha = 0$ its value is

$$\nu \simeq \frac{v \Delta x}{2} \left(1 - \frac{v \Delta t}{\Delta x} \right), \quad (83)$$

and for $\alpha = 1$ and centered differences

$$\nu \simeq \frac{v^2 \Delta t}{2}. \quad (84)$$

The situation in the code is complicated, with respect to this simple example, by the presence of nonuniform three-dimensional meshes in a non-Cartesian frame of reference. Furthermore, the conditions above are only *necessary* and not sufficient for stability. Fully advanced predictor–corrector is used to stabilize advection in the periodic direction θ , since we cannot upwind θ -derivative. We normally combine this method with upwind differences in r and z , originating the stability condition showed in Eq. (19) since both must obey the Courant condition.

APPENDIX C: POSITIVE DEFINITENESS OF A SYMMETRIC TRIDIAGONAL MATRIX

Let us consider a symmetric tridiagonal matrix A of the form:

$$A_{i,i} = \begin{cases} c_2 + b_1 + b_2 + C_0 b_1, & i = 2, \\ c_i + b_{i-1} + b_i, & 3 \leq i \leq N-2, \\ c_{N-1} + b_{N-2} + b_{N-1} + C_L b_{N-1}, & i = N-1, \end{cases} \quad (85)$$

$$A_{i,i+1} = b_i \quad 2 \leq i \leq N-2$$

$$A_{i,i-1} = b_{i-1} \quad 3 \leq i \leq N-1,$$

where c_i and b_i are positive and C_0 and C_L may be either 1 or -1 . A matrix A is positive definite if and only if

$$x \cdot A \cdot x \geq 0 \quad \forall x \neq 0. \quad (86)$$

The condition above becomes for our matrix

$$\sum_{i=2}^{N-1} x_i^2 (c_i + b_i + b_{i-1}) + \sum_{i=3}^{N-1} x_i x_{i-1} b_{i-1} \quad (87)$$

$$+ \sum_{i=2}^{N-2} x_i x_{i+1} b_i + x_2^2 b_1 C_0 + x_{N-1}^2 b_{N-1} C_L \geq 0. \quad (88)$$

We can rewrite it as

$$\sum_{i=2}^{N-1} x_i^2 c_i + \sum_{i=2}^{N-2} b_i (x_i - x_{i+1})^2 + x_2^2 b_1 (1 + C_0) + x_{N-1}^2 b_{N-1} (1 + C_L) \geq 0, \quad (89)$$

that is manifestly true.

ACKNOWLEDGMENTS

We would like to thank Claudio Chiuderi, Giorgio Einaudi, Jon Linker, Gerard Van Hoven, and Marco Velli for many helpful discussions. Computations were performed at the Interuniversity Consortium of the Northeastern Italy for Automatic Computing (CINECA) and at the National Energy Research Supercomputer Center (NERSC) at Livermore, California. This work was supported in part by a NASA contract to Science Applications International Corporation (SAIC). One of us (RL) wishes to thank Roberto Casini for collaboration in developing imaging software; the University of California at Irvine, and SAIC for their kind hospitality during the development of this work. The visit of RL to UCI was supported, in part, by NSF and NASA.

REFERENCES

1. B. M. Haisch and M. Rodonò (Eds.), *Solar and Stellar Flares* (Kluwer Academic, Dordrecht, 1989).
2. P. Ulmschneider, E. R. Priest, and R. Rosner (Eds.), *Mechanisms of Chromospheric and Coronal Heating* (Springer-Verlag, Berlin, 1991).
3. G. Belvedere, M. Rodonò, and G. M. Simnett (Eds.), *Advances in Solar Physics* (Springer-Verlag, Berlin, 1994).
4. E. N. Parker, *Spontaneous Current Sheets in Magnetic Fields with Applications to Stellar X-rays* (Oxford Univ. Press, New York, 1994).
5. G. Van Hoven, Y. Mok, and Z. Mikić, Coronal loop formation resulting from photospheric convection, *Astrophys. J.* **440**, L105 (1995).
6. A. W. Hood and E. R. Priest, Critical conditions for magnetic instabilities in force-free coronal loops, *Geophys. Astrophys. Fluid Dyn.* **17**, 297 (1981).
7. G. Einaudi and G. Van Hoven, The stability of coronal loops: finite-length and pressure-profile limits, *Sol. Phys.* **88**, 163 (1983).
8. M. Velli, G. Einaudi, and A. W. Hood, Boundary effects on the magnetohydrodynamic stability of a resistive plasma, *Astrophys. J.* **350**, 419 (1990).
9. M. Velli, G. Einaudi, and A. W. Hood, Ideal kink instabilities in line-tied coronal loops: growth rates and geometrical properties, *Astrophys. J.* **350**, 428 (1990).

10. A. Y. Aydemir and D. C. Barnes, An implicit algorithm for compressible three-dimensional magnetohydrodynamic calculations, *J. Comput. Phys.* **59**, 108 (1985).
11. D. S. Harned and W. Kerner, Semi-implicit method for three-dimensional compressible magnetohydrodynamic simulations, *J. Comput. Phys.* **60**, 62 (1985).
12. D. S. Harned and D. D. Schnack, Semi-implicit method for long time scale magnetohydrodynamic computations in three dimensions, *J. Comput. Phys.* **65**, 57 (1986).
13. D. D. Schnack, D. C. Barnes, Z. Mikić, D. S. Harned, and E. J. Caramana, Semi-implicit magnetohydrodynamic calculation, *J. Comput. Phys.* **70**, 330 (1987).
14. K. Lerbinger and J. F. Luciani, A new semi-implicit method for MHD computations, *J. Comput. Phys.* **97**, 444 (1991).
15. Z. Mikić, D. D. Schnack, and G. Van Hoven, Dynamical evolution of twisted magnetic flux tubes. I. Equilibrium and linear stability, *Astrophys. J.* **361**, 690 (1990).
16. G. H. Golub and C. F. Van Loan, *Matrix Computations* (Johns Hopkins Univ. Press, 1989), p. 516.
17. Z. Mikić and E. C. Morse, The use of a preconditioned bi-conjugate gradient method for hybrid plasma stability analysis, *J. Comput. Phys.* **61**, 154 (1984).
18. D. Gottlieb and S. A. Orszag, *Numerical Analysis of Spectral Methods* (SIAM, Philadelphia, 1977).
19. Z. Mikić, to be published.
20. D. D. Schnack, D. C. Baxter, and E. J. Caramana, A pseudospectral algorithm for three-dimensional magnetohydrodynamic simulation, *J. Comput. Phys.* **55**, 485 (1984).
21. Z. Mikić, Magnetohydrodynamic modeling of the solar corona, *Phys. Fluids B* **2**, 1450 (1990).
22. T. Gold and F. Hoyle, On the origin of solar flares, *Mon. Not. R. Astron. Soc.* **120**, 89 (1960).
23. B. J. Foote and I. J. D. Craig, The linear stability of line-tied coronal magnetic fields, *Astrophys. J.* **350**, 437 (1990).
24. I. J. D. Craig and A. D. Sneyd, Nonlinear development of the kink instability in coronal flux tubes, *Astrophys. J.* **357**, 653 (1990).
25. H. Baty and J. Heyvaerts, Electric current concentration and kink instability in line-tied coronal loops, *Astron. Astrophys.* **308**, 935 (1996).
26. M. Velli, R. Lionello, and G. Einaudi, Kink modes and current sheets in coronal loops, *Sol. Phys.* **172**, 257 (1996).
27. M. N. Rosenbluth, R. Y. Dagazian, and P. H. Rutherford, Non-linear properties of the internal kink instability in the cylindrical tokamak, *Phys. Fluids* **16**, 1894 (1973).
28. D. W. Longcope and H. R. Strauss, The form of ideal current layers in line-tied magnetic fields, *Astrophys. J.* **437**, 851 (1994).
29. G. Einaudi, R. Lionello, and M. Velli, Magnetic reconnection in solar coronal loops, *Adv. Space Res.* **19**, 1875 (1997).
30. W. H. Press, B. P. Flannery, Saul A. Teukolsky, and W. T. Vetterling, *Numerical Recipes* (Cambridge Univ. Press, Cambridge, 1986).

A Finite-Volume Algorithm for Three-Dimensional Magnetohydrodynamics on an Unstructured, Adaptive Grid in Axially Symmetric Geometry

D. D. Schnack,^{*} I. Lottati,[†] Z. Mikić,^{*} and P. Satyanarayana[†]

^{*}*Science Applications International Corporation, 10260 Campus Point Drive, San Diego, California 92121-1578; †Science Applications International Corporation, 1710 Goodridge Drive, McLean, Virginia 22102*
E-mail: schnack@iris023.saic.com

Received September 20, 1996; revised July 10, 1997

A new finite-volume algorithm for the solution of the time-dependent, nonideal magnetohydrodynamic (MHD) equations in cylindrical (r, ϕ, z) geometry is presented. The boundary geometry is assumed to be axially symmetric, but it can have arbitrary shape and connectivity in the poloidal (r, z) plane. The dynamics of the fluid is fully three-dimensional. A two-dimensional, unstructured, adaptive grid of triangles is used to describe the poloidal geometry. A pseudospectral algorithm with fast Fourier transforms is used for the periodic toroidal (ϕ) direction. The grid can be dynamically refined or coarsened by adding or deleting points to adapt to evolving fine-scale structures in the solution. The algorithm exactly conserves total mass, momentum, energy, and magnetic flux, and identically preserves the solenoidal properties of the magnetic field and the current density. Examples of the application of the algorithm to two-dimensional hydrodynamic and MHD shocks, the linear growth of a resistive tearing instability in a tokamak, and the linear growth and nonlinear saturation of three-dimensional kink instabilities in toroidal geometry are given. © 1998 Academic Press

1. INTRODUCTION

Over the past two decades, large scale numerical simulation has played an important role in fusion plasma research. Applications of these techniques to fluid plasma models have led to an interpretation of sawtooth [1] and fishbone oscillations [2–4] in tokamaks, the tokamak major disruption [5], the tilting mode in field-reversed configurations [6], and to a fundamental understanding of the reversed-field pinch dynamo [7]. These calculations

were generally performed on spatial grids aligned with fixed coordinate directions. As a result, these calculations were often carried out in generic toroidal or cylindrical geometry.

Many important engineering and theoretical issues are affected by the details of the geometry. For example, the poloidal plasma shape can greatly influence the linear stability properties of a fusion plasma, and these linear calculations are now routinely performed with the actual poloidal plasma geometry accurately represented. This is often accomplished by employing a coordinate system based on the magnetic field lines, whose geometry is fixed throughout the calculation. The resulting metric makes the fluid equations quite complicated, but it allows the coordinate system to naturally fit the plasma shape.

While coordinate systems based on magnetic fields have proven useful in linear calculations that principally determine eigenvalues and eigenvectors, they have several disadvantages in fully nonlinear simulations because of the dynamical nature of the magnetic field. Primary among these is the nonuniqueness of the magnetic topology when finite resistivity is included in the model. These coordinate systems also may become singular at magnetic separatrices, which are essential features of modern tokamaks.

It is thus desirable for fully nonlinear simulations to employ a spatial representation that can readily conform to the geometric details of the plasma and its surroundings and is independent of the magnetic structure. For accuracy, this representation should also be capable of conforming to the dynamical evolution of short spatial scale structures, such as current filaments and density gradients that may appear spontaneously and require finer spatial resolution than the surrounding environment.

One candidate for a spatial representation with these features is an *unstructured, adaptive mesh*. In such a mesh the mesh points are not constrained to lie along constant coordinate directions. Instead, mesh points are placed on the boundary to conform with the actual geometry of the problem and are distributed in space to maximize the accuracy of the calculation. Thus placed, the points are connected with line elements that form the edges of triangles (see Fig. 1). These triangles are the Eulerian control volumes that form the basis for the finite representation of the appropriate fluid equations. In the logical data structure that describes the mesh, mesh points (and associated triangles) can easily be added or deleted dynamically, based on predefined accuracy criteria. The spatial representation can thus adapt to evolving spatial structures without the mesh distortion problems associated

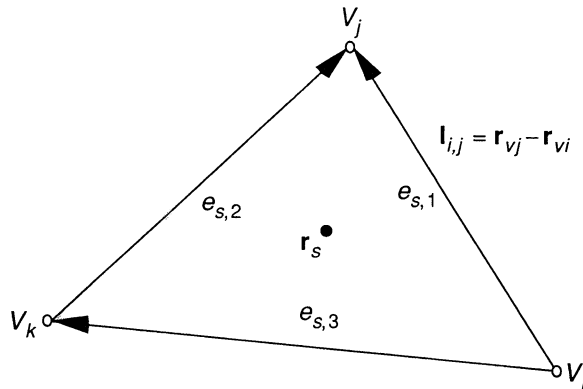


FIG. 1. Triangle, edge, and vertex mesh elements.

with Lagrangian formulations. Also, since the placement of the mesh points is not tied to a magnetic field, separatrices and X-type neutral points can be readily resolved.

Techniques based on unstructured, adaptive meshes have come to maturity in computational fluid dynamics (CFD), where quantitative predictions in real geometry have become essential in the design of aircraft and gas turbine engines [8]. These methods are generally based the solution of a Riemann problem at each triangle interface (edge) to determine the fluxes of energy, mass, and momentum [9]. The simplest extension of the hydrodynamic model that is appropriate for the description of magnetic fusion plasmas is magnetohydrodynamics (MHD).

In this paper we describe an extension of these spatial gridding techniques to an MHD model suitable for the description of the fully three-dimensional dynamics of plasmas with axially symmetric geometry, such as toroidal fusion devices. Since the dominant MHD modes in this geometry have relatively long toroidal wavelength, the toroidal coordinate is approximated with finite Fourier series. The unstructured, triangular mesh is used to describe the details of the poloidal geometry. The hydrodynamic variables are treated in a manner analogous to that used in CFD. These quantities (mass, momentum, and energy) are volume based densities that satisfy scalar or vector conservation laws. The electromagnetic variables (the magnetic flux density \mathbf{B} and the electric current density \mathbf{J}) are area-based densities that satisfy pseudo-vector conservation laws and have no counterpart in fluid dynamics. These variables are constrained to remain solenoidal. These quantities are represented on the triangular mesh in a manner that is an extension of that used on rectangular, structured meshes.

In this work we have chosen to solve the primitive (instead of reduced [10–12]) MHD equations in order to make the resulting codes and techniques more generally applicable to problems beyond the narrow scope of tokamak plasmas. The temporal stiffness problems inherent in this description of tokamak dynamics that motivate the reduced MHD model are addressed here with the semi-implicit method of time integration [13–16]. We remark that, while the present work deals strictly with the MHD equations, other volume-based fluid descriptions, such as diffusive transport, could easily be adapted to these techniques and coupled with the description of the electromagnetic field presented here.

We emphasize that a primary goal of this work is to develop an algorithm for the description of slow, nonlinear, long wavelength motions in toroidal geometry with arbitrary poloidal shape. We have therefore used several low-order approximations that may be inappropriate for problems in which the highly accurate description of strong shocks is required. The solution of such problems will require extensions of the work described here. Nonetheless, the present algorithm can reasonably describe shock formation and propagation at relatively low Mach number.

This paper is organized as follows. In Section 2 we discuss the properties of structured and unstructured meshes, and the data structures useful for describing them. Issues related to the triangulation of an arbitrary set of points in a plane are also discussed. In Section 3 we derive a finite volume approximation to the resistive MHD equations suitable for use on an unstructured, triangular mesh in toroidal geometry. Boundary conditions are discussed here. The specific MHD model and its implementation on the unstructured mesh are discussed in Section 4. In Section 5 we discuss methods of time integration and describe our implementation of semi-implicit and fully implicit algorithms. Examples of the application of the method are given in Section 6. Included are standard, two-dimensional hydrodynamic and MHD shock problems, as well as applications of the method to the stability and nonlinear

evolution of toroidal fusion plasmas in three dimensions. The summary and discussion are given in Section 7.

2. COMPUTATIONAL MESHES

Continuous systems described by partial differential equations respond to differences between the state of the system at one spatial location and the state at another spatial location that is only infinitesimally distant. The state of the system is defined on a continuum of points in the domain. In a finite analog of such a system, the infinity of points in the continuum is replaced by a finite number of discrete points, and the infinitesimal distance is replaced by the finite distance between neighboring points. For the purposes of computing the differences in the state of the system between these points, near neighboring points can be thought of as being linked together to form a mesh that covers the domain. The description of the mesh consists of a list of the mesh points and their connectivity. The physical relationships between the state of the system at one mesh point and that at all others then defines a finite-dimensional set of nonlinear algebraic equations that are the exact equations of motion for the finite system. The extent to which the dynamics of this finite-dimensional system approximate those of the continuum system determines the accuracy and utility of the approximation.

The computational description of a continuous, time-dependent system, such as a magnetized plasma, has three components: a continuum model of the system that describes the evolution of infinitesimally small volume elements for infinitesimally small intervals of time; an approximation to the continuum model that describes the evolution of finite sized volume elements for infinitesimally small intervals of time; and a description of how these finite-sized volume elements evolve over finite time intervals. In this work we have chosen resistive magnetohydrodynamics as the continuum model. This will be described in Section 3. The finite temporal description will be given in Section 5. Here, and in Section 4, we will discuss finite methods of spatial representation.

2.1. Structured Meshes

A *structured* mesh is one in which a predefined logical structure (or order) is assumed to exist. For example, in 2D Cartesian coordinates, a structured mesh consists of a product of two sets of mesh arrays (the x and y coordinates), with indices i and j , ordered by increasing coordinate value. Two indices are required to identify a mesh point: point (i, j) has coordinates $x(i)$, $y(j)$. The mesh is structured logically so that points $(i+1, j)$ and $(i, j+1)$ are adjacent to point (i, j) . This logical structure is assumed to hold for all points in the domain and is implicitly used in constructing the finite-dimensional algebraic equations that describe the dynamical evolution of the finite system. Structured meshes form the familiar quadrilateral grids commonly used in numerical methods. The boundary of the domain naturally consists of curves of the form $x = \text{const}$ and $y = \text{const}$. (An irregular domain would be built up from unions of such meshes.) As neighboring points are logically connected in this way, adding and deleting points affects the indexing of *all* points in the mesh.

2.2. Unstructured Meshes

In contrast to a structured mesh, an *unstructured* mesh is one that has no predefined logical structure. An unstructured mesh consists of a set of arbitrarily ordered points. A single mesh index suffices to identify a point. Point r_i , having coordinates x_i and y_i , and point $i+1$, having coordinates x_{i+1} and y_{i+1} , are not necessarily adjacent.

Since there is no pre-defined logical structure, the mesh points are not constrained to lie along any predetermined curves; they may be arbitrarily distributed in the domain. Neighboring points are then connected by line elements to form a mesh of triangles that covers the domain. The mesh points \mathbf{r}_i form the vertices of the triangles, and the connecting lines form the triangle edges. The mesh consists of N_v vertices, N_e edges, and N_s triangles, with $N_v < N_s < N_e$.

With each triangle s we will associate a point r_s . This point identifies the location of the triangle in the domain. (The definition of r_s is not unique. This will be discussed in Sections 2.4 and 2.5.) It is also convenient to define the edges of the triangles as directed line segments, or vectors $\mathbf{l}_{i,j}$, connecting point i with point j , i.e., $\mathbf{l}_{i,j} = \mathbf{r}_j - \mathbf{r}_i$. Every edge e thus has triangle $s + L$ on the left, and triangle $s = R$ on the right. With each edge we also associate a unit tangent vector $\mathbf{t}_e = \mathbf{l}_e / l_e$, and a unit normal vector \mathbf{n}_e that points from the left side to the right side. These mesh elements are sketched in Figure 1.

An unstructured mesh is identified and manipulated by means of primary and secondary data sets. The primary data set consists of a list of mesh elements. Secondary data sets define the connectivity between the primary mesh elements. For example, for 2D meshes the spatial representation consists of triangular elements. The primary data set consists of a list of cells (triangles), their vertices, and the edges connecting them. Additional data sets consist of cross-indexing information that relate the elements of the primary set. For example, an edge-indexed array specifies the indices of the cells to the left and right of an edge. Other cell-indexed arrays specify the indices of the three vertices and three edges of a cell.

2.3. Primary and Dual Meshes

Computational meshes, both structured and unstructured, are used not only to describe geometric regions, but also to define differential operators. For the latter purpose, it is useful to introduce the concept of primary and dual meshes. For a structured mesh, these are often referred to as staggered meshes. An example of a two-dimensional structured, staggered mesh is shown in Fig. 2.

In a finite-volume representation, different control volumes are used for different dependent variables. For example, some dependent variables are defined on at the vertices of the primary mesh; the control volume associated with these quantities is a rectangle formed by the dual mesh. Other quantities are defined at the vertices of the dual, or staggered, mesh; the control volume associated with these quantities is a rectangle formed by the primary mesh. Meshes of this type have been used successfully in MHD simulation [16].

The concept of primary and dual meshes can be extended to triangular meshes. In this case the primary mesh consists of the triangulation of arbitrarily placed points in the plane. The mesh points are the vertices of the triangles. The dual mesh consists of polygons that surround each vertex. The vertices of the dual polygons can be chosen in several ways. Two choices will be discussed below. When taken together, the primary triangular mesh and the dual polygon mesh are the generalization of structured, staggered meshes. An example of a triangular mesh and its polygon dual are sketched in Fig. 3.

2.4. The Barycenter, or Centroid, Dual Mesh

We use a Delaunay triangulation [17] for the primary mesh. The Delaunay triangulation maximizes the minimum angle of the triangulation; i.e., of all triangulations of the set P the Delaunay triangles are the closest to being equiangular, on average. Because of this

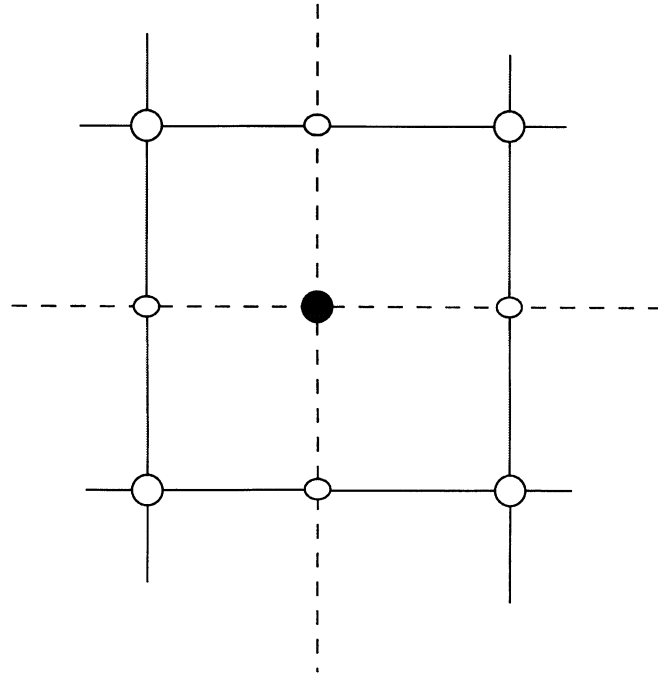


FIG. 2. Structured, staggered (dual) meshes.

property, these triangles are chosen as the primary control volumes. We use a dual mesh whose vertices are the centroids, or barycenters, of each triangle. If the coordinates of the triangle vertices (the points P) are \mathbf{r}_v , the coordinates of the vertices of the dual mesh are given by

$$\mathbf{r}_s = \frac{1}{3}(\mathbf{r}_{v1} + \mathbf{r}_{v2} + \mathbf{r}_{v3}), \quad s = 1, 2, \dots, N_s, \quad (1)$$

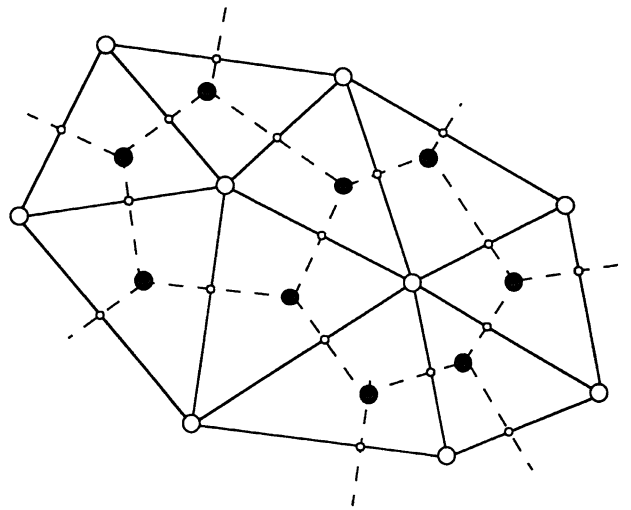


FIG. 3. Triangular (primary) and polygon (dual) meshes.

where N_s is the number of triangles and the \mathbf{r}_{vi} are the three vertices of triangle s . This dual mesh has the property that the vertices of the polygons are always interior to their corresponding triangles. However, the edges of the dual meshes are not orthogonal, as in the Voronoi dual mesh [17]. This complicates the calculation of some dependent variables, as will be discussed in Section 4.

2.5. The Third (Toroidal) Dimension

One goal of this work is to describe magnetohydrodynamics in toroidal fusion systems. The geometry of these systems is symmetric about an axis, and is best described in cylindrical (r, ϕ, z) coordinates. We use the unstructured Delaunay triangular mesh and the barycenter dual mesh dual to approximate the geometry in the poloidal (r, z) plane. Since the angular (ϕ) coordinate is periodic and since the dominant MHD motions in this geometry are long wavelengths in this direction, we have chosen a pseudospectral description using fast Fourier transforms (FFTs) for this coordinate. The toroidal mesh is thus structured with a uniform mesh spacing $\Delta\phi = 2\pi/N_\phi$, where N_ϕ is the number of toroidal mesh points; N_ϕ must be a power of 2.

The three-dimensional control volume is sketched in Fig. 4. The elemental volume is $\Delta V_s = r_s \Delta\phi \Delta a_s$, where Δa_s is the planar area of triangle s and r_s is the radius of the triangle centroid. The Pappus–Guldinus theorem guarantees that this formula is exact.

2.6. Mesh Refinement

The use of an unstructured mesh allows for new triangles to be added and old ones deleted in a relatively easy manner. Here we use the method of direct dynamic refinement [18] (DDR). In this method the mesh is refined or coarsened automatically during the execution of the algorithm, according to predetermined criteria. New triangles are added to the end of the list, and old triangles are deleted and the list shortened. A new triangle is added by introducing a new vertex at the centroid of a triangle to be refined. New edges

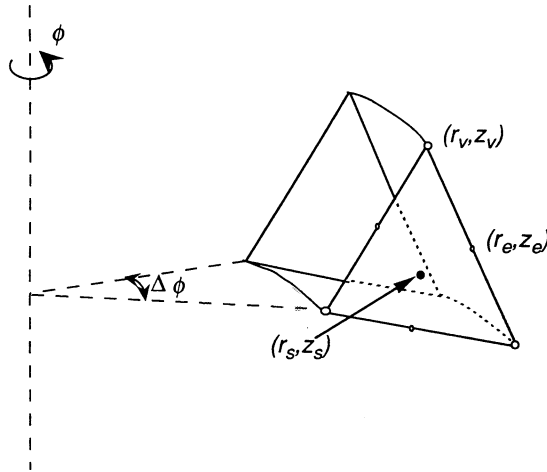


FIG. 4. Three-dimensional control volume.

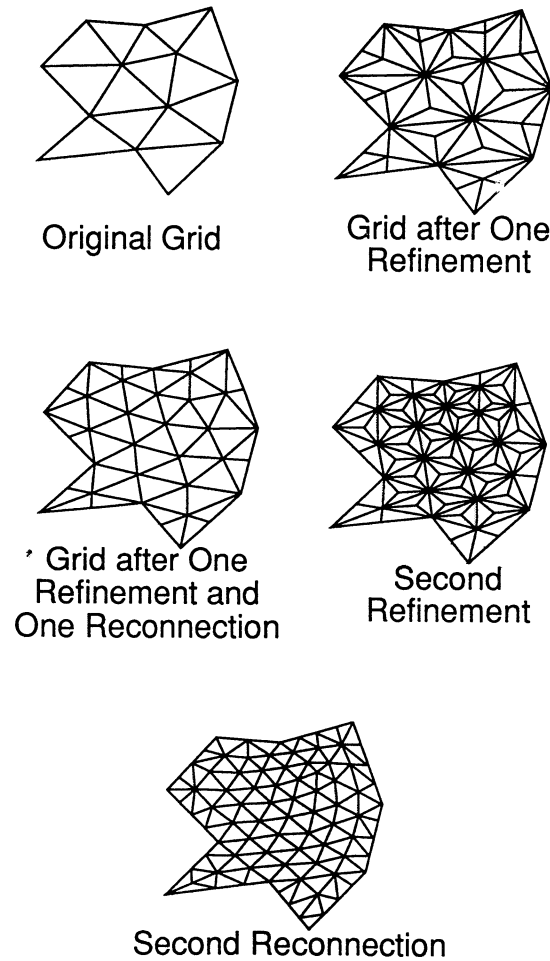


FIG. 5. Mesh refinement and edge swapping (from [18]).

connect this vertex to the three vertices of the original triangle. The original triangle is thus divided into three, and two new triangles, three new edges, and one vertex are added to the lists. The new edges may need to be swapped between the new vertex and the opposing vertices of the three neighboring triangles. The circumcenter test [19] is used to determine whether or not edge swapping is required. The new triangulation is thus as acute as possible. The addition of a vertex and edge swapping are sketched in Fig. 5. Triangle deletion is sketched in Fig. 6. Edges of triangles may also be subdivided. The triangle centered densities (mass, momentum, energy, and toroidal vector potential) can then be distributed over the new triangles in a conservative manner. Edge centered quantities (poloidal vector potential) are interpolated to the new mesh using the methods described in Section 4.3.

Before adaption can occur a triangle must be identified for refinement or coarsening. We have used several criteria for this purpose. Different criteria may be useful for different problems. One criterion is based on a modified version of the classic interpolation estimate originally developed for steady-state hydrodynamic computations [20, 21]. For each triangle

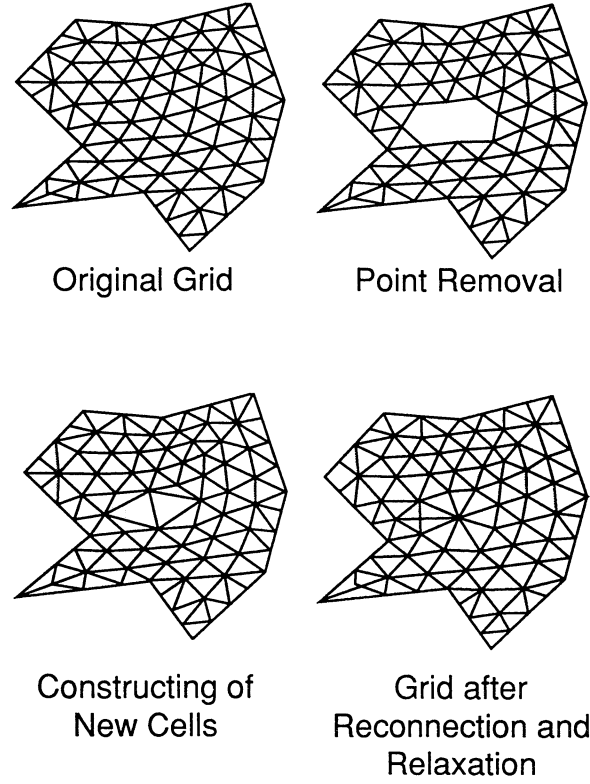


FIG. 6. Mesh coarsening (from [18]).

s , we compute the normalized second derivative,

$$E_s = \frac{\delta_s^2 \overline{|\nabla^2 U_s|}}{\delta_s \overline{|\nabla U_s|} + \varepsilon \overline{|U_s|}}, \quad (2a)$$

where $\delta_s = \sqrt{\Delta a_s}$, U_s is any triangle-centered dependent variable, ε is a constant between 0 and 1 (typically, $\varepsilon = 0.2$), and the overscore indicates an average over triangle s and its three neighbors. (For three-dimensional problems, the maximum of E_s over the toroidal dimension is taken.) In (2a), the quantity E_s is dimensionless and bounded, so that it can be used for a variety of problems and dependent variables. Another criterion is based on the normalized average gradient:

$$E_s = \frac{\delta_s \overline{|\nabla U_s|}}{U_{\max}}. \quad (2b)$$

For either criterion (2a) or (2b), all triangles for which $E_s > E_R$ are refined, while all triangles for which $E_s < E_C$ are coarsened.

We have found that the proper choices of E_R and E_C are as much an art form as they are anything else. Choosing too small a value for E_R can result in too much refinement and, hence, too many triangles. Refinement is done on numerical noise rather than on physical structures. Choosing E_R too large can result in patchy refinement and poor resolution. The

proper choices of E_R and E_C also seem to be problem dependent. Much trial and error is required. A rule of thumb is to start with $E_R = 0.9$ and $E_C = 0.1$, and make small variations until a satisfactory grid results.

As mesh refinement and coarsening are time-consuming operations they are not done every timestep. Mesh refinement is done after every N_R timesteps, and coarsening is done after every N_C refinement steps. Values of N_R from 5 to 20, and N_C from 1 to 4, are typical. Examples of refinement and coarsening are given in Section 6.

3. APPROXIMATION TO SPATIAL DIFFERENTIAL OPERATORS

The differential operators that appear in fluid-like equations are the gradient of a scalar, the divergence of both a vector and a tensor, and the curl of vector. We now proceed to define approximations to these operators on the triangular, unstructured mesh. We use the method of finite volumes as applied to the three-dimensional volume element shown in Fig. 4.

Consider the triangle in the poloidal (r, z) plane shown in Fig. 7. We define normal and tangent unit vectors \mathbf{n}_e and \mathbf{t}_e at each edge such that

$$\mathbf{e}_\phi = \mathbf{t}_e \times \mathbf{n}_e, \quad (3)$$

where \mathbf{e}_ϕ is the toroidal unit vector. (Note that \mathbf{e}_ϕ points “into” the page.) The normal and tangent unit vectors are given by

$$\mathbf{l}_e = \Delta r_e \mathbf{e}_r + \Delta z_e \mathbf{e}_z = \Delta l_e \mathbf{t}_e \quad (4)$$

$$\mathbf{n}_e = \frac{\Delta z_e \mathbf{e}_r - \Delta r_e \mathbf{e}_z}{\Delta l_e} \quad (5)$$

and the area of the triangle is

$$\Delta a_s = \frac{1}{2} |\mathbf{l}_1 \times \mathbf{l}_2| = \frac{1}{2} |\mathbf{l}_2 \times \mathbf{l}_3| = \frac{1}{2} |\mathbf{l}_3 \times \mathbf{l}_1|. \quad (6)$$

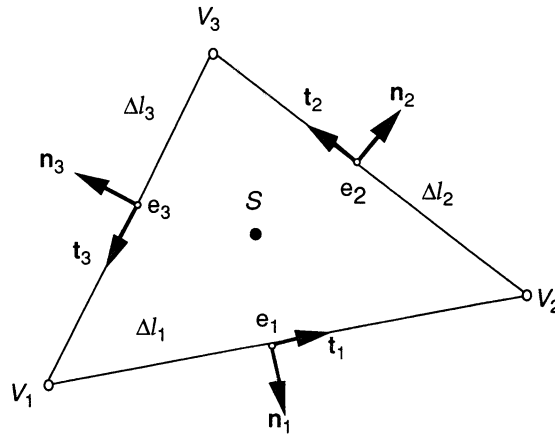


FIG. 7. Poloidal projection of control volume.

The unit normal vector \mathbf{n}_e points from the left side of edge e (triangle $s = L_e$) to the right side of edge e (triangle $s = R_e$).

The finite volume method is used to obtain the approximations to the differential operators. In this method differential operators are defined in terms of their integral relations. We assume all functions are of the form

$$f(r, \phi, z, t) = \sum_n f_n(r, z, t) e^{in\phi} \quad (7)$$

and then we integrate the appropriate identity over the three-dimensional control volume shown in Fig. 4. (Since the toroidal representation is spectral and not finite-difference, the limit of the resulting expressions as $\Delta\phi \rightarrow 0$ is taken.) This technique assures that the same integral relationships are obeyed by the finite difference approximations and their equivalent differential operators.

To obtain an approximation for the *gradient of a scalar* we substitute Eq. (7) into the integral identity

$$\int \nabla f dV = \oint f \mathbf{n} ds, \quad (8)$$

and use second-order approximations to the volume and surface integrals to obtain

$$(\nabla f)_s = \frac{1}{r_s \Delta a_s} \sum_{e=1}^3 r_e \Delta l_e \mathbf{n}_e \bar{f}_e - \frac{f_s}{r_s} \mathbf{e}_r + \frac{in}{r_s} f_s \mathbf{e}_\phi. \quad (9)$$

The sum is taken over the three edges of triangle s , and the radius of edge e is $r_e = (r_{ve1} + r_{ve2})/2$, where r_{ve1} and r_{ve2} are the radial coordinates of the vertices connected by edge e . The quantity \bar{f}_e is the simple average $\bar{f}_e = (f_{Re} + f_{Le})/2$, where the values f_{Re} and f_{Le} are the values of f_s in the triangles lying to the right (R_e) and left (L_e) of edge e .

Similarly, for the *divergence of a vector* we use the identity

$$\int \nabla \cdot \mathbf{A} dV = \oint \mathbf{n} \cdot \mathbf{A} dS \quad (10)$$

to obtain the approximation

$$(\nabla \cdot \mathbf{A})_s = \frac{1}{r_s \Delta a_s} \sum_{e=1}^3 r_e \Delta l_e \mathbf{n}_e \cdot \mathbf{A}_e + \frac{in}{r_s} A_{\phi s}; \quad (11)$$

for the curl of a vector we use

$$\int \nabla \times \mathbf{A} dS = \oint \mathbf{t} \cdot \mathbf{A} dl \quad (12)$$

to obtain the approximation

$$(\nabla \times \mathbf{A})_{ne} = -\frac{1}{r_e \Delta l_e} (r_{v+} A_{\phi v+} - r_{v-} A_{\phi v-}) + \frac{in}{r_e} \mathbf{A}_e \cdot \mathbf{t}_e, \quad (13)$$

$$(\nabla \times \mathbf{A})_{\phi s} = -\frac{1}{\Delta a_s} \sum_{e=1}^3 \mathbf{A}_e \cdot \mathbf{l}_e. \quad (14)$$

Here we have taken surface and line integrals over the faces of the control volume and their respective bounding edges. To approximate the *divergence of a tensor* we use

$$\int \nabla \cdot \mathbf{T} dV = \oint \mathbf{n} \cdot \mathbf{T} dS \quad (15)$$

to obtain

$$\begin{aligned} (\nabla \cdot \mathbf{T})_s = & \frac{1}{r_s \Delta a_s} \sum_{e=1}^3 r_e \Delta l_e [\mathbf{e}_r (\mathbf{n}_e \cdot \mathbf{T}_e)_r + \mathbf{e}_\phi (\mathbf{n}_e \cdot \mathbf{T}_e)_\phi + \mathbf{e}_z (\mathbf{n}_e \cdot \mathbf{T}_e)_z] \\ & + \frac{in}{r_s} [\mathbf{e}_r T_{\phi rs} + \mathbf{e}_\phi T_{\phi \phi s} + \mathbf{e}_z T_{\phi zs}] + \frac{1}{r_s} [\mathbf{e}_\phi T_{\phi rs} - \mathbf{e}_r T_{\phi \phi s}]. \end{aligned} \quad (16)$$

It is easy to verify from Eqs. (11), (13), and (14) that $\nabla \cdot \nabla \times \mathbf{A} \equiv 0$ for these finite operators. This is a direct result of the use of consistent integral relations to obtain the finite approximations.

4. THE MHD EQUATIONS: PLACEMENT OF THE VARIABLES ON THE MESH

In this work we solve the equations of resistive magnetohydrodynamics (MHD). In a convenient nondimensional form, they are

$$\frac{\partial \mathbf{A}}{\partial t} = -\mathbf{E} \quad (17)$$

$$\mathbf{E} = -\mathbf{v} \times \mathbf{B} + \eta \mathbf{J}/S \quad (18)$$

$$\mathbf{B} = \nabla \times \mathbf{A} \quad (19)$$

$$\mathbf{J} = \nabla \times \mathbf{B} \quad (20)$$

$$\frac{\partial \rho \mathbf{v}}{\partial t} = -\nabla \cdot \mathbf{T} \quad (21)$$

$$\mathbf{T} = \rho \mathbf{v} \mathbf{v} - \mathbf{B} \mathbf{B} + \frac{1}{2} (p + B^2) \mathbf{I} \quad (22)$$

$$\frac{\partial \rho}{\partial t} = -\nabla \cdot (\rho \mathbf{v}) \quad (23)$$

$$\frac{\partial u}{\partial t} = -\nabla \cdot \mathbf{F} \quad (24)$$

$$u = \rho v^2 + B^2 + \frac{p}{\gamma - 1} \quad (25)$$

$$\mathbf{F} = \left(\rho v^2 + \frac{\gamma}{\gamma - 1} p \right) \mathbf{v} + 2 \mathbf{E} \times \mathbf{B}, \quad (26)$$

where S is the Lundquist number, η is the resistivity, γ is the ratio of specific heats, u is the total energy density, \mathbf{F} is the energy flux, \mathbf{I} is the unit tensor, and \mathbf{T} is the Reynolds–Maxwell stress tensor. All other quantities have their usual meanings. Note that we have chosen the conservation form of the equations. We have found this form satisfactory, even for plasmas where the magnetic energy dominates the internal energy.

Equation (22) is often modified by the addition of an artificial viscosity of the form $\nu \nabla \rho \mathbf{v}$, which leads to a vector Laplacian operator on the right-hand side of Eq. (21). This term

is necessary to avoid the inevitable buildup of energy at the shortest available wavelength ($\lambda \sim \delta_s = \sqrt{\Delta a_s}$) due to nonlinear mode coupling. We have found it necessary to choose the viscosity component ν such that the cell Reynolds number $R_\Delta = \nu \delta_s / \nu$ is of order unity.

4.1. Hydrodynamic Variables

The boundary of the poloidal computational region is formed by triangle edges. We define the momentum density $\rho \mathbf{v}$, the energy u and the mass density ρ at the triangle centroids \mathbf{r}_s . These quantities thus represent the momentum, energy, and mass per unit volume in a triangular cell. (The quantities $\rho_s \Delta V_s$, $(\rho \mathbf{v})_s \Delta V_s$, and $u_s \Delta V_s$ are the total mass, momentum, and energy in cell s .) Velocities in a cell are given by $\mathbf{v}_s = (\rho \mathbf{v})_s / \rho_s$. The rate of change of these quantities given by applying the differential approximations defined in Section 3.2 to Eqs. (17)–(26). For example, the rate of change of mass density in triangle s is given by

$$\frac{\partial \rho_s}{\partial t} = -\frac{1}{r_s \Delta a_s} \sum_{e=1}^3 r_e \Delta l_e \mathbf{n}_e \cdot \mathbf{F}_e + \frac{in}{r_s} F_{\phi s}, \quad (27)$$

where

$$\mathbf{n}_e \cdot \mathbf{F}_e = \rho_e v_{ne} \quad (28)$$

is the poloidal mass flux across edge e , and

$$F_{\phi s} = \rho_s v_{\phi s} \quad (29)$$

is the mass flux in the toroidal direction. The quantity v_{ne} is the normal component of velocity at edge e and is defined as

$$v_{ne} = \frac{1}{2} \mathbf{n}_e \cdot (\mathbf{v}_{Le} + \mathbf{v}_{Re}). \quad (30)$$

Expressions similar to Eqs. (27)–(29) hold for the momentum equation (Eq. (21)), and the energy equation (Eq. (24)).

The advective flux at an edge e is computed using the full donor cell method. For example, the right-hand side of Eq. (28) is evaluated as

$$(F_{ne})_{adv} = \rho_{Le} v_{ne}, \quad \text{if } v_{ne} > 0, \quad (31a)$$

$$(F_{ne})_{adv} = \rho_{Re} v_{ne}, \quad \text{if } v_{ne} < 0, \quad (31b)$$

where L_e and R_e are the indices of the triangles to the left and right of edge e , respectively. This method introduces numerical diffusion of order $v_{ne} \delta_s / 2$, where $\delta_s \approx \sqrt{\Delta a_s}$. While this technique may be too diffusive for highly accurate shock calculations, it is quite adequate to describe the relatively slow motions of interest in tokamak dynamics. Problems involving strong shocks may require a higher order treatment.

4.2. Electromagnetic Variables

The primary electromagnetic variable in this formulation is the vector potential \mathbf{A} . We define A_r and A_z at the triangles edges e , and A_ϕ at the triangle centroids s . Then Eqs. (13) and (14) define B_{ne} , the component of \mathbf{B} in the poloidal plane normal to a triangle edge, and $B_{\phi s}$, the toroidal component of \mathbf{B} at the triangle centroid. (Note that $(\nabla \cdot \mathbf{B})_s \equiv 0$.)

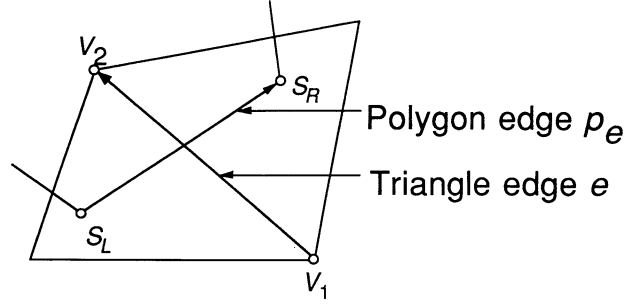


FIG. 8. Triangle and polygon edges.

The procedure described above defines only the component of \mathbf{B} normal to each triangle edge. To uniquely determine the magnetic field we must also define another independent component of \mathbf{B} in the poloidal plane. This is done by integrating Eq. (12) over the surface of the dual polygon p_e that crosses an edge e , as shown in Fig. 8. The polygon edge has a unit normal vector \mathbf{n}_{pe} and a unit tangent vector \mathbf{t}_{pe} . This defines B_{npe} , the components of \mathbf{B} normal to the polygon edge. The cylindrical components of the poloidal field at a triangle edge are then given by

$$B_{re} = \frac{1}{\Delta} (B_{ne} n_{pez} - B_{npe} n_{ez}) \quad (33)$$

$$B_{ze} = \frac{1}{\Delta} (B_{npe} n_{er} - B_{ne} n_{per}), \quad (34)$$

where

$$\Delta = \mathbf{e}_\phi \cdot (\mathbf{n}_e \times \mathbf{n}_{pe}) \neq 0, \quad (35)$$

from which the tangential component of \mathbf{B} at edge e is computed as

$$B_{te} = B_{ze} n_{er} - B_{re} n_{ez}. \quad (36)$$

Similar relationships hold for the current density \mathbf{J} . (Note that if the mesh consists of Delaunay triangles and Voronoi polygons the dual meshes are orthogonal and this calculation is simplified.)

In light of Eq. (17), we define the electric field \mathbf{E} at the same spatial locations as the vector potential \mathbf{A} . The normal and tangential components of the electric field at a triangle edge are given by

$$E_{ne} = -\bar{v}_{\phi e} B_{te} + \bar{v}_{ne} \bar{B}_{te} + \eta J_{ne}/S, \quad (37)$$

$$E_{te} = -\bar{v}_{ne} \bar{B}_{\phi e} + \bar{v}_{\phi e} B_{ne} + \eta J_{te}/S. \quad (38)$$

The toroidal electric field at the triangle centroids is given by

$$E_{\phi s} = -v_{zs} \bar{B}_{rs} + v_{rs} \bar{B}_{zs} + \eta J_{\phi s}/S. \quad (39)$$

We note that Eqs. (11) and (16) are the discrete equivalent of Gauss' theorem, and Eqs. (13) and (14) are the discrete equivalent of Stokes' theorem. Thus, all conservation laws obeyed by the resistive MHD equations have equivalent discrete statements. For example, the rate of change of toroidal flux through the surface of any triangle is given by the line integral of the tangential electric field around the edges of the triangle, in exact equivalence to Lenz's law. This is a direct result of Eqs. (17) and (19) and the definition of the differential operators given here. It is independent of the form of Ohm's law. If the surface is constructed from several triangles, the line integrals over the interior edges cancel, and only the line integral of the tangential electric field around the bounding surface remains. If that surface is a perfect electrical conductor, the tangential electric field vanishes on the boundary and the total toroidal flux is conserved, even in a resistive plasma.

4.3. Averages and Interpolation

In Eqs. (37)–(39), an overscore indicates that an average should be taken or that interpolation be performed. Several types of interpolation are required in the present algorithm, especially during mesh refinement and coarsening. These are discussed in this section.

Interpolation from triangle centroids to edges is a simple average between adjacent triangles:

$$\bar{f}_e = \frac{1}{2}(f_{Re} + f_{Le}). \quad (40)$$

Interpolation from vertices or edges to triangle centroids is also a simple average. For functions defined on vertices,

$$\bar{f}_s = \frac{1}{3}(f_{v1} + f_{v2} + f_{v3}), \quad (41)$$

and for functions defined at edges,

$$\bar{f}_s = \frac{1}{3}(f_{e1} + f_{e2} + f_{e3}), \quad (42)$$

where $v1, v2, v3$, and $e1, e2, e3$ are the three vertices and edges of triangle s , respectively.

Interpolation from edges to vertices is given by

$$\bar{f}_v = \frac{1}{N_{ve}} \sum_{e'} f_{e'}, \quad (43a)$$

where N_{ve} is the number of edges meeting at vertex v , and e' indicates a sum over those edges, while the interpolation formula from vertices to edges is

$$\bar{f}_e = \frac{1}{2}(f_{v1} + f_{v2}), \quad (43b)$$

where $v1$ and $v2$ are the two vertices joined by edge e .

For interpolation from triangle centroids to vertices, we use a pseudo-Laplacian weighted average [22]. In this approach, the interpolated value of a function at vertex v is given by the weighted average

$$\bar{f}_v = \frac{\sum_{s'} (1 + w_{s'}) f_{s'}}{\sum_{s'} (1 + w_{s'})}, \quad (44)$$

where the prime (s') indicates that the sums are taken over all triangles sharing vertex v , and *not* over all triangles N_s .

The weights w_s are determined by requiring that they be as small as possible and that the interpolation be exact for linear functions. We then minimize the functional

$$F(w_s) = \sum_{s'} w_{s'}^2 \quad (45)$$

subject to the constraints

$$L_r = \sum_{s'} (1 + w_{s'}) (r_{s'} - r_v) = 0, \quad (46a)$$

$$L_z = \sum_{s'} (1 + w_{s'}) (z_{s'} - z_v) = 0, \quad (47b)$$

where (r_v, z_v) and (r_s, z_s) are the coordinates of the vertex and the centroids. The result is that

$$w_s = \lambda_r \Delta r_s + \lambda_z \Delta z_s, \quad (48)$$

where $\Delta r_s = r_s - r_v$, $\Delta z_s = z_s - z_v$, and λ_r and λ_z are Lagrange multipliers given by

$$\lambda_r = \frac{R_z I_{rz} - R_r I_{zz}}{I_{rr} I_{zz} - I_{rz}^2}, \quad (49)$$

$$\lambda_z = \frac{R_z I_{rz} - R_z I_{rr}}{I_{rr} I_{zz} - I_{rz}^2}, \quad (50)$$

$$R_r = \sum_{s'} \Delta r_{s'}, \quad (51)$$

$$R_z = \sum_{s'} \Delta z_{s'}, \quad (52)$$

$$I_{rr} = \sum_{s'} (\Delta r_{s'})^2, \quad (53)$$

$$I_{zz} = \sum_{s'} (\Delta z_{s'})^2, \quad (54)$$

$$I_{rz} = \sum_{s'} \Delta r_{s'} \Delta z_{s'}. \quad (55)$$

Equations (40)–(44) have low order of accuracy. The use of higher order interpolation methods, especially in place of Eq. (40), can be shown to lead to a non-Hermitian formulation of sound waves and resulting unphysical behavior.

A complication is that neither Eqs. (40) and (42), Eqs. (41) and (44), nor Eqs. (43a) and (43b) are exact inverses of each other. Thus, for example, interpolation from centroids to vertices using Eq. (44), followed directly by interpolation from vertices to centroids using Eq. (41), introduces errors. Heuristically, these errors do not seem critical to the results obtained with the algorithm, but their affect on problems in parameter regimes other than those studied in the present work cannot be assessed.

4.4. Boundary Conditions

Since the computational boundary consists of triangle edges, the mass density in triangles adjacent to the boundary is completely determined by the normal velocity v_{ne} at the boundary. The momentum density and energy density also require that the normal component of the magnetic field, B_{ne} , and the total pressure, $p + B^2$, be specified. For a nonporous, perfectly conducting wall, the appropriate boundary conditions are that $B_{ne} = v_{ne} = 0$, and that the normal gradient of the total pressure vanish. Implementation of boundary conditions is aided by introducing ghost triangles that lie outside the boundary and are reflections of interior triangles that contain a boundary edge. For the electromagnetic variables it is sufficient to specify the electric field tangent to the boundary. Thus, for a perfectly conducting wall $E_{te} = E_{\phi e} = 0$, where $E_{\phi e}$ is the average of the toroidal electric field in a boundary cell and its reflected ghost cell.

When the inner boundary extends to $r = 0$, regularity conditions must be applied to the complex Fourier coefficients. For scalars (ρv_z , A_z , B_z , J_z , p or u , and ρ), all Fourier components vanish except $n = 0$, which have zero derivative. For vector components (ρv_r , ρv_ϕ , A_r , A_ϕ , B_r , B_ϕ , J_r , and J_ϕ), all Fourier components vanish, except $n = 1$, which have zero derivative. However, for $n = 1$ this condition is only directly applied to the r -component of vectors. The ϕ -component is found from the relation $V_r + iV_\phi = 0$, which assures that the Cartesian (x, y) components of the vector are unique at $r = 0$.

Boundary conditions corresponding to applied tangential or toroidal electric fields and to supersonic inflow (specified upstream velocity, pressure and density) and outflow (zero normal derivative of pressure, density, and velocity) have also been implemented.

5. TIME INTEGRATION

As is appropriate for sound and Alfvén waves the time integration algorithm uses an explicit leapfrog method with predictor–corrector steps to stabilize the nonlinear advective terms. The leapfrog scheme is second-order accurate for uniform time steps, while the predictor–corrector is formally first-order accurate in time. The velocity and momentum are defined at time t^n . The energy density, mass density, and vector potential are defined at time $t^{n+1/2}$. The time step can be arbitrarily large; the semi-implicit method [13–16] is used to remove the CFL time-step restriction and is second-order accurate for uniform time steps. Artificial viscosity, which is required for nonlinear numerical stability, is treated fully implicitly and is, therefore, first-order accurate.

The time advance proceeds by means of operator splitting, i.e.,

$$\left. \frac{\partial \mathbf{U}}{\partial t} \right|_{\text{total}} = \left. \frac{\partial \mathbf{U}}{\partial t} \right|_{\text{explicit}} + \left. \frac{\partial \mathbf{U}}{\partial t} \right|_{\text{semi-implicit}} + \left. \frac{\partial \mathbf{U}}{\partial t} \right|_{\text{viscous}} \quad (56)$$

or

$$\frac{\mathbf{U}^* - \mathbf{U}^n}{\Delta t} = \mathbf{F}_{\text{explicit}} \quad (57a)$$

$$\frac{\mathbf{U}^{**} - \mathbf{U}^*}{\Delta t} = \mathbf{F}_{\text{semi-implicit}} \quad (57b)$$

$$\frac{\mathbf{U}^{n+1} - \mathbf{U}^{**}}{\Delta t} = \mathbf{F}_{\text{viscous}}, \quad (57c)$$

where \mathbf{U} is the state-vector describing the system, and $\mathbf{F}_{\text{explicit}}$, $\mathbf{F}_{\text{semi-implicit}}$, and $\mathbf{F}_{\text{viscous}}$ represent the explicit (wave-like and advective), semi-implicit, and viscous terms that appear on the right-hand side of the equations. Details of these methods are given in the following sections.

5.1. Explicit Advance

Wave-like and advective terms are advanced explicitly with Δt chosen for accuracy and computational convenience rather than numerical stability. The explicit part of the algorithm is

$$\frac{\rho \mathbf{v}^* - \rho \mathbf{v}^{n-1/2}}{\Delta t} = -\nabla \cdot (\rho \mathbf{v} \mathbf{v})^{n-1/2} \quad (58)$$

$$\frac{\rho \mathbf{v}^{n+1/2} - \rho \mathbf{v}^{n-1/2}}{\Delta t} = -\nabla \cdot [(\rho \mathbf{v} \mathbf{v})^* - (\mathbf{B} \mathbf{B})^n] - \frac{1}{2} \nabla (p + B^2)^n \quad (59)$$

$$\mathbf{J}^n = \nabla \times \mathbf{B}^n \quad (60)$$

$$\frac{\mathbf{A}^* - \mathbf{A}^n}{\Delta t} = \mathbf{v}^{n+1/2} \times \mathbf{B}^n \quad (61)$$

$$\mathbf{B}^* = \nabla \times \mathbf{A}^* \quad (62)$$

$$\frac{\mathbf{A}^{n+1} - \mathbf{A}^n}{\Delta t} = \mathbf{v}^{n+1/2} \times \mathbf{B}^* - \eta \mathbf{J}^n / S \quad (63)$$

$$\frac{\rho^* - \rho^n}{\Delta t} = -\nabla \cdot (\rho^n \mathbf{v}^{n+1/2}) \quad (64)$$

$$\frac{\rho^{n+1} - \rho^n}{\Delta t} = -\nabla \cdot (\rho^* \mathbf{v}^{n+1/2}) \quad (65)$$

$$\frac{u^* - u^n}{\Delta t} = -\nabla \cdot \frac{\gamma}{\gamma - 1} p^n \mathbf{v}^{n+1/2} \quad (66)$$

$$p^* = (\gamma - 1)[u^* - (\rho v^2)^{n+1/2} - (B^2)^{n+1}] \quad (67)$$

$$\mathbf{E}^{n+1} = -\mathbf{v}^{n+1/2} \times \mathbf{B}^{n+1} + \eta \mathbf{J}^{n+1} / S \quad (68)$$

$$\frac{u^{n+1} - u^n}{\Delta t} = -\nabla \cdot \left\{ \left[(\rho v^2)^{n+1/2} + \frac{\gamma}{\gamma - 1} p^* \right] \mathbf{v}^{n+1/2} + 2 \mathbf{E}^{n+1} \times \mathbf{B}^{n+1} \right\} \quad (69)$$

$$p^{n+1} = (\gamma - 1)[u^{n+1} - (\rho v^2)^{n+1/2} - (B^2)^{n+1}]. \quad (70)$$

Total mass, momentum, and magnetic flux are exactly conserved. Because the pressure, magnetic field, mass density, and momentum are defined at different time levels, the sum of the kinetic, magnetic, and internal energies is exactly conserved in the limit $\Delta t \rightarrow 0$, independently of spatial discretization. (The volume integral of the quantity u is exactly conserved independently of Δt .) The predictor–corrector steps introduce an additional diffusion of order $v \Delta t / 2$ that can exceed the diffusion from the donor cell fluxes when the time step exceeds the explicit CFL stability limit.

5.2. Semi-Implicit and Implicit Solutions

We use the semi-implicit method [13–16] to remove the CFL time step restriction for numerical stability associated with the explicit advance described in Section 5.1. This restriction is of the form $C \Delta t / \delta < 1$, where $C = \sqrt{V^2 + C_s^2 + V_A^2}$ is the characteristic speed for the propagation of disturbances, and δ is a measure of the linear size of a zone (here proportional to the square root of the triangle area). With the use of the semi-implicit method the algorithm becomes numerically stable at arbitrary Δt so that the time step can be chosen for reasons of accuracy or computational convenience rather than numerical stability. The time step remains limited by the advective CFL stability condition $V \Delta t / \delta < 1$, where V is the local flow speed. This is not a significant restriction when $V / \sqrt{C_s^2 + V_A^2} \ll 1$, as is the case for many fusion applications. When $V / \sqrt{C_s^2 + V_A^2} \approx 1$, as is the case for shocks, the algorithm becomes explicit. This restriction can thus be viewed as an accuracy condition.

In this work we use a simple vector Laplacian semi-implicit operator [16]. This term is added to and subtracted from the right-hand side of the momentum equation at the new and old time levels. The semi-implicit advance is

$$(1 - \alpha \Delta t \nabla^2)(\rho \mathbf{v})^{**} = (\rho \mathbf{v})^* - \alpha \Delta t \nabla^2(\rho \mathbf{v})^n, \quad (71)$$

where α is the semi-implicit coefficient given by

$$\alpha = \frac{\sigma}{k_{\max}^2 \Delta t} \left[\left(\frac{\Delta t}{\Delta t_{\text{CFL}}} \right)^2 - 1 \right] \quad \text{for } \Delta t > \Delta t_{\text{CFL}}, \quad (72)$$

$$\alpha = 0 \quad \text{for } \Delta t \leq \Delta t_{\text{CFL}}, \quad (73)$$

where $(\rho \mathbf{v})^*$ is the value of momentum obtained from the explicit advance (Eq. (59)), $k_{\max} \approx 1/\delta_s$ is the largest wave-number resolved on the mesh, Δt_{CFL} is the maximum time step allowed by the CFL restriction for normal modes, and σ is a constant $\gtrsim 1$. Since Eq. (71) is second order in space, boundary conditions must be applied to the tangential (ϕ and z) components of the momentum density. For inviscid flow, the normal derivative is set to zero at solid boundaries; for viscous flow, the tangential momentum is set to zero. In either case, the normal component vanishes at solid boundaries. For supersonic inflow, the upstream velocity is specified. For outflow, the normal derivatives of all components are set to zero. Boundary conditions at $r = 0$ are as described in Section 4.4.

The time step is completed with the implicit viscous advance

$$(1 - \nu \Delta t \nabla^2)(\rho \mathbf{v})^{n+1} = (\rho \mathbf{v})^{**}, \quad (74)$$

where ν is a (possibly spatially dependent) artificial viscosity coefficient. All components of momentum are set to zero at solid boundaries. For inflow, outflow, and $r = 0$, the boundary conditions are as described for Eq. (71).

The vector Laplacian operator appearing in Eqs. (71) and (74) requires the definition of the scalar Laplacian. This is accomplished by the successive application of the gradient and divergence operators defined in Eqs. (9) and (11). When combined with the condition

$$(\nabla f)_G = (\nabla f)_B, \quad (75)$$

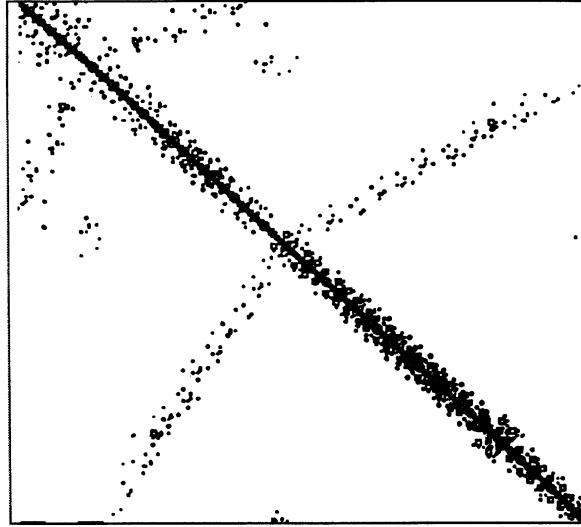


FIG. 9. Matrix structure for the Laplacian operator on an unstructured mesh.

where the subscripts G and B represent values in ghost and boundary triangles, respectively, the resulting operator is self-adjoint.

Since the mesh is unstructured, the $N_s \times N_s$ matrices corresponding to the operators appearing in Eqs. (71) and (74) are not banded but are sparse. An example of the structure pattern for a case with 320 triangles is shown in Fig. 9. Matrix inversion is performed with a conjugate gradient (CG) algorithm with diagonal preconditioning [23]. Since this method is iterative, the full $N_s \times N_s$ matrix never needs to be stored. Good convergence properties have been found, even with relatively large time steps.

At this time the resistivity is treated explicitly. Since $\eta/S \ll 1$ we have not found this to be computationally restrictive.

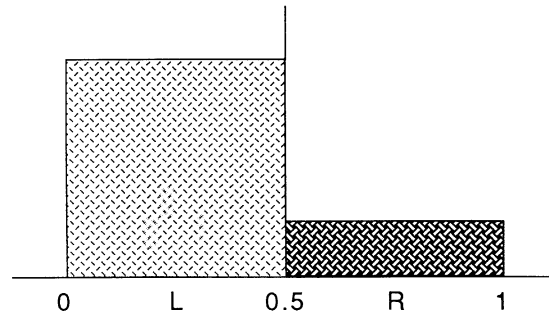
6. APPLICATIONS

The algorithm described above has been applied to several nonlinear test problems, both two- and three-dimensional. The code based on the algorithm is called TRIM, for TRIangular MHD. The application of TRIM to these test problems is described in the following sections.

6.1. The Hydrodynamic Shock Tube Problem

A standard problem for testing hydrodynamic algorithms has been defined by Sod [24]. The initial conditions consist of two fluids with different uniform properties separated by a membrane. The fluid to the left of the membrane has both pressure p_L and density ρ_L equal to 1. The fluid to the right of the membrane has $p_R = 0.1$ and $\rho_R = 0.125$. The initial velocity is zero and the ratio of specific heats is $\gamma = 1.4$ (air). The magnetic field is zero. These conditions are sketched in Fig. 10.

At $t=0$ the membrane is ruptured and the fluid reacts dynamically. This Riemann problem is one of the few fully nonlinear problems that has a known analytic solution [9], and is therefore valuable for testing numerical algorithms. The solution consists of an



$$\begin{array}{ll} \rho_L = 1 & p_R = 0.1 \\ \rho_L = 1 & \rho_R = 0.125 \end{array}$$

FIG. 10. Initial conditions for hydrodynamic shock tube problem.

expansion wave traveling to the left and a shock wave and a contact discontinuity traveling to the right, all with known velocities.

We have applied the TRIM algorithm to this problem. The time integration is explicit and the artificial viscosity ν is set to zero. While this test problem is one-dimensional, the triangular grid in TRIM requires that a two-dimensional problem be solved. The mesh is shown in Fig. 11. It contains 1250 triangles. In this figure, the initial membrane is horizontal and centered at $z = 0.5$. As the solution proceeds in time no spatial variation develops in the direction parallel to the membrane. The solution thus remains one-dimensional, even with the two-dimensional algorithm. The analytic solution at $t = 0.1$ is shown in Figs. 12a–c.

The results of TRIM with the mesh shown in Fig. 11 is shown in Figs. 13a–c at $t = 0.1$. The magnitude of the pressure and velocity in the region between the shock and

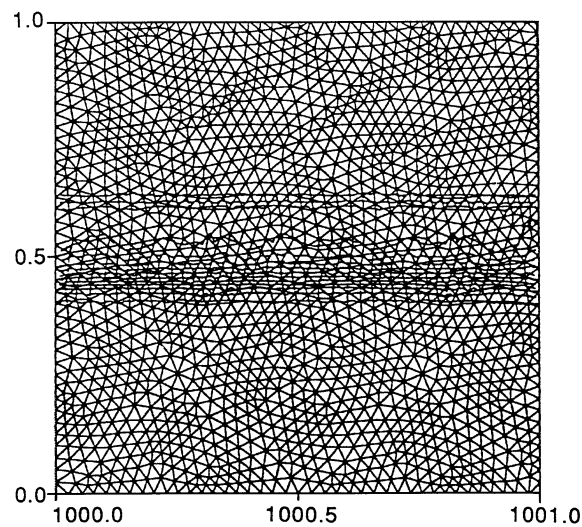


FIG. 11. Mesh for hydrodynamic shock tube problem, with superimposed contours.

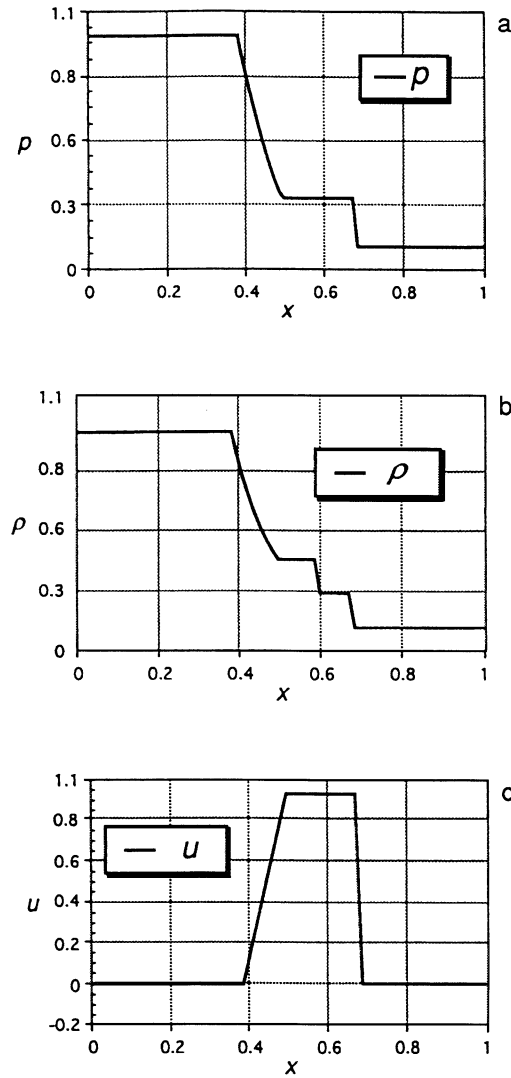


FIG. 12. (a-c) Analytic solution to the hydrodynamic shock problem.

the expansion fan are quite accurate. (Note the because of the normalization the pressure in TRIM appears to be twice the pressure in the analytic solution.) As is anticipated, the numerical diffusion introduced by the first-order upwind treatment of the interface fluxes has resulted in a considerable smoothing of the discontinuities. This is especially noticeable in the density. The contact discontinuity, which is an interface separating regions of different density but equal pressure and velocity, has been considerably smeared out. This structure is particularly difficult to treat numerically. In contrast with a shock, there are no nonlinear processes that continue to generate a contact discontinuity in opposition to numerical diffusion; it is merely an interface between two states of different density. The effect of any diffusion in the algorithm is felt most strongly here.

One solution to the problem of numerical diffusion is to employ a higher order approximation to the interface fluxes. Another solution is to use a low order method but to reduce the diffusion by adaptively refining the mesh in the regions near the discontinuities. We

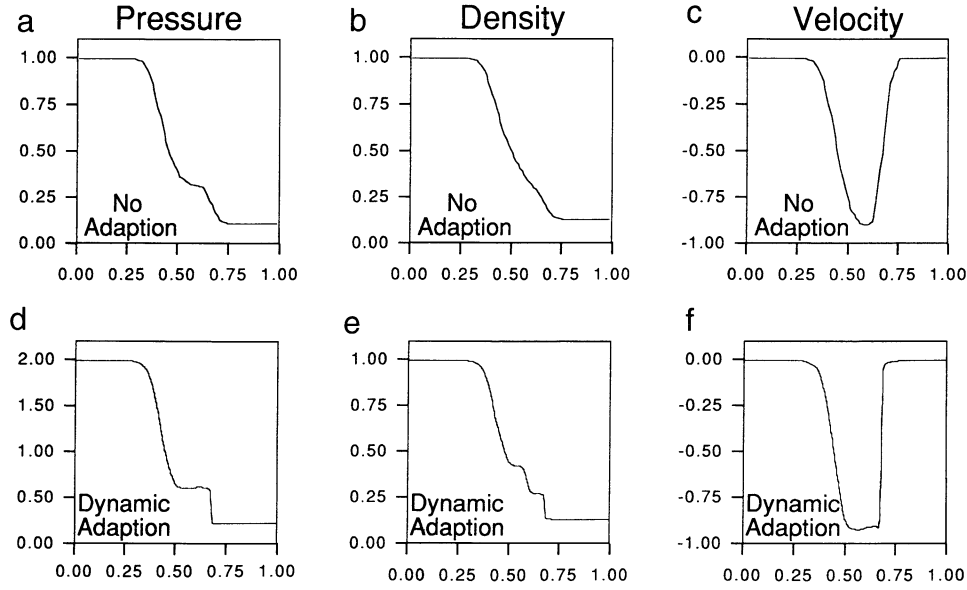


FIG. 13. (a–f) Comparison of numerical solutions without (a–c) and with (d–f) dynamic mesh adaption.

have applied the mesh refinement techniques described in Section 2.7 to this problem. For this problem we used the mass density ρ as the dependent variable in the refinement criterion, Eq. (2a), with $\varepsilon = 0.2$, $E_R = 0.8$, and $E_C = 0.2$. (Smaller values of E_R resulted in an unacceptable number of triangles; larger values resulted in patchy refinement. See Section 2.6.) Both refinement and coarsening were done every 50 timesteps. The initial mesh is shown in Fig. 14a. This mesh has been refined in order to initially capture the pressure and density discontinuities. The adaptively refined mesh at $t = 0.1$ is shown in Fig. 14b. The algorithm has adapted the mesh to the dynamically evolving shock, contact discontinuity, and expansion front. The initial mesh had 7777 triangles, and the dynamically evolving mesh contained up to 34,415 triangles.

In Figs. 13a–f we compare the solution at $t = 0.1$, with and without adaption. All features are sharper with dynamic mesh refinement than without. In both cases, the jump conditions are exact. The discontinuities become sharper as the grid is refined. However, we are unable to furnish an estimate of the error as a function of grid refinement, as this is the only satisfactory grid we could produce. As anticipated, the major error is in the contact discontinuity. This error can only be eliminated by the use of a higher order method, such as a Riemann solver. This is beyond the scope of the present work. We emphasize that problems involving strong shocks are uncommon in fusion plasmas, so that low-order methods are sufficient for these applications.

6.2. The Magnetohydrodynamic Shock Tube Problem

The hydrodynamic shock tube solution described in the previous section has been extended to MHD by Brio and Wu [25]. The thermodynamic properties of the left and right states are the same in the purely hydrodynamic case. A uniform magnetic field B_x is imposed in the direction (x) perpendicular to the membrane. The component of the magnetic field B_y parallel to the membrane is discontinuous at the membrane, with $B_{yL} = 1$ and $B_{yR} = -1$.

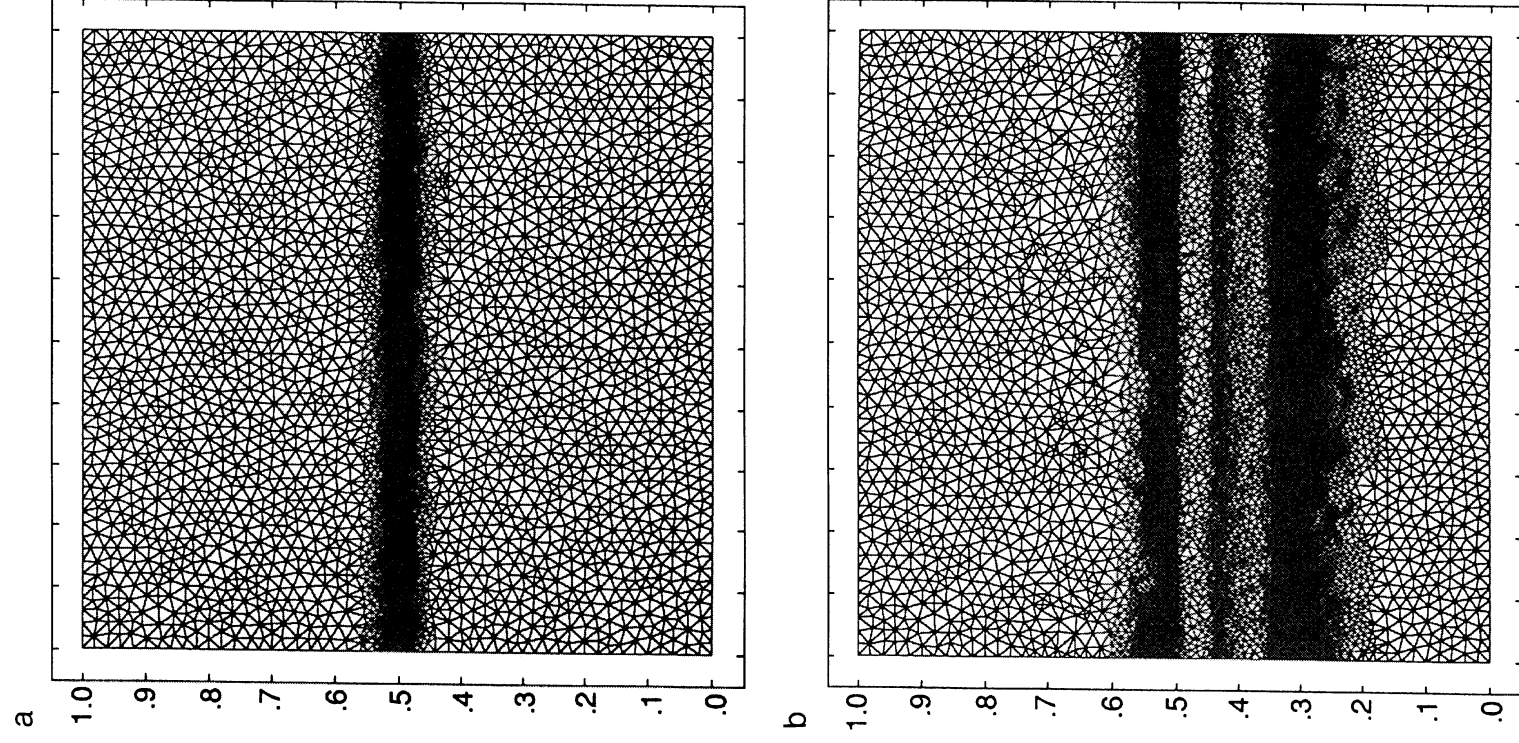


FIG. 14. (a) Initial mesh for dynamic adaption; (b) dynamically adapted mesh at $t = 0.1$.

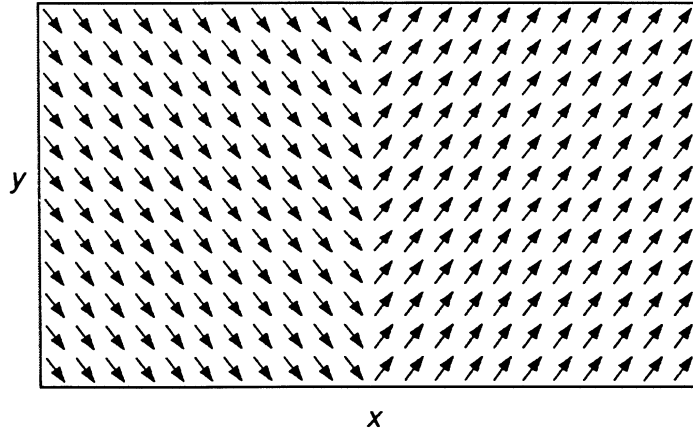


FIG. 15. Initial magnetic field vectors for the MHD shock tube problem.

The membrane is thus a current sheet in the z -direction. The magnetic configuration is sketched in Fig. 15.

The dynamics after the membrane is ruptured are much more complex than in the purely hydrodynamic case; we refer the reader to Ref. [25] for details. In Fig. 16 we present our two-dimensional solution of this problem. This can be compared with the more finely resolved one-dimensional solution of Brio and Wu [25]. We find that most of the details of the Brio–Wu solution are reproduced in our results, although the effect of the low-order diffusion is again apparent, especially near the contact discontinuity. We have also repeated the calculation with the component of magnetic field parallel to the membrane rotated by $\pi/2$ and find identical results for this polarization.

We have also applied mesh refinement and coarsening to the MHD shock tube problem. The refinement and coarsening criteria are the same as described in Section 6.1. Figure 17 shows a comparison of the mass density ρ with and without dynamic mesh adaption. Finer structure is observed when dynamic mesh refinement is implemented. However, the contact discontinuity is still poorly resolved due to the low order calculation of the interface fluxes.

6.3. Supersonic Flow Past a Sphere

We now consider the case of steady axisymmetric supersonic flow past a solid sphere. The sphere is centered at $r = z = 0$. The boundary of the sphere is at $r^2 + z^2 = 1$. The outer boundary of the computational domain is a cylinder of radius $r = 10$ with ends at $z = \pm 10$. Supersonic inflow conditions are imposed at the upper boundary ($z = 10$) and outflow conditions are imposed at the lower ($z = -10$) and outer ($r = 10$) boundaries. Regularity conditions are imposed at $r = 0$.

The initial conditions consist of uniform pressure, density, and axial velocity (v_z). The initial radial velocity (v_r) is set to zero. The parameters are chosen so that the initial axial velocity corresponds to an upstream Mach number $M = v/c_s = 2$.

With the magnetic field set to zero, the hydrodynamic equations are integrated forward in time until a steady (time independent) state is reached. A small amount of viscosity

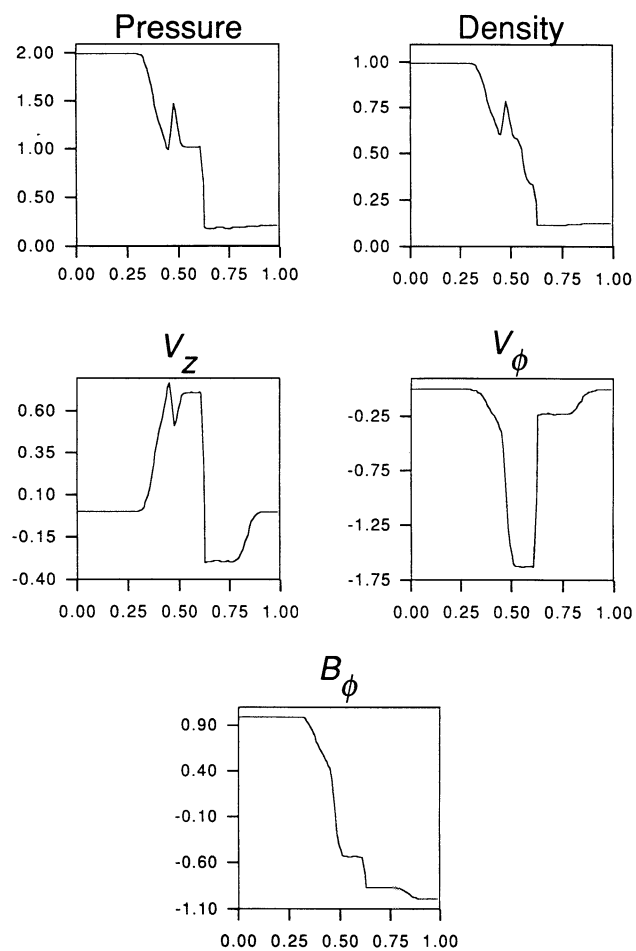


FIG. 16. Numerical solution of the MHD shock tube problem. This can be compared with the solution given in [25].

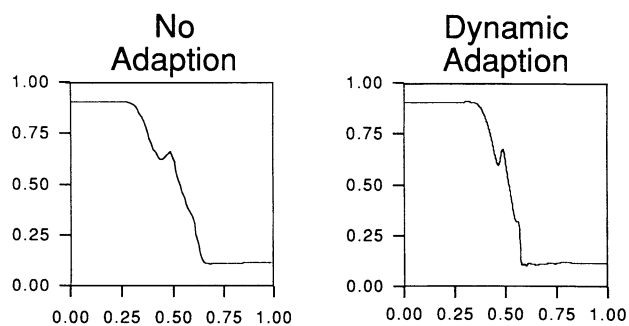


FIG. 17. Comparison of the results for the MHD shock tube problem without and with dynamic mesh adaption.

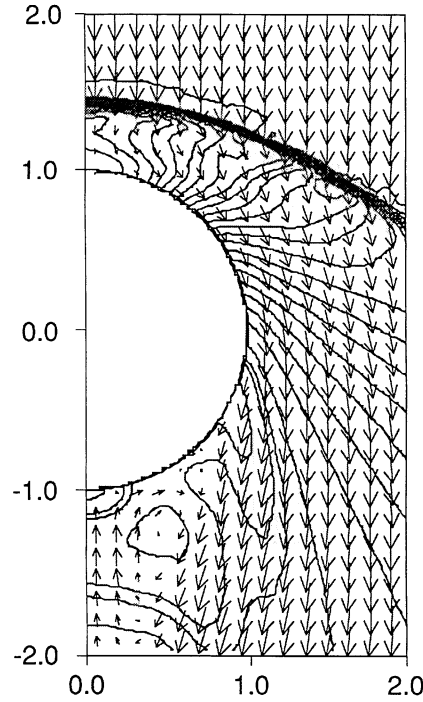


FIG. 18. Velocity vectors and pressure contours for $M = 2$ flow past a sphere.

($\nu = 10^{-3}$) was used in this calculation. In the steady state a shock forms in front of the sphere as the flow is deviated around it. The flow separates from the surface of the sphere and forms a recirculating eddy behind it. The pressure contours and velocity vectors in the vicinity of the sphere are shown in Fig. 18.

This calculation was performed using an adaptive mesh along with the criterion given by Eq. (2b). The mass density was used to compute the normalized gradient. The mesh was locally refined if $E_s > 0.95$, and coarsened if $E_s < 0.05$. Refinement and coarsening were performed every 500 timesteps. The initial and final meshes are shown in Figs. 19a and b. The final mesh has 13,360 triangles.

We have repeated this calculation, but with a dipole magnetic field embedded in the sphere at $t = 0$. The axis of the dipole is aligned with the upstream flow direction. This field is given by the vector potential

$$A_\phi = B_0 \frac{r}{(r^2 + z^2)^{3/2}}, \quad (76)$$

where B_0 is the strength of the magnetic field at $r = 1, z = 0$. The resistivity was taken to be uniform and to correspond to a Lundquist number of $S = 10^3$. A coarse mesh was used. The mesh in the vicinity of the sphere is shown in Fig. 20. The initial magnetic field is shown in Fig. 21.

As the calculation proceeds, the initial dipole field remains embedded in the spherical boundary and is swept downstream behind the sphere. The shock remains in front of the sphere. The final magnetic field for the case $B_0 = 0.5$ is shown Fig. 22, and the adapted grid is shown in Fig. 23.

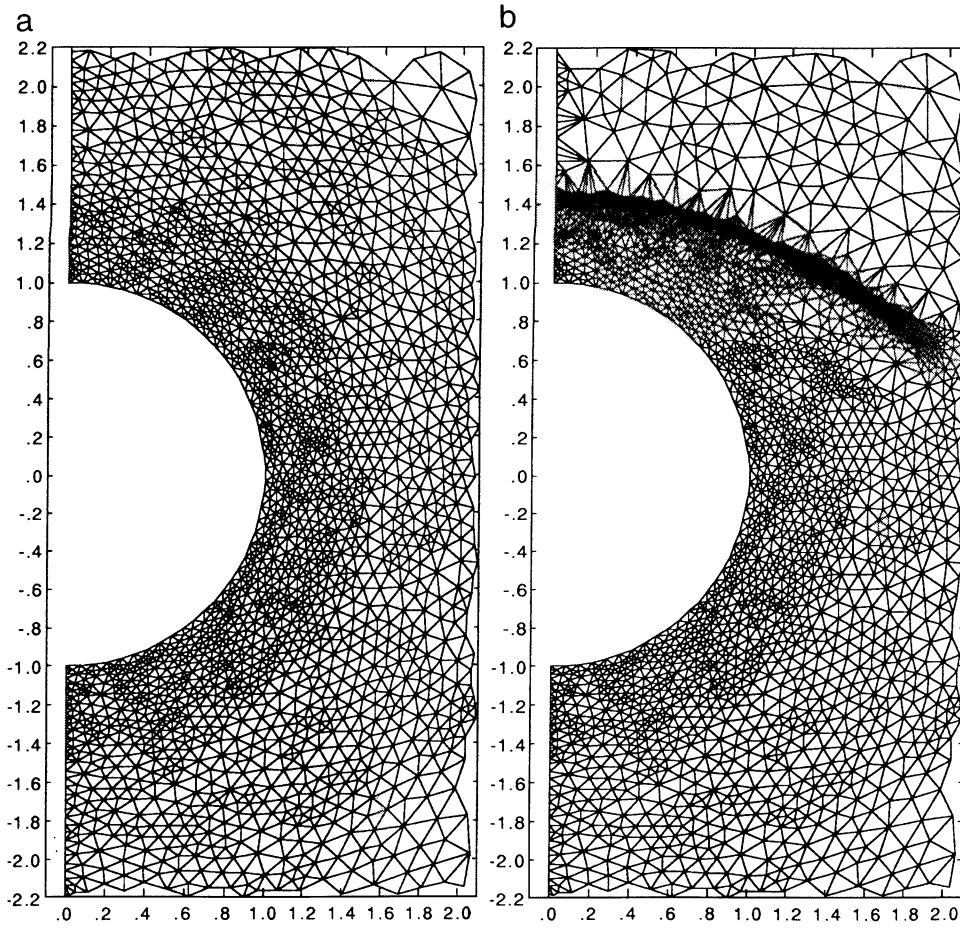


FIG. 19. (a) Initial mesh; (b) final, adapted mesh for $M = 2$ flow past a sphere.

6.4. Nonlinear Evolution of Toroidal Instabilities

One of the standard applications of MHD to fusion plasmas is the linear growth and nonlinear saturation of instabilities. These instabilities can occur because toroidal equilibria are not necessarily minimum energy states, even though they are extrema of the energy. Equilibria that are local maxima of the energy are unstable, with small deviations from the initial state growing exponentially in time. Determining the stability of equilibria is an important problem in the design of a fusion experiment. Even stable equilibria can be driven unstable by diffusive processes [7].

It is to be emphasized that algorithms of the type described in this paper are not the most efficient or accurate way of computing linear stability. Specialized algorithms that find the eigenvalues of the linearized MHD operator are better suited to this problem [26]. Nonetheless, linear stability problems are among the few three-dimensional toroidal problems with known solutions (generally obtained with the specialized algorithms [26]) and are therefore valuable benchmarks for nonlinear, time-dependent algorithms.

Physically, linearly unstable MHD modes are of interest only if they impart some observable, and hence, finite and nonlinear, perturbation to the physical system. The details of

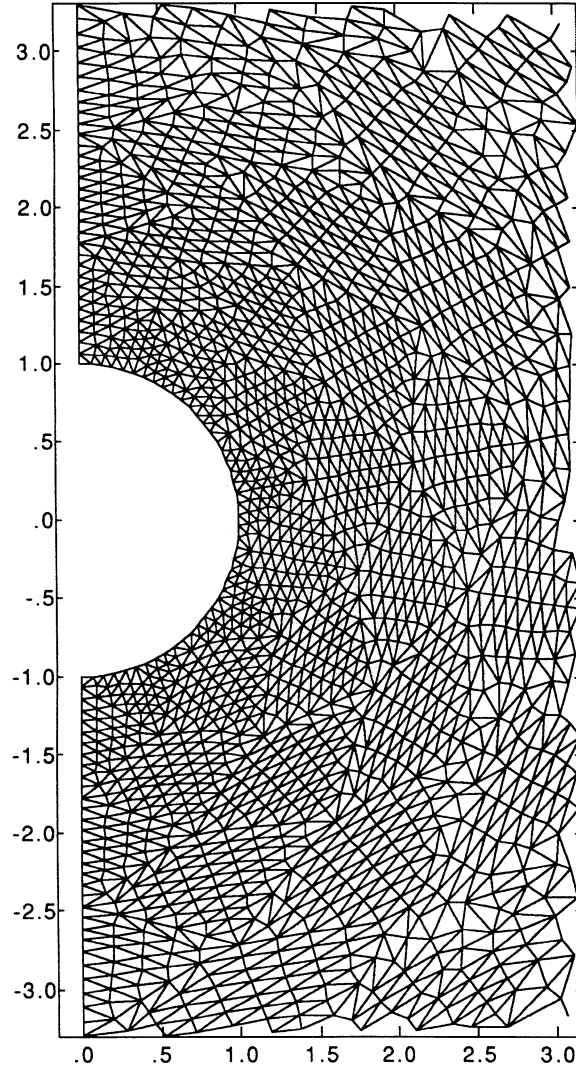


FIG. 20. Mesh used for flow past a sphere with an embedded dipole magnetic field.

the nonlinear evolution of linearly unstable modes requires that algorithms of the present type be employed.

6.4.1. *Solov'ev Equilibrium*

Axially symmetric force balance in a torus is given by solutions to the Grad–Shafranov equation

$$\Delta^* \psi = r^2 \nabla \cdot \frac{\nabla \psi}{r^2} = \frac{1}{2} r^2 \frac{dP}{d\psi} - F \frac{dF}{d\psi}, \quad (77)$$

where $\psi(r, z) = r A_\phi$ is the poloidal flux, and the pressure $P(\psi)$ and the toroidal flux function $F(\psi) = r B_\phi$ are arbitrary functions of ψ . An analytic solution has been given by

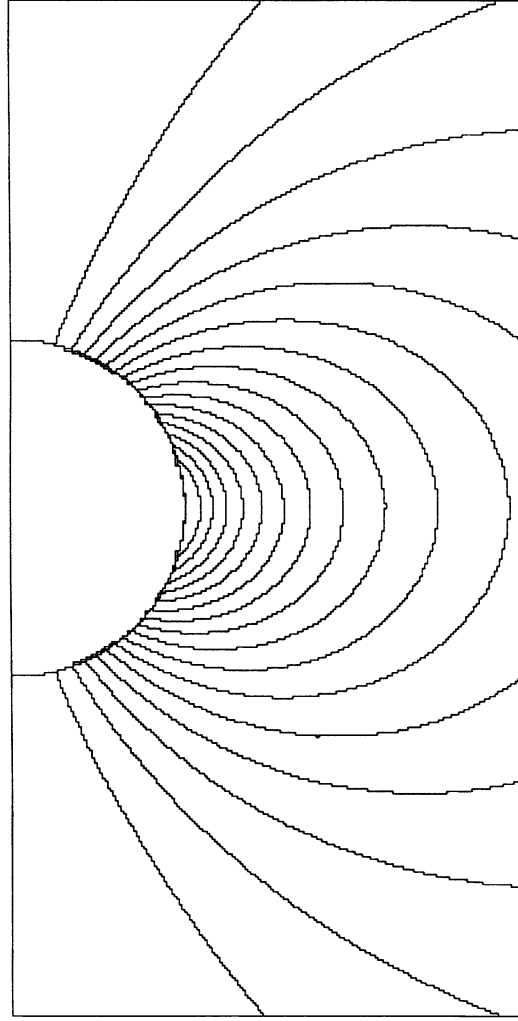


FIG. 21. Initial dipole magnetic field.

Solov'ev [27]. With

$$P(\psi) = -\frac{4}{\varepsilon^2} \frac{1 + \kappa^2}{\kappa^2} (\psi - 1) \quad (78)$$

$$F(\psi) = \frac{2b}{\varepsilon\kappa} (1 - \psi)^{1/2} + C \quad (79)$$

the poloidal flux and toroidal field are

$$\psi(r, z) = \frac{1}{\varepsilon^2} \left[\frac{(r^2 + b^2)z^2}{\kappa^2} + \frac{(r^2 - 1)^2}{4} \right] \quad (80)$$

$$B_\phi = \frac{C}{r} + O(b), \quad (81)$$

where $\varepsilon = a/R$ is the inverse aspect ratio, κ is the elongation, b is a diamagnetic factor, and C is a normalization constant that determines the strength of the vacuum toroidal

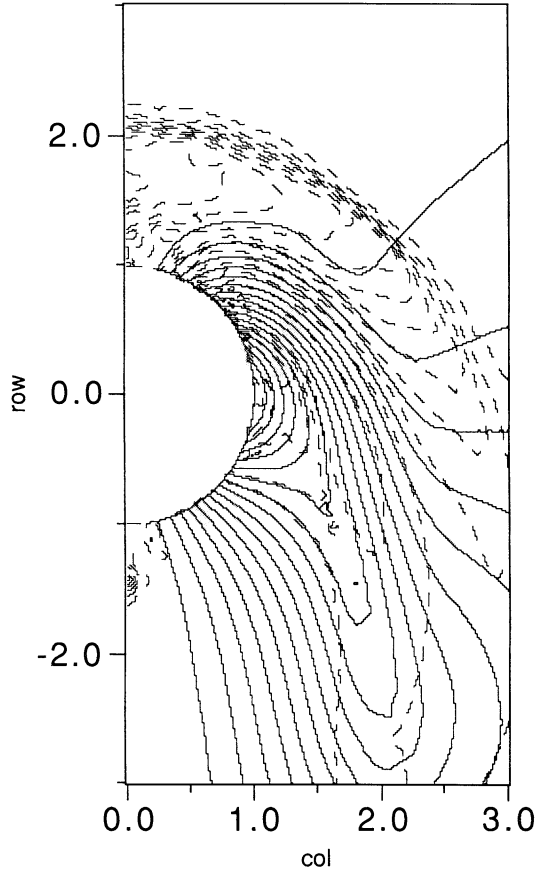


FIG. 22. Final magnetic field configuration for $M = 2$ flow past a sphere with an embedded initial dipole field.

field. Contours of ψ and P with $\kappa = 1$ and $b = 0$ are shown in Fig. 24. Since $b = 0$, this equilibrium has no poloidal current ($J_r = J_z = 0$).

Linear stability and comparison with previous results. The linear stability of the Solov'ev equilibrium to large-scale MHD modes has been extensively studied using specialized eigenvalue techniques [28]. We have developed a "linearized" modification of the TRIM algorithm to study the linear stability of this equilibrium. This modification is possible because of the pseudospectral representation. In these calculations the initial conditions consist of the axisymmetric ($n = 0$) equilibrium, such as Eqs. (80) and (81), along with very low amplitude random noise in the velocity field of a single $n = n_0 > 0$ toroidal mode. All other toroidal modes are set to zero initially. The calculation then proceeds as described in Section 5, except that after each time step the amplitudes of all modes with $n \neq n_0$ are reset to zero and the $n = 0$ (equilibrium) component is restored to its initial value. This effectively disables any nonlinear or quasilinear mode couplings and affords a good approximation to the solution of the linearized equations. The magnetic and kinetic energies of an unstable mode will grow exponentially with time as $\exp(2\gamma t)$, allowing the growth rate (eigenvalue) γ to be calculated. The self-similar spatial structure of the growing mode defines the eigenvector.

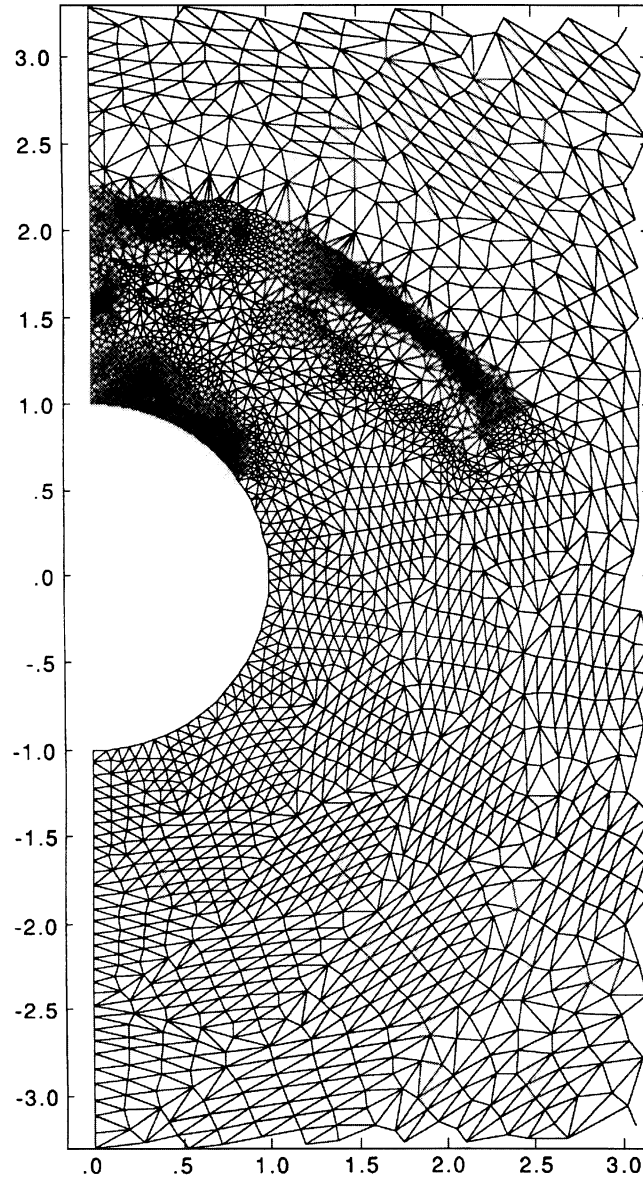


FIG. 23. Adapted grid for flow past a sphere with embedded dipole magnetic field.

The Solov'ev equilibrium can be completely parameterized in terms of the three non-dimensional constants ε (the inverse aspect ratio), κ (the elongation), and q_0 (the safety factor on axis). In Ref. [28] values of normalized growth rate $\gamma\tau_A$ (where τ_A is the Alfvén transit time) were obtained over a range of q_0 for values of $\varepsilon = 1/3$ and $\kappa = 1$ and 2. Here we have primarily focused our attention on the cases with $q_0 = 0.5$, which exhibit robust instability to ideal MHD modes for these values of ε and κ . Special cases with $q_0 = 0$ and $q_0 = 0.8$ will also be described. Also, we have used a boundary condition that corresponds to a perfectly conducting boundary placed at the plasma edge. Thus, only internal (rigid boundary) modes are considered.

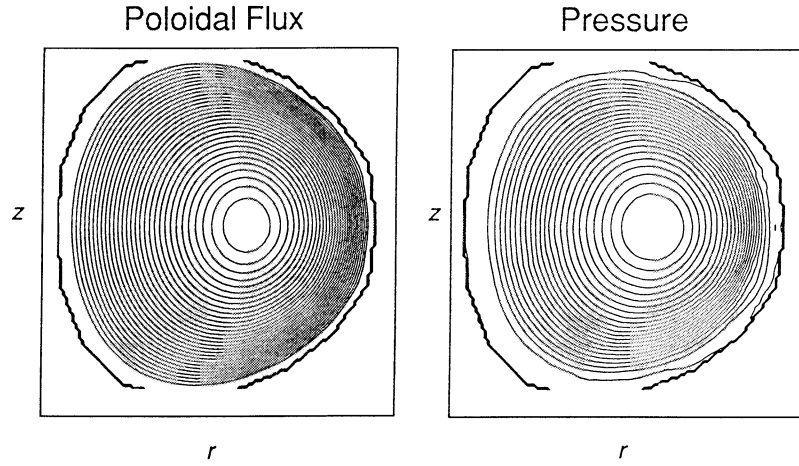


FIG. 24. Contours of poloidal flux and pressure for the Solov'ev toroidal equilibrium with $\kappa = 1$.

When the semi-implicit method is used to take time steps that exceed the CFL limit, the growth rate will be a function of the time step [16]. This is discussed in more detail later in this section. The actual growth rate is obtained in the limit $\Delta t \rightarrow 0$. (In practice, we only take the limit $\Delta t / \Delta t_{\text{CFL}} \rightarrow 1$.) Here we have performed such a convergence study only for the two cases $\varepsilon = 1/3$, $n_0 = 2$, $q_0 = 0.5$, and $\kappa = 1$ and 2. Quantitative comparisons should be made for these cases only.

For the converged cases ($q_0 = 0.5$, $n_0 = 2$), we find for $\kappa = 1$, $\gamma\tau_A = 0.122$, as compared with $\gamma\tau_A = 0.158$ from Ref. [28] (when converted to our normalization); for $\kappa = 2$, we find $\gamma\tau_A = 0.22$, compared with $\gamma\tau_A = 0.28$ from Ref. [28]. The time-step converged growth rates determined from TRIM are about 20% lower than those of Ref. [28] and are consistently lower for the nonconverged cases. A quantitative result for the case with $q_0 = 0$, $\kappa = 1$, is not given in Ref. [28], where this mode is identified as “an $m = 0$ mode and not a kink.”

The eigenfunctions (spatial structure) for the cases $n_0 = 2, 3$, and 4, $q_0 = 0.5$, and $\kappa = 1$ are shown in Figs. 25–27. In each figure, velocity vectors of the real part of the poloidal velocity (v_r, v_z) and contours of the imaginary part of the toroidal velocity (v_ϕ) for mode n_0 are shown. For the $n_0 = 2$ mode, the poloidal structure is dominantly $m = 1$, while for the $n_0 = 4$ mode, the poloidal structure is dominantly $m = 2$. This is consistent with the value $q_0 = 0.5$, and in agreement with the results of Ref. [28]. The eigenfunction for the case $n_0 = 2$, $q_0 = 0$, $\kappa = 1$ is shown in Fig. 28. It is easy to see the dominant $m = 0$ interchange structure of this mode.

The equilibrium for the case $\kappa = 2$, $q_0 = 0.5$ is shown in Fig. 29. Velocity eigenfunctions for the cases $\kappa = 2$, $q_0 = 0.5$, and $n_0 = 2$ and 3 are shown in Figs. 30 and 31. The dominant poloidal mode structure is in agreement with that of Ref. [28]. Finally, in Fig. 32 we display the velocity eigenfunction for the case $\kappa = 2$, $q_0 = 0.8$, $n_0 = 1$. The rigid $m = 1$ displacement of the mode is in contrast with the vortex structure displayed by the other unstable modes found here.

Effect of time step on linear growth rate. As discussed in Section 5, TRIM uses the semi-implicit method [13–16] to achieve time steps in excess of that set by numerical stability constraints. As shown in Ref. [16] the semi-implicit method reduces the characteristic

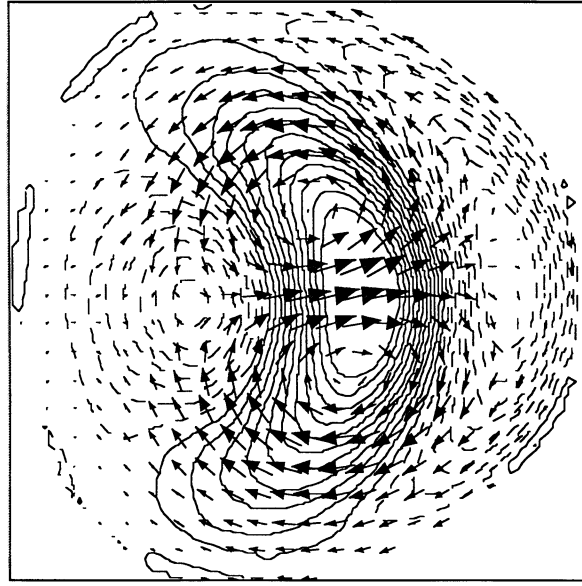


FIG. 25. Linear eigenfunction for the $n = 2$ mode in the Solov'ev equilibrium with $\kappa = 1$, $q_0 = 0.5$, $R/a = 3$. Velocity vectors display the real part of the poloidal velocity (v_r , v_z), contours display the imaginary part of the toroidal velocity (v_θ).

frequency of a mode with wave number k by a factor

$$\frac{\omega}{\omega_0} = \frac{1}{\sqrt{1 + \alpha k^2 \Delta t}}, \quad (82)$$

where α is the semi-implicit coefficient and ω_0 is the frequency obtained by an explicit

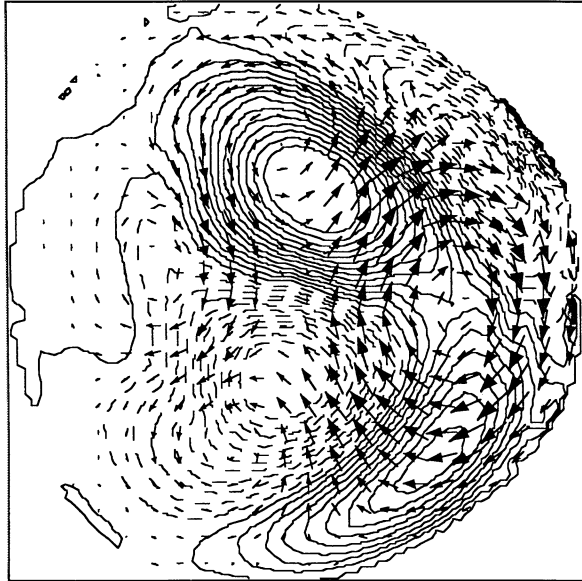


FIG. 26. Linear eigenfunction for the $n = 3$ mode in the Solov'ev equilibrium with $\kappa = 1$, $q_0 = 0.5$, $R/a = 3$.

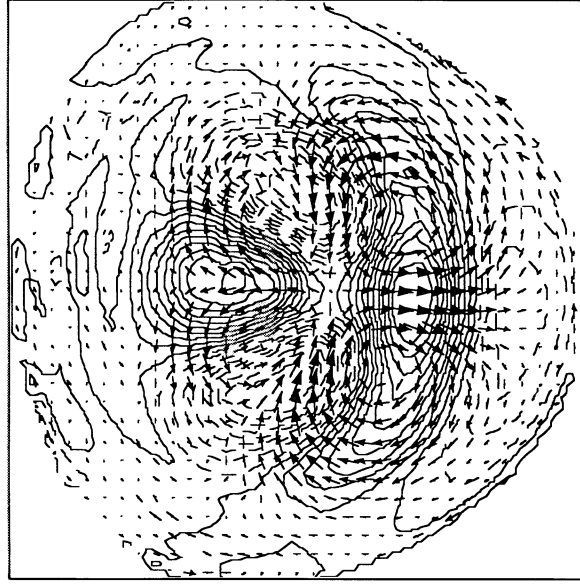


FIG. 27. Linear eigenfunction for the $n=4$ mode in the Solov'ev equilibrium with $\kappa=1$, $q_0=0.5$, $R/a=3$.

calculation with $\Delta t = \Delta t_{\text{CFL}}$. Using Eq. (72), this expression can be rewritten as

$$\frac{\omega}{\omega_0} = 1 / \sqrt{1 + \sigma \left[\left(\frac{\Delta t}{\Delta t_{\text{CFL}}} \right)^2 - 1 \right] \left(\frac{k}{k_{\text{max}}} \right)^2}, \quad (83)$$

where σ is a constant of order unity and k_{max} is the maximum value of k that can be resolved on the grid. For unstable modes, the frequency ω becomes the growth rate γ .

For the case $n_0=2$, $\kappa=1$, and $q_0=0.5$ (see Fig. 25), we have $k_{\text{max}} = 164$ (corresponding to 2090 triangles), $k \approx 15$ (corresponding to $\lambda_r \approx \lambda_z \approx 2a \approx 0.6$), and $\sigma = 1.5$. This case was run with a small amount of artificial viscosity, $\nu = 10^{-4}$. In Fig. 33 we plot the ratio γ/γ_0 obtained from both TRIM and from Eq. (83) as a function of $\Delta t/\Delta t_{\text{CFL}}$ for this case. These results substantially confirm the effect of the semi-implicit method on the growth rate. The discrepancy between the two curves may be due to the artificial viscosity or other numerical damping inherent in the algorithm.

Nonlinear results. The linear results described above were obtained by removing all nonlinear interactions, freezing the $n=0$ component of the solution, and allowing only a single mode with $n=n_0$ to evolve. To obtain the full nonlinear dynamical evolution of the unstable equilibrium, all modes with $n>0$ are initially perturbed, all nonlinear interactions are restored, and the $n=0$ component is allowed to evolve under the influence of unbalanced forces, resistivity, viscosity, and nonlinear effects. Since these cases may involve large amplitude displacements and considerable dynamics, larger values of resistivity and artificial viscosity are used than in the strictly linear results. Typical values are $S=10^4$ and $\nu=10^{-2}$. Total toroidal flux is conserved.

In Fig. 34 we plot the time evolution of the kinetic energy in the modes $1 \leq n \leq 5$ (corresponding to 16 toroidal mesh points) for the case $\kappa=1$, $q_0=0.5$, $R/a=3$. The time step

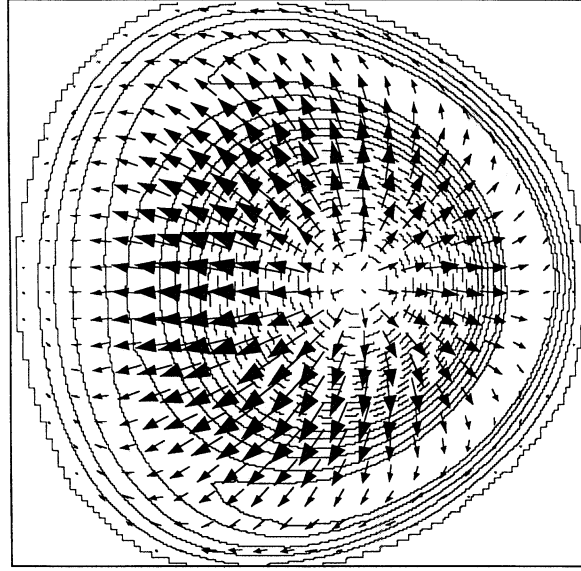


FIG. 28. Linear eigenfunction for the $n = 2$ mode in the Solov'ev equilibrium with $\kappa = 1$, $q_0 = 0$, $R/a = 3$. Note the $m = 0$ interchange structure.

is such that $\Delta t / \Delta t_{\text{CFL}} = 11.5$. Because of the finite resistivity, the total toroidal current decays and its profile peaks during the evolution, thus altering the linear stability properties of the discharge. The $n = 2$ mode is linearly unstable, grows to finite amplitude, and saturates. The $n = 4$ mode, which was found to be linearly unstable by both TRIM and in Ref. [28], exhibits initial exponential growth at approximately twice the rate of the $n = 2$ mode. This

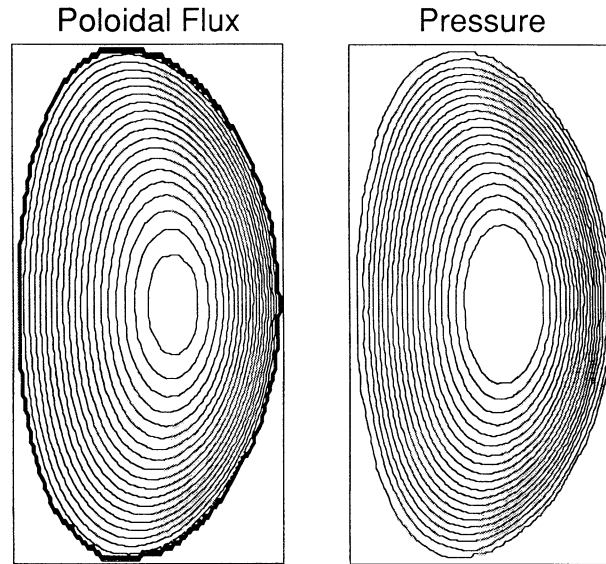


FIG. 29. Poloidal flux surfaces and pressure contours for the elongated Solov'ev equilibrium $\kappa = 2$, $q_0 = 0.5$, $R/a = 3$.

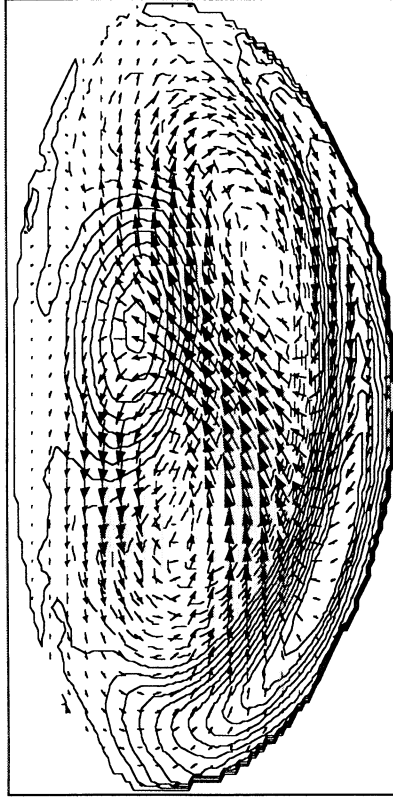


FIG. 30. Linear eigenfunction for the $n = 2$ mode in the Solov'ev equilibrium with $\kappa = 2$, $q_0 = 0.5$, $R/a = 3$.

and the delayed onset of the mode imply that this mode is driven nonlinearly by the $n = 2$ mode rather than by inherent linear instability. The change in the linear stability properties of this mode may be due to the modification of the $n = 0$ component by resistive diffusion, but we have not verified this conjecture. The $n = 1$ and $n = 5$ modes exhibit complete linear stability. The small amplitude increases at late time in these modes is due to nonlinear spectral broadening from the saturation of the $n = 2$ mode. The $n = 3$ mode shows some small indication of linear instability late in the calculation but prior to $n = 2$ saturation. We cannot rule out nonlinear spectral broadening as the cause of this increase. In Fig. 35 we plot contours of the pressure in the saturated state at four different toroidal locations spanning one-half of the torus. The predominantly $n = 2$, $m = 1$ helical displacement of the plasma column is evident.

The same calculation has been performed for the case $\kappa = 2$, $R/a = 3$, $q_0 = 0.5$, with 32 toroidal mesh points (corresponding to toroidal mode numbers $0 \leq n \leq 10$ after dealiasing). The magnetic energy in the modes $1 \leq n \leq 10$ is shown in Fig. 36. The modes $n = 2$ and $n = 3$ exhibit robust linear instability. The $n = 4$ mode also indicates initial linear instability, but makes a transition to being nonlinearly driven by the $n = 2$ mode later in the calculation. The $n = 1$ and $n = 5$ modes are driven by the nonlinear interaction of the $n = 2$ and $n = 3$ modes, and the $n = 6$ mode is nonlinearly driven by the $n = 3$ mode. All other modes appear to be driven by nonlinear spectral broadening. The finite amplitude of all modes at the end of the calculation probably indicates that more toroidal mesh points (modes)

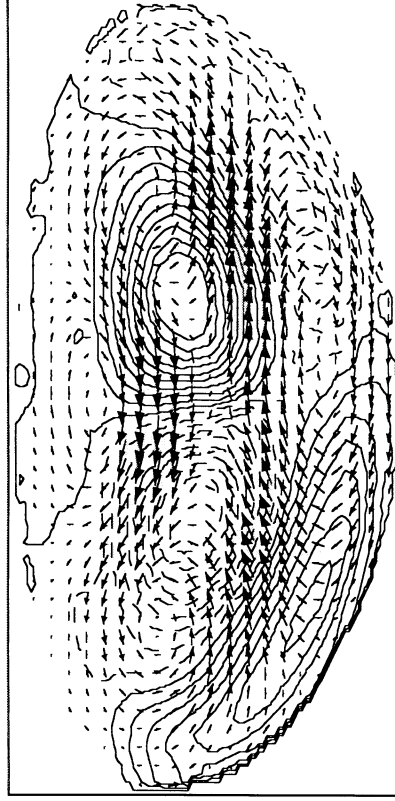


FIG. 31. Linear eigenfunction for the $n = 3$ mode in the Solov'ev equilibrium with $\kappa = 2$, $q_0 = 0.5$, $R/a = 3$.

are required for proper resolution of the nonlinear state. In Fig. 37 we plot contours of the pressure in the saturated state at four different toroidal locations spanning one-half the torus. Again, the helical displacement is topologically $m = 1$, $n = 2$ dominant.

6.4.2. ITER Equilibrium

In Figs. 38a and b we display poloidal flux and pressure contours for an equilibrium that is representative of ITER, an international fusion test reactor that is presently being designed [29]. The outer boundary is the separatrix, or last closed flux surface; it is intended that the plasma is confined within this surface. This equilibrium been constructed to be robustly unstable to an internal kink mode with toroidal mode number $n = 2$. The safety factor profile is shown in Fig. 39. (This equilibrium is unphysical, but it retains the ITER cross-sectional shape and is robustly unstable. It thus serves as a demonstration problem.) The linear instability has been computed with the GATO code [26], which directly solves the resulting linear eigenvalue problem.

The boundary of the calculation is the separatrix, which we take to be rigid and perfectly conducting. The unstructured mesh inside the separatrix with $N_s = 5728$ is shown in Fig. 40. The equilibrium is initialized to this mesh by cubic spline interpolation, and the resulting force imbalance is resolved with viscous damping. We have also found it useful to introduce spatially dependent resistivity, with $S = 10^6$ near the magnetic axis and $S = 10^4$ near the separatrix. Thus resistive flow is always present and true static equilibrium is not

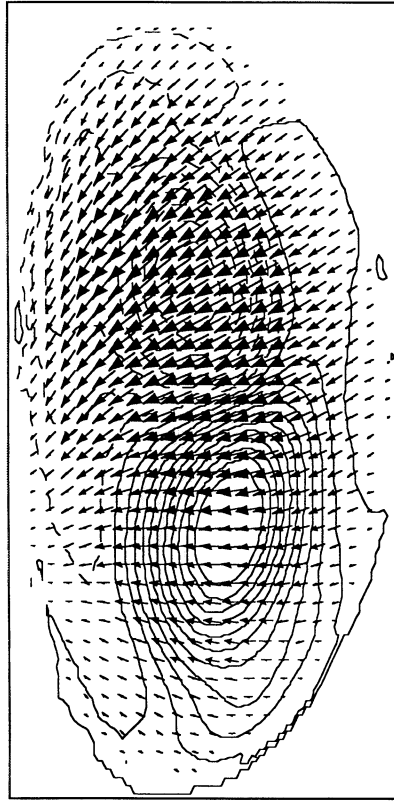


FIG. 32. Linear eigenfunction for the $n = 1$ mode in the Solov'ev equilibrium with $\kappa = 2$, $q_0 = 0.8$, $R/a = 3$. Note the rigid $m = 1$ displacement of this mode.

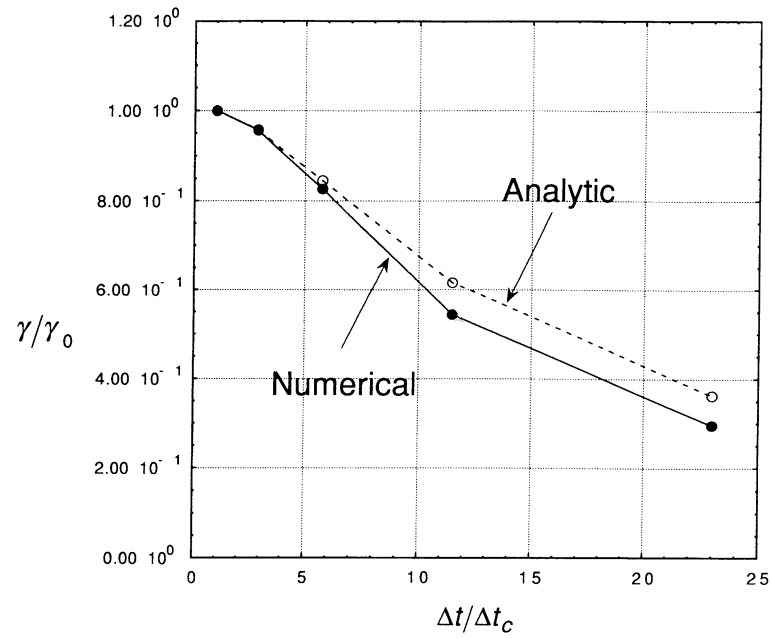


FIG. 33. The effect of the semi-implicit method on the linear growth rate obtained with TRIM for the case $\kappa = 1$, $q_0 = 0.5$, $R/a = 3$, $n = 2$, as a function of the time step (in excess of the CFL limit).

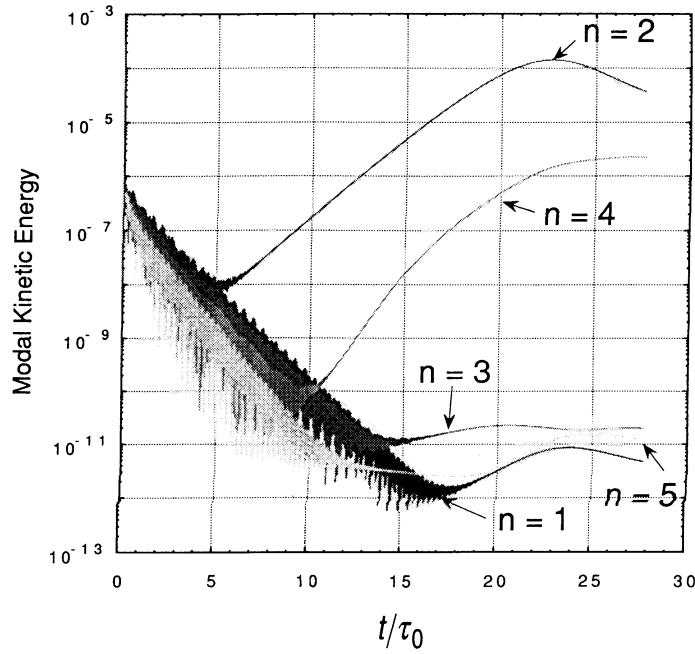


FIG. 34. Kinetic energy in the modes $1 \leq n \leq 5$ versus time for the nonlinear evolution of the Solov'ev equilibrium with $\kappa = 1$, $q_0 = 0.5$, $R/a = 3$.

achieved. The resistivity also causes the current to peak near the magnetic axis, thus altering the safety factor profile.

After axisymmetric relaxation, three-dimensional modes are perturbed with random noise at very low amplitude. For this calculation we use a toroidal mesh with $N_\phi = 8$ toroidal mesh points, so that three toroidal Fourier modes ($n = 0, 1, 2$) are included after dealiasing. This resolution is marginally acceptable for highly accurate calculations, but will demonstrate the utility of the TRIM algorithm for this problem.

The kinetic energy in the $n = 1$ and $n = 2$ modes are shown in Fig. 41. The $n = 2$ mode is unstable and the $n = 1$ mode is stable, in agreement with linear calculations [29].

The linear eigenmode for the poloidal velocity is shown in Fig. 42, where the poloidal velocity vectors are shown at the eight toroidal locations included in the calculation. The flow pattern has the clear counterrotating vortex structure of an internal kink mode with dominant poloidal mode number $m = 1$. This structure is seen to rotate twice around the torus, as required by an $n = 2$ mode.

The instabilities computed here evolve on a fraction of the poloidal Alfvén time, which is almost a factor of 10 longer than the toroidal Alfvén time. Purely explicit methods require that the time step be taken at a fraction of the shortest time scale. In the example computed here we have used the semi-implicit method with a time step 30 times larger than that allowed by explicit numerical stability.

6.4.3. Resistive Instability in a Torus

The results presented in Sections 6.4.1 and 6.4.2 described ideal instabilities, i.e., unstable normal modes of the ideal (infinitely conducting) MHD equations. However, some of the

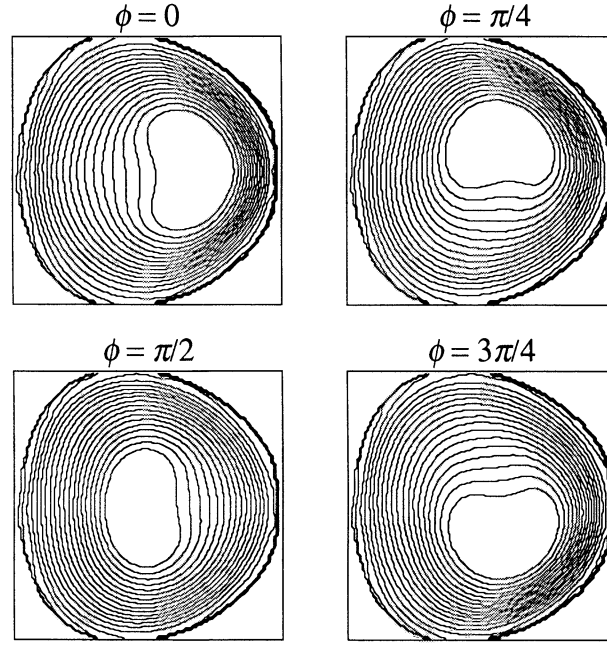


FIG. 35. Pressure contours in the poloidal plane at four different toroidal locations in the nonlinearly saturated state of the Solov'ev equilibrium with $\kappa = 1$, $q_0 = 0.5$, $R/a = 3$.

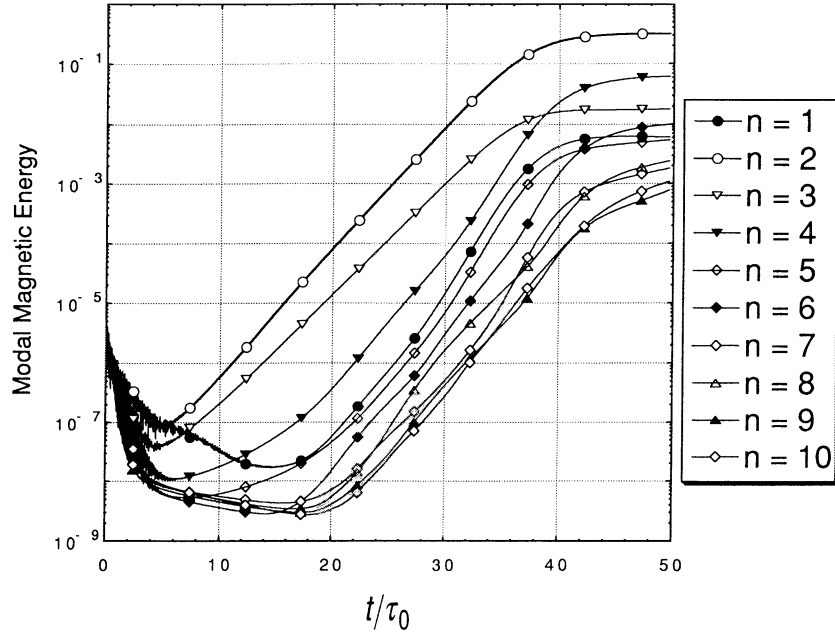


FIG. 36. Magnetic energy in the modes $1 \leq n \leq 10$ versus time for the nonlinear evolution of the Solov'ev equilibrium with $\kappa = 2$, $q_0 = 0.5$, $R/a = 3$.

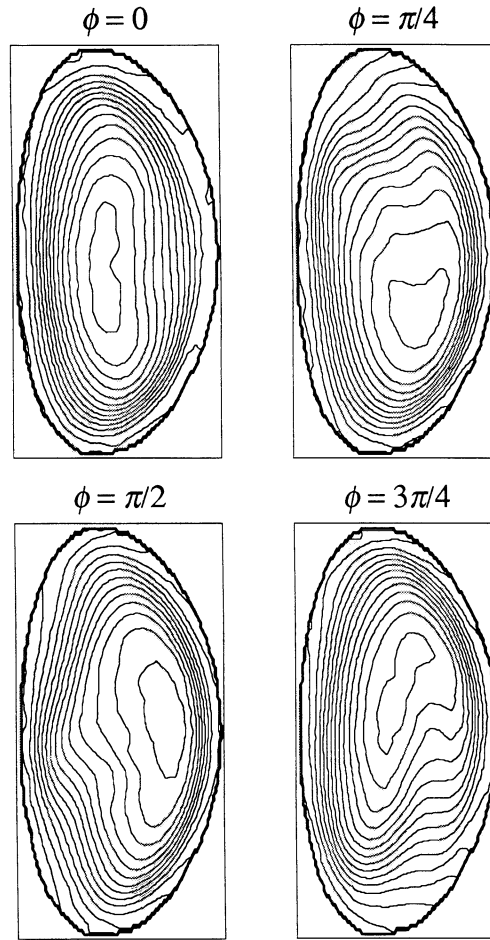


FIG. 37. Pressure contours in the poloidal plane at four different toroidal locations in the nonlinearly saturated state of the Solov'ev equilibrium with $\kappa = 2$, $q_0 = 0.5$, $R/a = 3$.

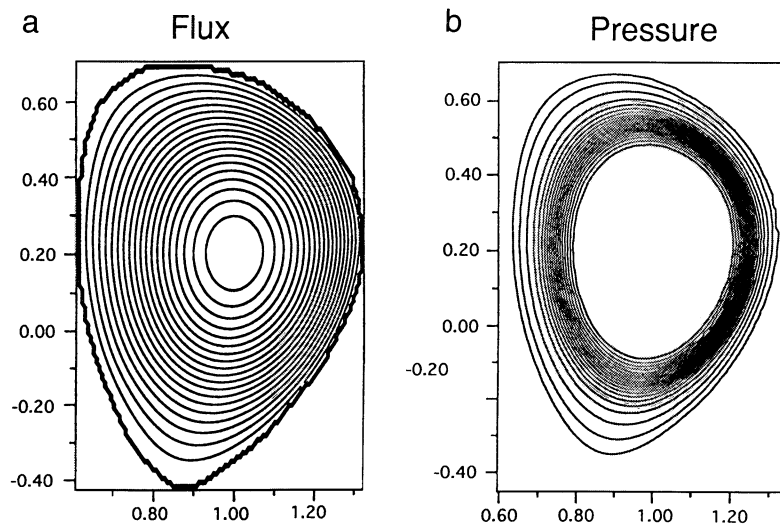


FIG. 38. Contours of poloidal flux and pressure for an ITER equilibrium.

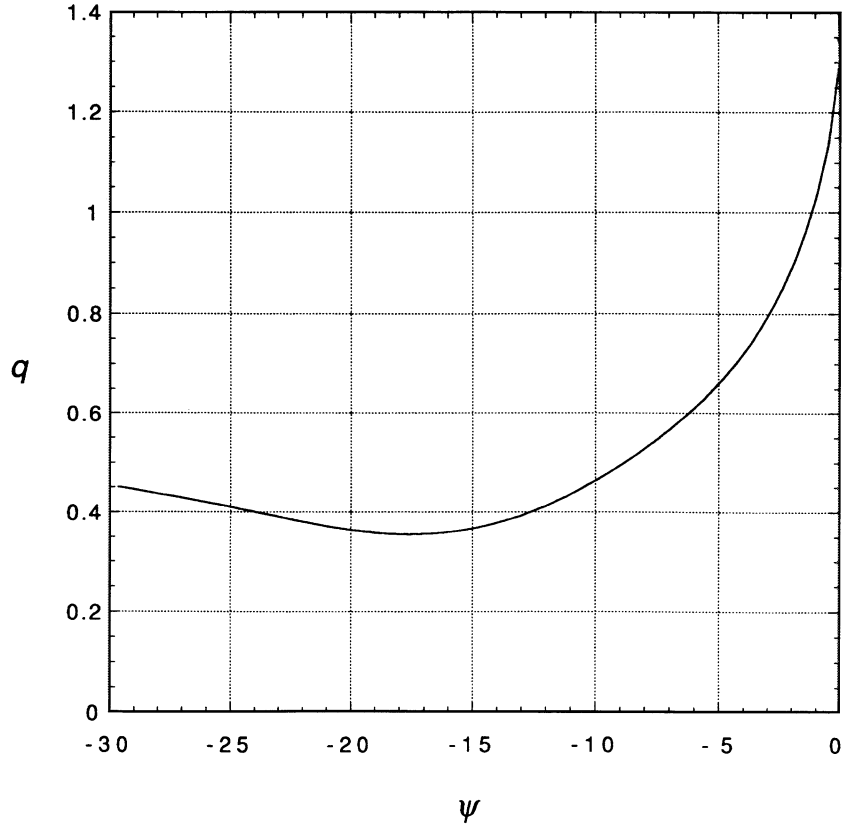


FIG. 39. The safety factor $q(\psi)$ for the ITER equilibrium.

most important instabilities exist only in the presence of finite resistivity. As a result of these modes the magnetic field configuration can change its topological properties, which are otherwise invariant in ideal MHD. These resistive instabilities [30] have no counterpart in ideal MHD and grow on a time scale that is a hybrid of the Alfvén and resistive time scales. The study of these modes has been a primary focus of resistive MHD computations for over 20 years.

We have begun to apply TRIM to resistive instabilities in a torus. We have studied the linear stability of a toroidal equilibrium whose stability properties are well known [31]. For this case, the poloidal cross section of the plasma is circular and the q -profile is given by

$$q(r) = 2 \left(\frac{1 + (r/r_0)^8}{1 + (r_{s2}/r_0)^8} \right)^{1/4}, \quad (84)$$

where r is the minor radius (measured from the center of the circular poloidal cross section), r_{s2} is the radius of the $q = 2$ surface, and r_0 is the width of the current channel. We use $r_{s2} = 0.7$ and $r_0 = 0.6$, which correspond to Run 1, Table 1 of Ref. [31]. The particular equilibrium has been supplied in numerical form [32]. In Ref. [31], the Lundquist number at the $q = 2$ surface was $S = 2 \times 10^4$. For our initial calculations, in order to save computer time, we have used an enhanced resistivity that gives $S = 10^3$ at the $q = 2$ surface.

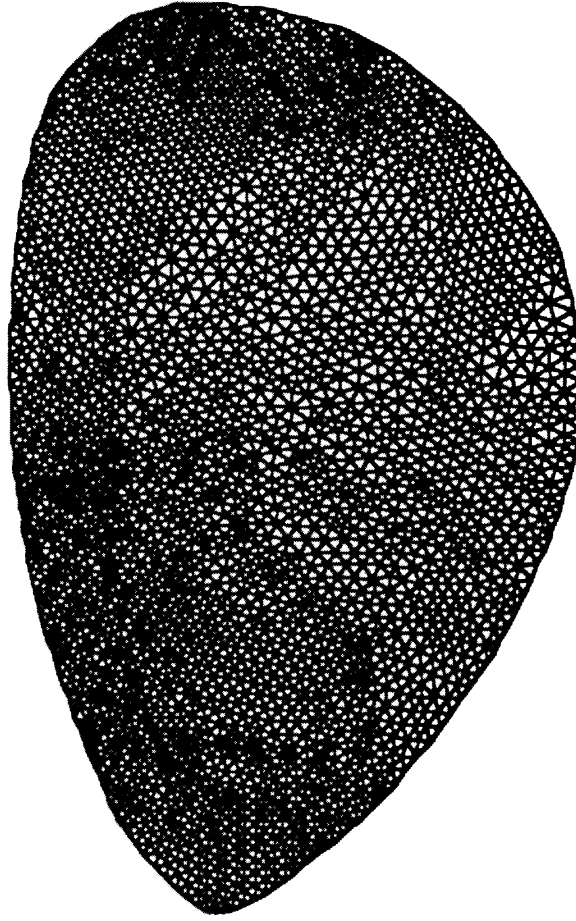


FIG. 40. Unstructured mesh for the ITER equilibrium.

We perturb the initial equilibrium with random noise and consider a linear case with toroidal mode number $n = 1$. We find an exponentially growing instability with a growth rate of $\gamma\tau_{Ap} = 0.01$ (where τ_{Ap} is the poloidal Alfvén time). This is to be compared with the result $\gamma\tau_{Ap} = 0.017$ of Ref. [31] with $S = 2 \times 10^4$. The effect of this resistive instability on the magnetic field topology is shown in Fig. 43, where we use the successive intersections of four different magnetic field lines with the poloidal plane (a Poincaré plot). The field line integration was performed with the code TUBE [33]. The magnetic islands that characterize resistive instabilities correspond topologically to a poloidal mode number $m = 2$, in agreement with Ref. [31].

7. SUMMARY AND DISCUSSION

An algorithm for the solution of the time-dependent, primitive, resistive MHD equations in three-dimensional toroidal geometry has been developed. The algorithm uses an unstructured, triangular mesh in the poloidal plane and a structured, pseudospectral method based

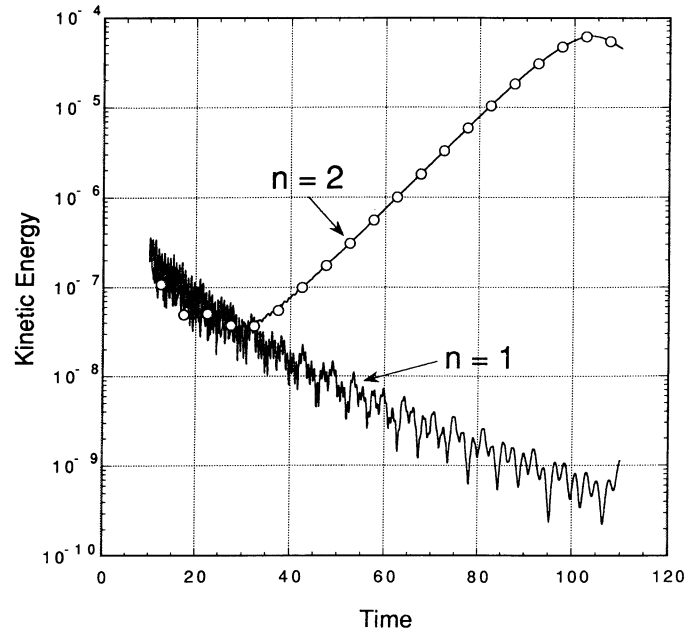


FIG. 41. Kinetic energy versus time for the $n = 1$ and $n = 2$ modes in the ITER equilibrium.

on FFTs in the toroidal coordinate. This allows axisymmetric configurations with arbitrarily complex poloidal geometry to be accurately represented. Boundaries in the poloidal plane need not correspond to flux surfaces or be constrained by coordinate systems. The algorithm is fully conservative and maintains both the magnetic field and current density as solenoidal. Fluxes at cell interfaces are computed with a low-order upwind method. The semi-implicit method is used for time integration.

The algorithm has been applied to four nonlinear test problems: a hydrodynamic shock tube; an MHD shock tube; supersonic flow past a sphere (both with and without an initial dipole magnetic field); and, growth and saturation of toroidal instabilities. For both the hydrodynamic and MHD shock tube problems, good agreement with previous results has been obtained. The primary inaccuracy is due to the numerical diffusion introduced by the low-order fluxes. Mesh adaption and refinement has been successfully applied to both the hydrodynamic and MHD cases and to the case of supersonic flow past a sphere. Linear growth and nonlinear saturation of three-dimensional kink modes in two analytic equilibria and in a highly elongated toroidal equilibrium representative of the ITER design have been computed. Time-step converged linear growth rates agree with previous linear stability calculations to within 20%. The nonlinear evolution of these modes has shown nonlinear mode coupling and spectral broadening and has demonstrated the utility of the semi-implicit method of time integration for these calculations. The linear growth of a resistive tearing instability in toroidal geometry has also been calculated.

We briefly remark on the order of accuracy and efficiency of the algorithm. In Fig. 44 we plot the numerical damping rate inherent in the algorithm as a function of number of

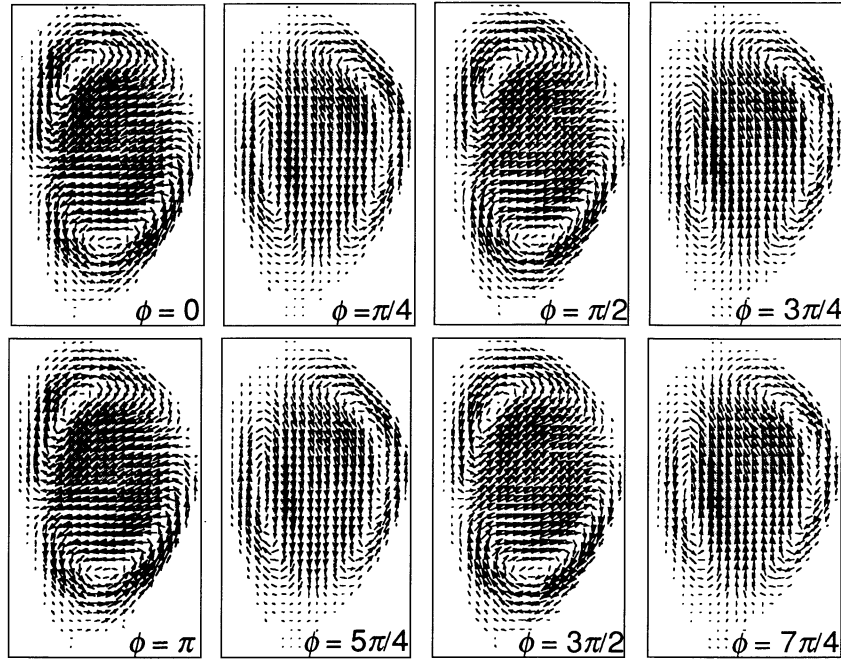


FIG. 42. Poloidal velocity in the linear eigenmode at eight different toroidal locations.

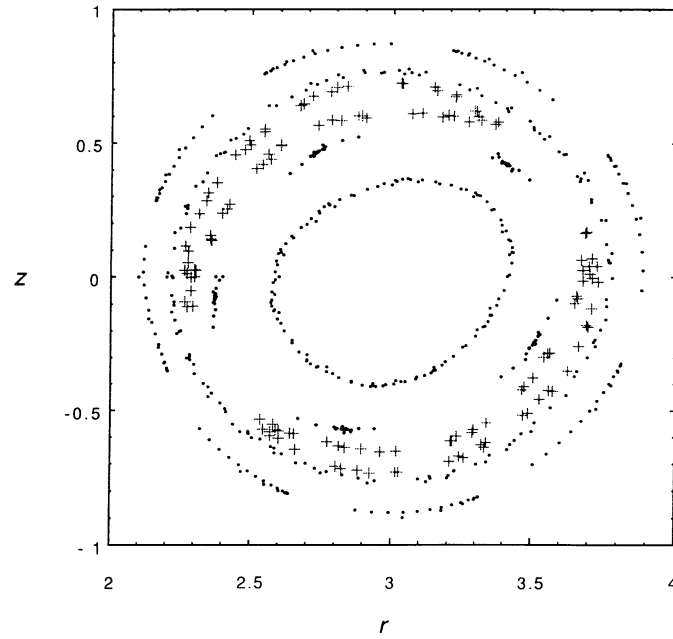


FIG. 43. Intersection of five different field lines with the poloidal plane showing the magnetic island that results from an unstable $n = 1$ resistive instability. The topologically $m = 2/n = 1$ structure is evident.

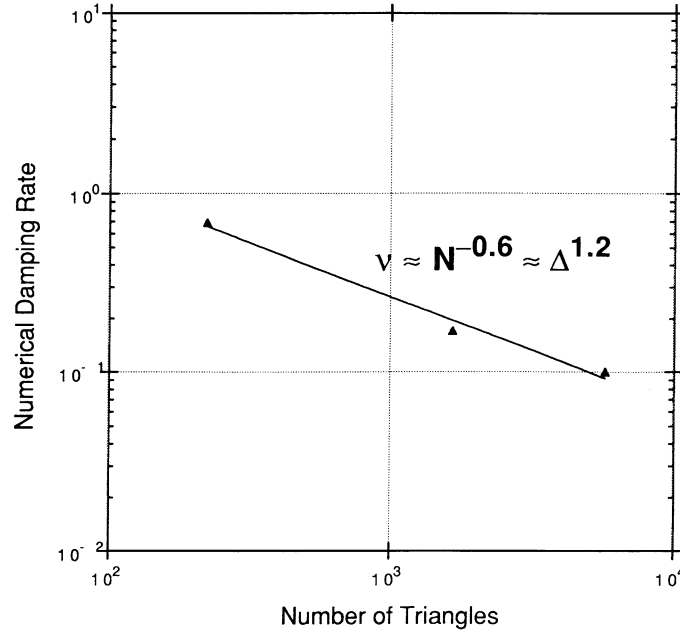


FIG. 44. Numerical damping rate vs number of triangles.

triangles. These results were obtained during the relaxation of the Solov'ev equilibrium, as described in Section 6.4.1. We see that the numerical damping rate is approximately linear in $\delta \approx (\Delta a_s)^{1/2}$, confirming the first-order nature of the algorithm. This damping is consistent with the low growth rates found for these cases. The efficiency of the algorithm is displayed in Fig. 45, where we plot the CPU time required to compute for one e-folding time of a linear instability in the Solov'ev equilibrium as a function of $\Delta t / \Delta t_{\text{CFL}}$, the ratio of the actual time step to the time step allowed by the explicit CFL condition. The behavior illustrated here is influenced by two factors. First, as the time step is increased above the CFL limit, the semi-implicit coefficient, Eq. (72), becomes larger, and consequently more iteration are required to invert the semi-implicit operator. Second, the e-folding time itself increases (the growth rate decreases) as the time step is increased (see Fig. 33). The most efficiency (i.e., the minimum CPU time per e-folding time) is obtained at about $\Delta t / \Delta t_{\text{CFL}} = 10$.

Several issues have arisen in the course of our investigation that we believe require further research. These are enumerated below.

The first issue concerns the most efficient and accurate use of the primary and dual meshes, and the placement of dependent variables on them. In this work we have used the Delaunay triangles as the primary control volume and have chosen to define all volume densities (momentum, mass, and energy) at their centroids. All physical boundaries consist of triangle edges. We have not made use of the dual control volume elements consisting of the polygons centered at triangle vertices with edges connecting triangle centroids. (The edges of these polygons are used to define components of the magnetic field and current density.) With the present scheme differential operators such as the gradient and the

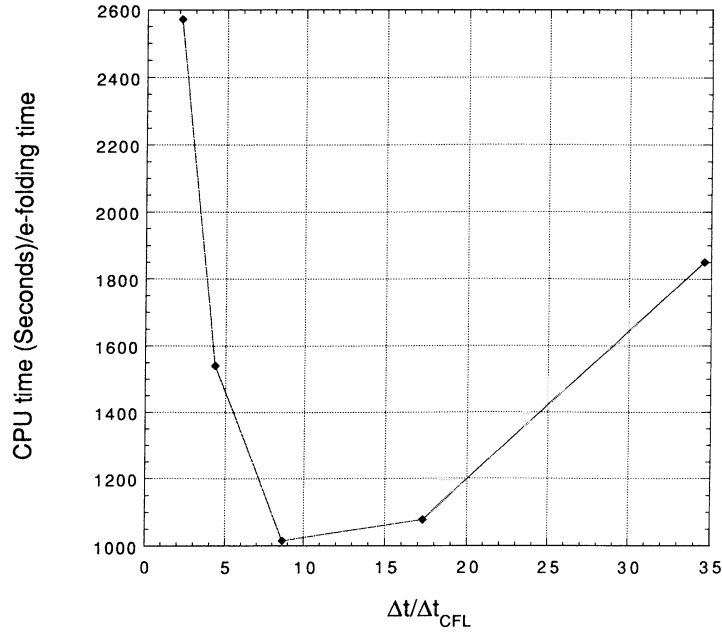


FIG. 45. CPU time per e-folding time for a linear instability in the Solov'ev equilibrium versus $\Delta t / \Delta t_{\text{CFL}}$, the ratio of the time step to that allowed by the CFL condition.

Laplacian acting on triangle-centered densities couple more than nearest neighbor triangles. Our experience with rectangular, structured meshes [16] indicates that the use of staggered, overlapping volume elements leads to the most compact, accurate, and physically motivated algorithms. In those methods, the pressure and momentum are not collocated as they are here, but are defined at the centers of the staggered primary and dual meshes, respectively. We have not experienced any severe problems that can be directly attributed to the non-compact formulation described in this paper, but the present algorithm seems to require somewhat more artificial viscosity to assure robustly stable computations than methods that use rectangular, structured meshes. Our initial attempts to formulate an exactly equivalent method using triangles and polygons has led to problems in consistently defining boundary edges and applying boundary conditions.

The second issue concerns interpolation. In the present algorithm, interpolation from centroids to vertices, vertices to centroids, centroids to edges, edges to vertices, and vertices to edges are all required. The form of the interpolation can affect the accuracy and stability of the calculation. As described in Section 4.3, some of these interpolation schemes can become quite complicated and can lead to coupling beyond nearest neighbors. We have not devised a method for MHD using either rectangular or triangular meshes that does not require some interpolation (or averaging) from one grid to another. Interpolation is required during mesh refinement and coarsening. The number of interpolations per time step is also affected by the choice of primary and dual meshes. The issues of accuracy and required number of interpolations, and their affect on the performance of the algorithm, must be better understood.

The third issue concerns the criteria used for dynamic refinement and coarsening of the mesh. In Section 2.7 we presented criteria for adding or deleting triangles that are based on either the normalized average Laplacian operator or the normalized gradient. For the results presented in Section 6, we have used these criteria in conjunction with the mass density. Other criteria have been used in computational hydrodynamics [18]. Other problems may require still other criteria. For example, criteria based on current density may be useful for magnetic reconnection problems. The proper criteria for resistive MHD is yet to be determined.

The fourth issue concerns the structure of the mesh itself. Delaunay triangles have many desirable properties. The algorithm is most accurate for equilateral triangles, for then the centroid dual mesh and the Voronoi dual mesh are equivalent. Deviations from equiangularity introduce errors, and highly obtuse triangles can lead to spikes in high order derivatives, such as current density. Mesh refinement can lead to large variations in triangle size and shape over the mesh, even though the Delaunay triangulation maximizes equiangularity in a global sense. These large variations can in turn affect the diagonal dominance of the Laplacian operator and cause the conjugate gradient algorithm to fail to converge. What is needed is a method for systematically redistributing the vertices in the poloidal plane to assure that all triangles are at least acute and that variations in mesh size are smoothly distributed in space. Clearly, more fundamental work needs to be done in this area.

We have used low order approximations for the calculation of interface fluxes. The accurate computation of these fluxes has occupied the attention of computational hydrodynamicists for several years, and it has proven to be a crucial issue in the accurate engineering application of these methods. Improvements in these methods for MHD must eventually be addressed.

Finally, we remark on the maximum Lundquist number (minimum dissipation) accessible by the TRIM algorithm. As is the case with all nonlinear calculations, we have found that, in the nonlinear regime, it is necessary to keep both the cell magnetic Reynolds' number, $R_{M\Delta} = v\delta/\eta$, and the cell viscous Reynolds' number, $R_\Delta = v\delta/\nu$, of order unity. The Lundquist number is related to the cell magnetic Reynolds' number by $S = (v_A/v)(L/\delta)R_{M\Delta}$. The maximum Lundquist number is therefore determined by both the particular problem under consideration (through the flow velocity and the Alfvén velocity) and by the resolution (through the cell size δ , which is proportional to the square root of the number of triangles). Thus, for a case with $v_A/v \sim 10$ and with 10^4 triangles (equivalent to a grid of 100×100 on a rectangular mesh), $S_{\max} \sim 10^3$. This is consistent with our experience. For a given problem, S_{\max} can only be increased by decreasing the size of the triangles. However, the scaling is not favorable: to increase S_{\max} by a factor of 10 with uniform triangle size, the number of triangles must be increased by a factor of 100 (\sim an order of magnitude for each spatial dimension). This is not to say that accurate but limited calculations cannot be performed at higher values of S . (See, for example, the ideal mode in the ITER equilibrium described in Section 6.4.2.) Indeed, the linear growth and initial nonlinear saturation of tearing modes in tokamaks can proceed for a time until the nonlinear coupling cascades significant energy to the shortest length scale δ . All that is required is that the linear mode structure near the resonant surface be well resolved, which can be accomplished by packing grid cells there. However, if $R_{M\Delta} > 1$, this energy will eventually and inevitably build to a level sufficient to render that calculation meaningless. This is the case for all nonlinear algorithms, not just the one described here.

ACKNOWLEDGMENTS

Many scientists have contributed to the work described in this paper. The logical data structure for the unstructured triangular mesh and the routines for dynamic mesh adaption were developed and written by one of the authors (Dr. I. Lottati) and Dr. S. Eidelman, who kindly supplied them from their hydrodynamics code. Valuable discussions on many aspects of unstructured meshes and mesh adaption were held with our colleagues Dr. H. R. Strauss, Dr. A. Koniges, Dr. A. Glasser, Dr. A. Kuprat, Dr. D. Longcope, and Dr. D. C. Barnes. Dr. A. Turnbull provided the ITER equilibrium and linear stability results, and Dr. A. Aydemir provided the equilibrium used for the calculation of resistive instabilities. This work was performed under Grant DE-FG03-91ER54124 with the U.S. Department of Energy.

REFERENCES

1. S. Migliuolo, *Nucl. Fusion* **33**, 1721 (1993).
2. L. Chen, R. B. White, and M. N. Rosenbluth, *Phys. Rev. Lett.* **52**, 1122 (1984).
3. B. Coppi and F. Porcelli, *Phys. Rev. Lett.* **57**, 2272 (1986).
4. B. Coppi, S. Mogliuolo, and F. Porcelli, *Phys. Fluids* **31**, 1630 (1988).
5. B. A. Carreras, H. R. Hicks, J. A. Holmes, and B. V. Waddell, *Phys. Fluids* **23**, 1811 (1980).
6. D. C. Barnes, private communication, 1995.
7. S. Ortolani and D. D. Schnack, *Magnetohydrodynamics of Plasma Relaxation* (World Scientific, Singapore, 1993).
8. *Unstructured Grid Methods for Advection Dominated Flows*, at the von Kármán Institute for Fluid Dynamics, Rhodé-Saint-Genève, Belgium, 2–6 March 1992 and at the NASA Ames Research Center, Moffett Field, CA, 28 Sept. 2–Oct. 1992 (Advanced Group for Aerospace Research and Development (AGARD), 7 Rue Ancelle, 92200 Neuilly-sur-Seine, France, 1992). [AGARD R-787]
9. R. Courant and K. O. Friedrichs, *Supersonic Flows and Shock Waves* (Interscience, New York, 1948).
10. H. R. Strauss, *Phys. Fluids* **19**, 134 (1976).
11. H. R. Strauss, *Phys. Fluids* **20**, 1354 (1977).
12. H. R. Hicks, B. Carreras, J. A. Holmes, D. K. Lee, and B. V. Waddell, *J. Comput. Phys.* **44**, 46 (1981).
13. D. S. Harned and W. Kerner, *J. Comput. Phys.* **60**, 62 (1985).
14. D. S. Harned and W. Kerner, *Nucl. Sci. Eng.* **92**, 119 (1986).
15. D. S. Harned and D. D. Schnack, *J. Comput. Phys.* **65**, 57 (1986).
16. D. D. Schnack, D. C. Barnes, Z. Mikić, D. S. Harned, and E. J. Caramana, *J. Comput. Phys.* **70**, 330 (1987).
17. T. J. Barth, Aspects of unstructured grids and finite-volume solvers for the Euler and Navier–Stokes equations, in Ref. [8].
18. I. Lottati and S. Eidelman, *Appl. Num. Math.* **14**, 353 (1994).
19. P. J. Green and R. Sibson, *Comput. J.* **21**, 191 (1983).
20. R. Löhner, K. Morgan, and O. C. Zienkiewicz, *Comput. Math. Appl. Mech. Eng.* **51**, 441 (1985).
21. R. Löhner, The efficient simulation of strongly unsteady flows by the finite element method, AIAA-87-055, 1987.
22. R. D. Rausch, *Time Marching Aeroelastic and Spatial Adaption Procedures on Triangular and Tetrahedral Meshes Using an Unstructured Grid Euler Method*, Ph.D. thesis, Purdue University, Decemeber 1992.
23. Z. Mikić and E. C. Morse, *J. Comput. Phys.* **61**, 154 (1985).
24. G. Sod, *J. Comput. Phys.* **27**, 1 (1978).
25. M. Brio and C. C. Wu, *J. Comput. Phys.* **75**, 400 (1988).
26. R. Gruber *et al.*, *Comput. Phys. Commun.* **24**, 363 (1981).
27. L. S. Solov'ev, *Sov. Phys. JETP* **26**, 400 (1968).

28. D. Berger, L. C. Bernard, R. Gruber, and F. Troyon, *J. App. Math. Phys. (ZAMP)* **31**, 113 (1980).
29. A. Turnbull, private communication, 1994.
30. H. P. Furth, J. Killeen, and M. N. Rosenbluth, *Phys. Fluids* **16**, 1054 (1973).
31. B. V. Waddell, B. Carreras, H. R. Hicks, and J. A. Holmes, *Phys. Fluids* **22**, 896 (1979).
32. A. Y. Aydemir, private communication, 1995.
33. A. A. Mirin, D. R. Martin, and N. J. O'Neill, *Comput. Phys. Commun.* **54**, 183 (1989).

NONLINEAR MAGNETOHYDRODYNAMIC EVOLUTION OF LINE-TIED CORONAL LOOPS

ROBERTO LIONELLO¹ AND MARCO VELLI

Dipartimento di Astronomia e Scienza dello Spazio, Università di Firenze, Largo Fermi 5, I-50125 Firenze, Italy; lionello@arcetri.astro.it, velli@arcetri.astro.it

GIORGIO EINAUDI

Dipartimento di Fisica, Università di Pisa, Piazza Torricelli 2, I-56126 Pisa, Italy; einaudi@astr11pi.difi.unipi.it

AND

ZORAN MIKIĆ

Science Applications International Corporation, 10260 Campus Point Drive MS-C2, San Diego, CA 92121-1578; mikic@iris023.saic.com
 Received 1997 March 27; accepted 1997 September 30

ABSTRACT

Simulations of the nonlinear evolution of the $m = 1$ kink mode in magnetic flux tubes with line-tying boundary conditions are presented. The initial structure of the flux tube is intended to model a solar coronal loop that either has evolved quasi-statically through sequences of equilibria with increasing twist due to the application of localized photospheric vortex flows or has emerged with a net current through the photosphere. It is well known that when the twist exceeds a critical value that depends on its radial profile and on the loop length, the loop becomes kink unstable. The nonlinear evolution of the instability is followed using a three-dimensional MHD code in cylindrical geometry, in different types of magnetic field configurations, with the common property that the current is confined within the same radius, so that the magnetic field is potential in the external regions. The differences reside in the net axial current carried by the structure, ranging from a vanishing current (corresponding to an outer axial potential field) to a high current (corresponding to an outer almost azimuthal potential field). It is shown that, during the nonlinear phase of the instability, loops develop current sheets and, consequently, their evolution becomes resistive with the occurrence of magnetic reconnection. The dependence of the topology of the currents at saturation on the initial magnetic structure, the details of the reconnection phenomenon, and the resistive dissipation mechanism are examined. Finally, the impact of the results on the understanding of coronal activity is discussed.

Subject headings: MHD — Sun: corona — Sun: magnetic fields

1. INTRODUCTION

The existence of long-lived magnetic loop structures in the solar corona has driven a great amount of work on the linear stability of axially symmetric equilibria. The reason for the stability of coronal current-carrying loops has been recognized to be the effect of line-tying, i.e., the axial boundary conditions due to the high-density photosphere. For a given radial profile of the current density, there exists a critical length above which the structure is magnetically unstable (Raadu 1972; Hood & Priest 1979, 1981; Einaudi & Van Hoven 1981, 1983; Velli, Einaudi, & Hood 1990a; Foote & Craig 1990).

Axially symmetric force-free equilibria may be divided into two generic classes: equilibria that contain a non-vanishing net axial current and that have a poloidal magnetic field which decreases as $1/r$ at large distances from the loop axis, and equilibria for which the poloidal field vanishes at the edge of the current-carrying region, which therefore carry a zero net axial current. The latter type of equilibrium is obtained when a magnetic structure, which is initially close to potential, is energized by currents induced via the magnetic field footpoint motions. Short correlation-time motions produce a random energy input, while longer correlation-time motions are capable of a quasi-coherent energy input that may be stored in a stable fashion in a

coronal loop, provided the loop is not too long (Mikić, Schnack, & Van Hoven 1989, 1990). The typical loop generated in this way carries a net axial current that vanishes beyond a radius comparable in dimension to that of the region of random motions.

The former kind of equilibrium requires a closing current to flow within the photosphere and may arise when a magnetic flux tube emerges from below the photosphere carrying a net axial current; as the emergence proceeds the loop becomes longer, reaching its critical stability length and crossing this threshold.

In reality, the distinction between such cases is probably not a strong one, as loops are continually excited by footpoint motions as well as emerging in a nonpotential manner from the photosphere. Nonetheless, we consider both cases here.

In this paper we study the evolution of a coronal loop when it becomes unstable, adopting different initial configurations that are intended to model its structure at the end of the energy buildup phase, which is not followed in time. Therefore, we start the simulations by perturbing an equilibrium at a chosen “distance” from marginal stability, as we shall discuss in more detail below. Linear instability results are fundamental in determining the thresholds for the onset of dynamical behavior; the ideal linear eigenfunctions may also be used as initial perturbations in a fully nonlinear simulation.

The paper is organized as follows. In § 2 we present the physical model used, the equations solved, and the bound-

¹ Now at Science Applications International Corporation, 10260 Campus Point Drive MS-C2, San Diego, CA 92121-1578.

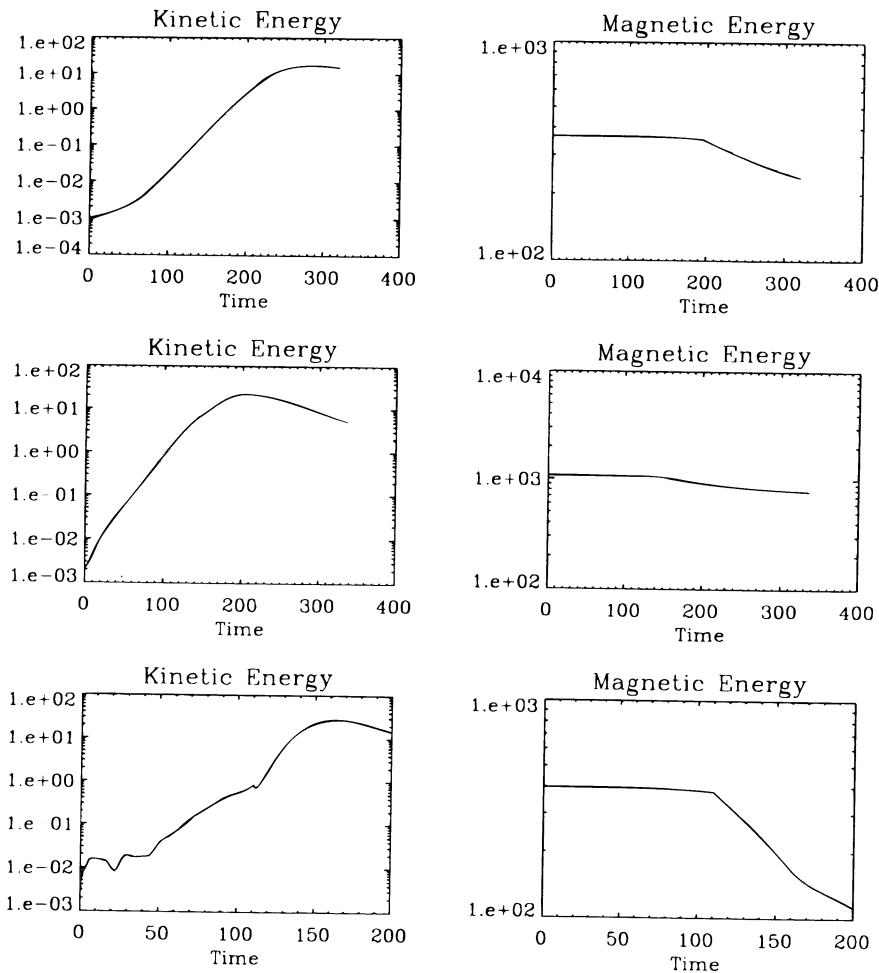


FIG. 11.—Kinetic (left panel) and nonpotential magnetic (right panel) energies as functions of time for equilibria FC1 (top panel), FC2 (middle panel), and NC (bottom panel).

particular, evolution of equilibrium NC, which maintains its large-scale magnetic structure and evolves on the fastest timescale, may provide a viable physical model for compact loop flares. FC models, which produce weaker current sheets and dissipate smaller amounts of energy, and evolve on longer timescales, would be expected to contribute to coronal heating, and may explain the long-lived hot loops observed by *Yohkoh*.

In summary, line tying has two contrasting effects on the behavior of coronal loops. For sufficiently short loops, it acts as a stabilizing agent to prevent perturbations from growing, allowing loops to build up and store magnetic energy. Once the loops become unstable, line tying can cause current sheets to form, resulting in an enhanced level of energy dissipation compared to non-line-tied configurations. It would be worthwhile to extend the calculations presented here to include a more realistic description of the thermodynamics, and to include the effect of toroidal curva-

ture, which may cause a rapid outward expansion of loops as they are twisted (Amari et al. 1996).

We would like to thank Hubert Baty, Claudio Chiuderi, Jon Linker, Dalton Schnack, and Gerard Van Hoven for helpful discussions. Computations were performed at the Interuniversity Consortium of the Northeastern Italy for Automatic Computing (CINECA) and at the National Energy Research Supercomputer Center (NERSC) at Livermore, California. This work was supported in part by a NASA Space Physics Theory Program contract (NAS 5-96081) to Science Applications International Corporation (SAIC). R. L. wishes to thank Roberto Casini for collaboration in developing imaging software; G. E. and R. L. wish to thank the University of California, Irvine (UCI), and SAIC for their kind hospitality during the development of this work. The visits of G. E. and R. L. to UCI were supported, in part, by NSF and NASA.

REFERENCES

- Amari, T., Luciani, J. F., Aly, J. J., & Tagger, M. 1996, *ApJ*, 466, L39
 Baty, H., & Heyvaerts, J. 1996, *A&A*, 308, 93
 Chiuderi, C., & Einaudi, G. 1981, *Sol. Phys.*, 73, 89
 Foote, B. J., & Craig, I. J. D. 1990, *ApJ*, 350, 437
 Einaudi, G., Lionello, R., & Velli, M. 1997, *Adv. Space Res.*, 19, 1875
 Einaudi, G., & Van Hoven, G. 1981, *Phys. Fluids*, 24, 1092
 ———. 1983, *Sol. Phys.*, 88, 163
 Hood, A. W., & Priest, E. R. 1979, *Sol. Phys.*, 64, 303
 ———. 1981, *Geophys. Astrophys. Fluid. Dyn.*, 17, 297
 Lionello, R. 1997, Ph.D. thesis, Univ. Florence
 Lionello, R., Mikić, Z., & Schnack, D. D. 1998, *J. Comput. Phys.*, in press
 Mikić, Z., Schnack, D. D., & Van Hoven, G. 1989, *ApJ*, 338, 1148
 ———. 1990, *ApJ*, 361, 690
 Raadu, M. A. 1972, *Sol. Phys.*, 22, 425
 Velli, M., Einaudi, G., & Hood, A. W. 1990a, *ApJ*, 350, 419
 ———. 1990b, *ApJ*, 350, 428
 Velli, M., Lionello, R., & Einaudi, G. 1997, *Sol. Phys.*, 172, 257

of the very rapid increase of growth rate as marginality is crossed.

4. NONLINEAR RESULTS

We have performed three simulations to study the nonlinear evolution of kink instabilities that develop in the FC and NC fields. The MHD equations (1)–(4) are advanced numerically in time by means of a three-dimensional semi-implicit algorithm, which makes use of a Fourier expansion in the poloidal direction and of a finite-difference technique in the axial and radial directions. We define a radial mesh extending between $r = 0$ and $r = R$, where we set a conducting boundary. Since we expect to find current concentrations in the vicinity of the center of the cylinder, the mesh is designed as in Mikić et al. (1990), with greater resolution for small r 's and increasingly sparser at greater radii: 13% of the points are within $r = 0.05R$, 26% are within $r = 0.1R$, 55% are within $r = 0.25R$, and 82% are within $r = 0.5R$. The ratio of the largest Δr to the smallest is 13.9. R must be large enough to avoid artificial stabilizing effects on the evolution of the system. We choose $R = 20$ for the FC fields, which develop global kink modes, and $R = 12.5$ for the NC equilibrium, in which the internal kink mode is effectively confined by the outer constant axial field. The axial and poloidal meshes are taken to be uniform in both cases. A $63 \times 63 \times 32r - z - \theta$ mesh is employed. We use a dealiased Fast Fourier Transform algorithm, so that only modes with $0 \leq m \leq 10$ are retained (equivalent to $\frac{2}{3}$ of available Fourier space). The inversion of self-adjoint matrices, generated by the semi-implicit formulation and by the fully implicit treatment of the viscous and resistive terms, is accomplished through a conjugate gradient solver with diagonal preconditioning. The details of the code are described elsewhere (Lionello, Mikić, & Schnack 1998). The initial conditions assume constant mass density, $\rho = 1$, constant temperature, a plasma beta $\beta = 0.01$, which is typical of the solar corona and an $m = 1$ perturbation of amplitude $v \sim 6 \times 10^{-4}$ is applied to the three equilibria described above. In order to save computing time the radial and axial profiles of the initial perturbation are derived from the linear code.

The computation is started with no resistivity and with a small value of the viscosity, $\nu \sim 10^{-3}$, to be able to follow the entire ideal linear phase of the instability. We find that in all three cases during the first stage of the nonlinear ideal evolution small scales are created in all three directions and eventually resistivity *must* be introduced in the computation in order to dissipate the energy which accumulates at small scales and to avoid the development of numerical instabilities (Einaudi et al. 1997). Therefore after a time T_r , whose value depends on the equilibrium under investigation, the resistive terms are turned on with $\eta = 10^{-2}$ ($T_r = 195, 160$, and 115 , respectively, for FC1, FC2, and NC), and at the same time the viscosity is set to the same value. Such a value is necessary to describe the behavior of small scales in our moderate resolution simulations properly. Resistivity is actually important only locally where small scales are created by the nonlinear dynamics. Attempts to link the inclusion of resistivity to the magnitude of the currents (to avoid the diffusion of the large-scale structures) in our code were unsuccessful, probably because of the implicit treatment of the dissipative terms.

Once resistivity is turned on, the instability eventually saturates in a timescale that appears to be independent of

the equilibrium adopted even though the linear timescales are different. Such a behavior is well described by the time history of the magnetic and kinetic energies contained in the different poloidal modes, which is shown in Figure 6 (note the cusps in the profiles at the time when resistivity is turned on).

In all runs an $m = 0$ transient mode shows up in the kinetic energy history, which is due to adaptation of the analytical equilibria to the grid. We have derived the approximate growth rate of the $m = 1$ mode in the three cases, finding a satisfactory agreement with the growth rates obtained using the linear code presented in Figure 3. From Figure 6 it is also clear that the growth of the higher m modes is due to forcing from the $m = 1$ mode via quadratic nonlinear terms, since, e.g., the $m = 2$ mode, once the $m = 1$ mode is well into the exponential growth phase, also exhibits exponential growth with a rate that is twice as large as that of the $m = 1$.

In order to investigate the distribution of the currents in the loop and to better understand the physical meaning of the creation of small scales, we have computed the modulus of the current density at different heights for the three equilibria at the beginning of the resistive phase, and we present the results for $z = 0$ and $z = \frac{2}{3}L$ in Figure 7. It is evident that the introduction of the resistivity is necessary to correctly describe the evolution of current peaks that have been formed during the ideal nonlinear evolution. The overall topology of the current structure differs considerably from one equilibrium to the other, reflecting the different physical nature of the current concentration. We have already described how for model FC1 the kink extends far into the regions of the original potential field and the current distribution does not show any strong concentration in the linear phase. In the nonlinear phase two current peaks develop, one per each half loop, the location of the peaks depending on the total length of the loop. This fact can be seen comparing the results for FC1 with the results presented in Velli et al. (1996) for their model *a*, which has the same radial structure as FC1 and length $L = 25$. The current concentrations at $z = 0$ are just the “tips” of the two layers developed in the legs of the loop. The formation of such current layers is a direct consequence of the fact that the magnetic lines cannot move at photospheric levels producing strong gradients where the kink folds on itself in each leg of the loop.

The presence of “resonant” regions in the linear phase can be another possible cause for the formation of current concentrations in the subsequent nonlinear phase. In a “resonant” region the ideal terms determining the time evolution of the radial component of the perturbed magnetic field go through zero, generating a current concentration within the region. For both FC2 and NC models the “resonant” region is located at the loop apex and current sheets develop there. The difference between the two models is that in the NC case only the internal part of the plasma column moves outward, piling up magnetic energy at the border with the potential region and contributing to the local enhancement of the current. In the FC2 case the radial displacement is more extended and therefore the resonant region is carried by the flows outward with a smaller opposition of the potential field.

In all cases current layers are formed and the evolution becomes resistive with a consequent occurrence of magnetic reconnection (see also Baty & Heyvaerts 1996).

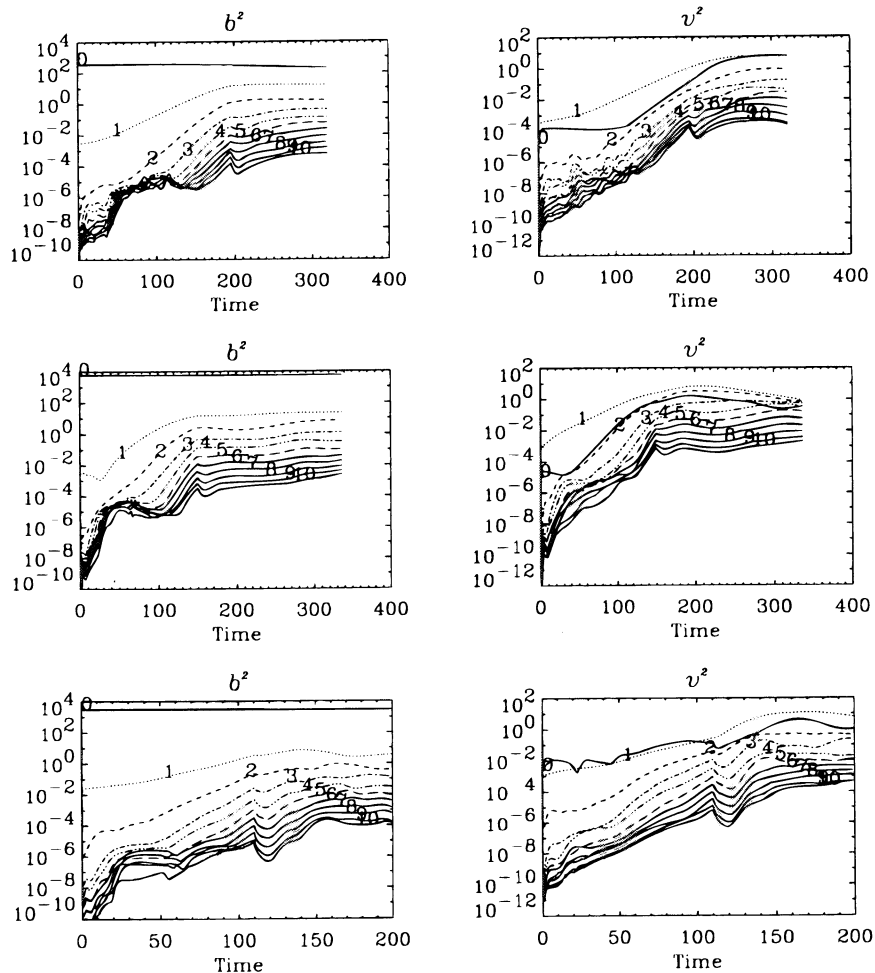


FIG. 6.—Poloidal mode histories of the magnetic and kinetic energy for equilibria FC1 (*top panel*), FC2 (*middle panel*), and NC (*bottom panel*)

In Figures 8 and 9 we present field line plots for the FC and NC models at the beginning of the resistive phase and at saturation of the instability when all poloidal modes start declining. The lines start from the bottom of the loop at different radii ($r = 2, 4$) and angles, in the region where the current flows, and are integrated until they reach the top. This choice of field line imaging makes the representation asymmetrical, though clearly a perfectly symmetrical image would appear if we plotted also the corresponding field lines originating from the top of the loop. The axial dimensions of the structures are proportional to the real lengths of the loops. Each magnetic line connects two fluid elements that are rooted in the photosphere at opposite sides of the loop. During the ideal phase the field line can only be bent and twisted since the fluid elements in the photosphere cannot move. In the resistive phase the field lines can reconnect, altering the field topology and therefore the connectivity between fluid elements in the photosphere.

The fact that reconnection has occurred during the resistive nonlinear evolution of all three models is evident from a comparison of left and right panels in Figures 8 and 9. Following the previous discussion on the properties of the dynamics of the three models, it is not surprising to notice that the final magnetic topologies of the three models differ considerably even if the physical mechanism determining the evolution is the same in all cases. This is due to the fact that the current layers resulting from the ideal nonlinear evolution are located in different regions of the loop.

Reconnection starts influencing those magnetic lines that go through the current layer and therefore changes the connectivity of those fluid elements at the photosphere where such lines originate. Away from the current layer the lines are frozen and move with the local velocity of the fluid.

In the case of model FC1 magnetic lines are affected by reconnection in both legs of the loop and the kink progressively involves field lines at greater and greater distances from the axis of the loop. As a result lines with an originally small amount of twist are connected with lines originally in the potential region of the loop with a much greater twist and eventually the original magnetic field topology is completely destroyed, leading to what appears to be an ergodic field. We have not checked whether there are field lines that are actually space filling, or field lines that are totally disconnected from the photosphere, but an indication may be given by the behavior of the function $\alpha = \mathbf{j} \cdot \mathbf{B}/B^2$, which is a constant along field lines. Initially, this quantity is non-vanishing only within the current channel and monotonically decreasing outward (it does not depend on z). At saturation, this function appears to develop a plateau over the full extent of the perturbed region. At the same time, the field lines are clearly not the laminar constant α force-free field.

Models FC2 and NC develop a current layer at the loop apex and suffer a less extended kink instability. In the NC case the kink is totally confined within the current channel and the original potential field contains no twist. For model

Solanki et al. (1993). According to Hagyard et al. (1983) and others, the observed vertical field gradient ranges from 0.2 G km^{-1} to several G km^{-1} (for reference see Balthasar & Schmidt 1993). Hagyard et al. (1983) suggest 0.2 G km^{-1} , while Balthasar & Schmidt (1993) suggest $2\text{--}3 \text{ G km}^{-1}$ and Pahlke & Wiehr (1990), 2 G km^{-1} . Balthasar & Schmidt (1993) obtained the nearly independent vertical field gradient on location within a sunspot. In the present study, we have considered four different cases: $dB_Z/dZ = 0 \text{ G km}^{-1}$, 0.5 G km^{-1} , 1 G km^{-1} , and 2 G km^{-1} . By virtue of equations (9) and (11), the longitudinal field configuration referenced to a common geometrical depth ($Z = Z_D$) can be obtained by

$$B_Z(R, Z_D) = B_Z(\alpha) + \Delta Z(\alpha)(dB_Z/dZ). \quad (12)$$

Here we express our new shape function as

$$D(\alpha) = D(0) \exp(-\alpha^n) = D(0) \exp[-(\alpha_p R/R_p)^n], \quad (13)$$

where n and α_p are free parameters that will be chosen to fit $D(\alpha)/D(0)$ to the derived $B_Z(R, Z_D)/B_Z(0, Z_D)$ through equation (2). The old shape function is a Gaussian ($n = 2$) with $\alpha_p = 1.63$, which was inferred from the longitudinal field configuration referenced to optical depth. Since we have converted the magnetic field distribution referenced to optical depth to one referenced to geometrical depth, we have to derive new shape functions that will conform to the new prescription. For this work we generalize the shape function to that given by equation (13). This corresponds to an improvement of the upper boundary condition of Yun's sunspot models.

A set of the two numerical parameters n and α_p has been determined by means of nonlinear least-squares fitting for each of the four different cases considered above. The resulting values are tabulated in the third and fourth columns of Table 1. In the table we may note that case 1 (zero field gradient) is very similar to the old one chosen by Yun (1968). The total flux Φ and the parameter f conforming to the newly derived shape function have been estimated by numerically solving equations (3) and (5). We define A and C as $A = f/D(0)$ and $C = \Phi/\pi D(0)$ and list the resulting values of A and C for the four cases in Table 1. Finally, the radial component of the field $B_R(R, Z_D)$ is computed from

$$B_R(R, Z_D) = \alpha D(\alpha)(d\xi/dZ)_{Z_D} \\ = \exp[-(\alpha R/R_p)^n](\tan \psi_p)(\alpha/\alpha_p).$$

2.3. Boundary Condition

The upper boundary condition is a free parameter, which can be specified by the inclination angle ψ_p at the outer edge of the penumbra at a given geometrical depth Z_D . The

upper boundary condition is given by

$$y'(Z_D) = \frac{y^2(Z_D)}{[D(0)]^{1/2}} \frac{\tan \psi_p}{\alpha_p}, \quad (15)$$

where Z_D is taken as the depth of $\tau = \frac{2}{3}$ at the sunspot center and ψ_p is the angle of inclination of a line of force passing through the outer edge of the penumbra at the geometric depth Z_D . The value of ψ_p here should be smaller than the observed angle of inclination at the outer edge of the penumbra. However, Yun (1970) neglected the Wilson effect and made use of values based on the observations. The $\psi_{p\max}$ in Table 1 is the upper limit of ψ_p , below which no off-centered local maximum of the total field strength is found. For all cases, the values of $\psi_{p\max}$ are smaller than the observed inclination angle $\psi_{\text{obs}}(0)$.

3. RESULT AND DISCUSSION

With the new shape functions derived in the previous section (see Table 1), four sets of magnetostatic sunspot models with $T_{\text{spot}} = 4000 \text{ K}$ and 4400 K have been constructed, in each of which ψ_p is varied to fit the observations. In Figure 2, the field strengths at the spot axis computed for three values of ψ_p are compared with the observed ones (*solid line*) determined by the empirical relation (eq. [6]). As can be seen from the figure, the computed field strengths match well the observed one for a particular ψ_p , which is named as the most desirable one. We tabulate the most desirable ψ_p in Table 1 for comparison with the upper limit angle $\psi_{p\max}$. As can be seen in Table 1, the most desirable ones of all cases, except for case 1 (zero field gradient), do not exceed the upper limit $\psi_{p\max}$, beyond which the off-centered maximum field strength begins to show up. It implies that the shortcomings of Yun's model do not appear in the computed models since the upper boundary condition is different from that of Yun (1970) by taking into account the Wilson effect. In addition, the determination of the most desirable value of ψ_p for a assumed field gradient results in the models that are essentially characterized only by the effective temperature T_{spot} at the spot axis. This makes it possible to investigate the dependence of the physical characteristics of model spots on T_{spot} and/or on the spot size. The physical characteristics of the computed model sunspots are summarized in Table 2, which are specified by the most desirable $\psi_p = 50^\circ, 63^\circ, 67^\circ, 71^\circ$, and $T_{\text{spot}} = 4000 \text{ K}, 4400 \text{ K}$, respectively. As can be seen in Table 2, thermodynamic parameters P_g and ρ depend only on the thermal structures of model spots.

So far, the vertical field gradient has been assumed to be independent of the position within a sunspot. In order to examine the radial dependence effect of the magnetic field

TABLE 1
MODEL PARAMETERS ESTIMATED FOR DIFFERENT VERTICAL FIELD GRADIENTS

Model	dB_Z/dZ (G km^{-1})	n	α_p	A	C	$\psi_{p\max}$ (deg)	ψ_p (Z_D) (deg)	ψ_{obs} (0) (deg)
Yun	0	2.00	1.63	0.50	1.00	66.5
Case 1	0	1.86	1.63	0.49	1.03	69.1	71	72
Case 2	0.50	1.65	1.43	0.48	1.11	68.7	67	72
Case 3	1.00	1.49	1.22	0.47	1.19	66.8	63	72
Case 4	2.00	1.24	0.81	0.47	1.44	58.6	50	72
Case 5	$-0.5\alpha + 1$	1.70	1.39	0.48	1.09	67.6	67	72

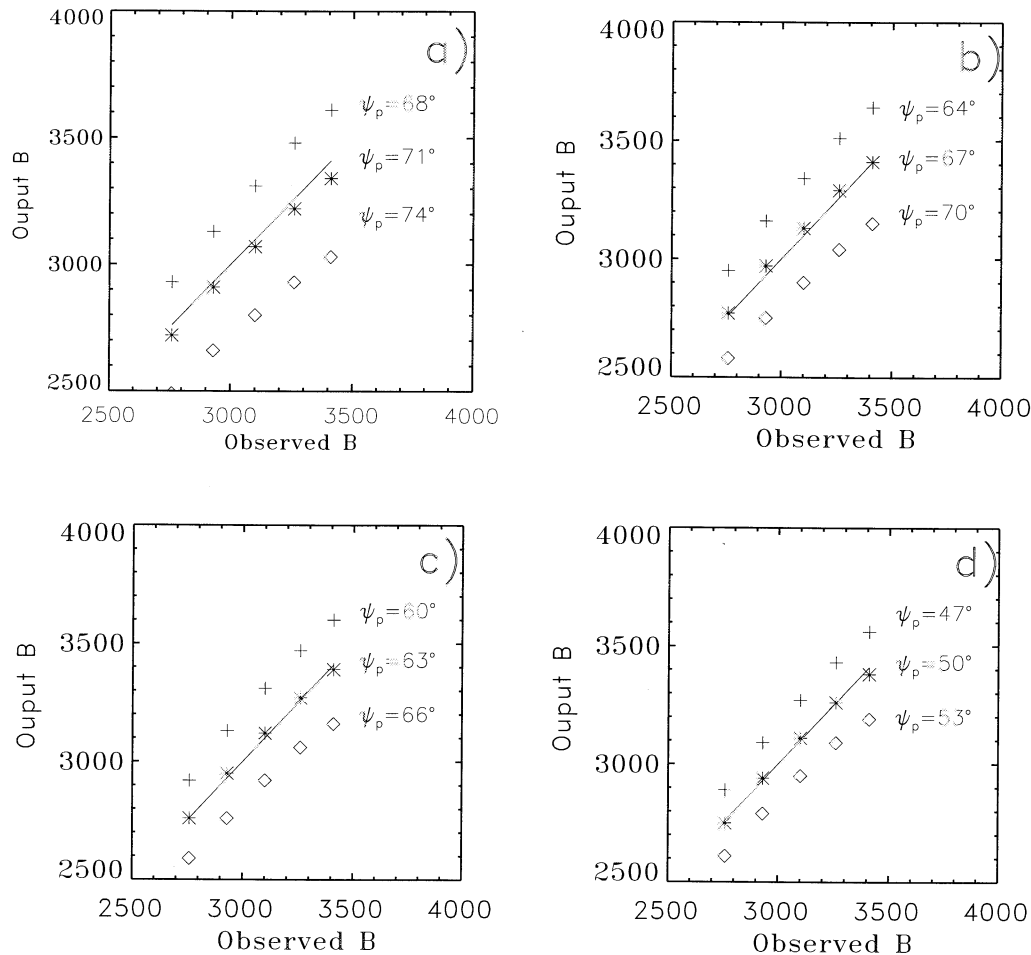


FIG. 2.—Computed maximum field strengths (points) at the photosphere of sunspots vs. the observed ones (solid line) given by eq. (6). $dB_z/dZ =$ (a) 0 G km^{-1} , (b) 0.5 G km^{-1} , (c) 1 G km^{-1} , and (d) 2 G km^{-1} . The two field strengths are consistent with each other for a particular ψ_p . Three ψ_p for each case are adopted for comparison.

gradient, we have taken a case characterized by

$$dB_z/dZ = -0.5\alpha + 1 \text{ G km}^{-1}, \quad (16)$$

where we assumed that the vertical field gradient decreases with the radial distance from the spot center. With a new shape function obtained from the field configuration characterized by equation (16), we have calculated the sunspot models by the same method as in the above four cases and included the results in the last rows of Tables 1 and 2. As seen from the tables, the physical characteristics of the computed models in case 5 are nearly similar to those of case 2,

where the vertical field gradient was taken as 0.5 G km^{-1} . This implies that ψ_p depends critically on the vertical gradient near the outer part of the penumbra.

Figure 3 shows the field distribution of the radial, vertical, and total magnetic field strengths at the depth of Z_d calculated by using new shape functions and equation (14) for four different field gradients ($0.5, 1, 2, -0.5\alpha + 1 \text{ G km}^{-1}$). Since the inclination angle of case 4 (Fig. 3c) changes too much from 50° at Z_d to 72° at $Z = 0$, it could not be compatible with the observation of deep sunspot penumbra (Solanki & Schmidt 1993). Among the con-

TABLE 2
PHYSICAL CHARACTERISTICS AT THE CENTER OF MODEL SUNSPOTS AT THE SURFACE Z_D

Model	T (K)	ψ_p (deg)	Φ (Mx)	B (G)	P_g (dynes cm^{-2})	ρ (g cm^{-3})	$(dB/dZ)_c$ (G km^{-1})	R_p (Z_D) (arcsec)
Case 1.....	4000	71	2.4E22	3337	1.99E5	7.86E-7	0.79	33.5
	4400	71	5.6E21	2720	1.73E5	6.22E-7	1.20	17.9
Case 2.....	4000	67	2.4E22	3406	1.99E5	7.86E-7	0.79	28.0
	4400	67	5.6E21	2774	1.73E5	6.22E-7	1.20	15.0
Case 3.....	4000	63	2.4E22	3387	1.99E5	7.86E-7	0.79	23.2
	4400	63	5.6E21	2759	1.73E5	6.22E-7	1.20	12.4
Case 4.....	4000	50	2.4E22	3377	1.99E5	7.86E-7	0.79	14.0
	4400	50	5.6E21	2759	1.73E5	6.22E-7	1.20	7.5
Case 5.....	4000	67	2.4E22	3374	1.99E5	7.86E-7	0.79	27.6
	4400	67	5.6E21	2748	1.73E5	6.22E-7	1.20	14.8

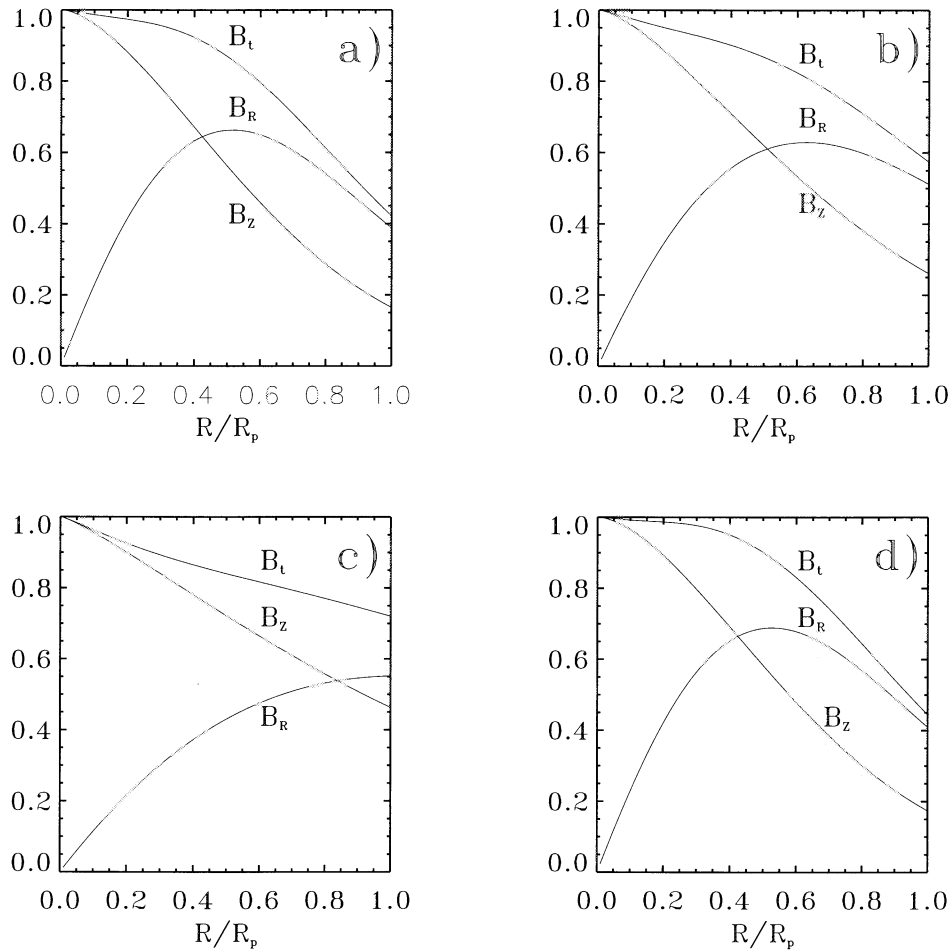


FIG. 3.—Magnetic field configuration characterized by new shape functions and the most desirable ψ_p (see Table 1). The most desirable ψ_p was determined by comparing the computed field strengths with the observed ones. $dB_z/dZ = (a) 0.5 \text{ G km}^{-1}$, $(b) 1 \text{ G km}^{-1}$, $(c) 2 \text{ G km}^{-1}$, and $(d) -0.5\alpha + 1 \text{ G km}^{-1}$.

sidered models, cases 3 and 5 seem to be the most self-consistent model in the sense that the resulting $(dB/dZ)_c$ ($0.8\text{--}1.2 \text{ G km}^{-1}$) comes out closer to the assumed vertical field gradient of 1 G km^{-1} . Considering the recent observation by Bruls et al. (1995), who found that the vertical gradient of magnetic fields in the penumbra slowly declines as a function of radial distance, we suggest that case 5 should be a most reasonable one. It is noted that the computed $d\psi_p/dZ$ ranges from 0.01 km^{-1} to 0.03 km^{-1} at the outer edge of the penumbra, which falls within the range suggested by Solanki et al. (1993).

Finally, we note that in our model the amount of the Wilson depression appears to have a linear relationship with $T_{\text{spot}}/T_{\text{ph}}$ and $T_{\text{spot}}/T_{\text{ph}}$ can be related to R_u , a directly observable quantity with the use of equations (6) and (7). In Figure 4 we plot the Wilson depression calculated from models as a function of R_u to get their linear relationship as

$$\text{WD(km)} = 26.4R_u[\text{arcsec}] + 356.2 \quad (17)$$

for $R_u > 7''$. We suggest this model-predicted relation could be tested by high-resolution observation in the future. The amount of the Wilson depression we presented in Figure 4 lies within the range of those suggested by Solanki et al. (1993) and Gokhale & Zwaan (1972).

The self-similarity assumption by ST58 is adopted in our study to make the problem mathematically tractable. There

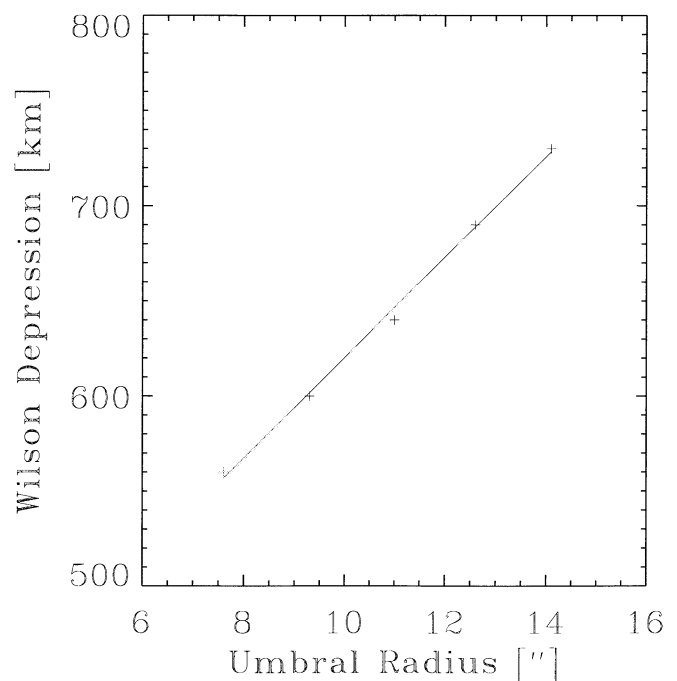


FIG. 4.—Computed Wilson depression as a function of the umbral size. Crosses are the computed values, and the solid line is their linear regression.

is no known physical reason for the sunspot field configuration to be self-similar. However, we can at least assert that the self-similarity, if any, can hold only in the region of high plasma β , where the plasma pressure can confine the magnetic field. So far no direct measurement of the subphotospheric field configuration has been made. Lee et al. (1993) investigated the radial magnetic field structure of a single isolated sunspot at the coronal base using microwave spectroscopy. They showed that the radial field distribution, at least inside the inner penumbra, has a Gaussian form and is very similar to that in the photosphere. If the field configuration is more or less self-similar even above the photosphere, we may expect that it would be more so in the subphotospheric region.

In the present study, we have not made a closer examination of the optical properties of the models. A continuum radiative transfer analysis of the emergent flux at various center-to-limb angles would give us a more definitive understanding of the Wilson effect. However, it is beyond the scope of this paper and is reserved for future studies.

The sunspot models in this study are constructed under the assumption of the azimuthal symmetry. Title et al. (1993) found from their high-resolution observations at the Swedish Solar Observatory in La Palma that the inclination angle of the magnetic field in the penumbra of sunspots oscillates rapidly with azimuth. In relation to this, Martens et al. (1996) presented a constant- α force-free model for the magnetic field in fluted sunspots. Our symmetric models do not accommodate any azimuthal variations, but are mainly concerned with the mean-field structure of isolated sunspots, especially in the high- β region in and below the photosphere.

4. SUMMARY AND CONCLUSION

In the present study, we have revisited Yun's sunspot models by taking into account the effect of the Wilson depression. For this purpose, we represented the observed field distribution of sunspots with the Skumanich dipole model and converted it to one referenced to a common geometric depth. In converting the Skumanich dipole model to the geometrically referenced one, we have made use of the radial dependence of the Wilson depression suggested by Solanki et al. (1993). With the use of the Wilson depression of Solanki et al. (1993) along with five different vertical gradients (0, 0.5, 1.0, 2.0, and $-0.5\alpha + 1 \text{ G km}^{-1}$), a set of new shape functions has been derived by fitting them to the geometrically referenced longitudinal field distributions. The shape functions are assumed to be represented by $D(\alpha) = D(0) \exp(-\alpha^n)$. To reduce the number of free parameters in the model computations, we have utilized a recent

empirical relation between maximum field strength and effective temperature of spots given by Kopp & Rabin (1992), together with the relation between the field strength and the umbral size suggested by Kopp & Rabin (1992) and Martinez Pillet & Vázquez (1993). With the new shape functions conforming to geometrically referenced field configurations characterized by the five different vertical field gradients, five sets of magnetostatic sunspot models have been computed by varying ψ_p .

The main result in this study is summarized as follows:

1. The computed models for a given field gradient can be characterized only by T_{spot} , the effective temperature at the center of spots. The most desirable values of ψ_p , the upper boundary condition, for the five different cases were determined by comparing the computed maximum surface field strengths with the observed ones.
2. Especially, the computed models do not have the shortcoming raised by Osherovich (1982), demonstrating that the shortcoming is not inherent to the self-similar models. The similarity assumption would break down in the higher solar atmosphere due to the surrounding weak gas pressure as commented by Steiner, Pneuman, & Stenflo (1986) and Pneuman, Solanki, & Stenflo (1986).
3. The resulting sunspot models support the observed empirical relations given by Kopp & Rabin (1992) and Martinez Pillet & Vázquez (1993).
4. The computed $d\psi_p/dZ$ ranges from 0.01 to 0.03 km^{-1} at the outer edge of the penumbra, which falls within the range suggested by Solanki et al. (1993).
5. The present study supports the self-similarity for the lateral magnetic vector structure of fairly isolated sunspots found by Keppens & Martinez Pillet (1996).

We presented in Table 2 the physical characteristics of T , ψ_p , Φ , B , P_g , ρ , $(dB/dZ)_c$, and $R_p(Z_D)$ expected in each model. It is concluded that when the Wilson depression is properly taken into account, the similarity field configuration represents quite well the structure of subphotospheric sunspots.

We wish to thank A. Skumanich, J. W. Lee, and G. S. Choe for reading the manuscript and providing valuable comments. We also appreciate the anonymous referee's helpful comments for improving the present paper. The present work is in part supported by the Basic Research Institute Program, Ministry of Education, Republic of Korea, 1996 (BSRI-96-5408) and in part by the Korea-China Cooperative Science Program, under grant (966-0203-005-2). Y.-J. Moon is very thankful for support of KAO (Korea Astronomy Observatory) Research Fund.

REFERENCES

- Adam, M. G. 1990, *Sol. Phys.*, 125, 137
 Balthasar, H., & Schmidt, W. 1993, *A&A*, 279, 243
 Bruls, J. H. M. J., Solanki, S. K., Rutten, R. J., & Carlsson, M. 1995, *A&A*, 293, 225
 Deinzer, W. 1965, *ApJ*, 141, 548
 Flå, T., Osherovich, V. A., & Skumanich, A. 1982, *ApJ*, 261, 700
 Gokhale, M., & Zwaan, C. 1972, *Sol. Phys.*, 26, 52
 Hagyard, M. J., et al. 1983, *Sol. Phys.*, 84, 13
 Keppens, R., & Martinez Pillet, V. 1996, *A&A*, 270, 494
 Kopp, G., & Rabin, D. 1992, *Sol. Phys.*, 141, 253
 Lee, J. W., Gary, D. E., Hurford, G. J., & Zirin, H. 1993, in *ASP Conf. Ser.* 46, *The Magnetic and Velocity Fields of Solar Active Regions*, ed. H. Zirin, G. Ai, & H. Wang (San Francisco: ASP), 287
 Lites, B. W., Elmore, D. F., Seagraves, P., & Skumanich, A. 1993, *ApJ*, 418, 928
 Martens, P. C. H., Hulburt, N. E., Title, A. M., & Acton, L. W. 1996, *ApJ*, 463, 372
 Martinez Pillet, V., & Vázquez, M. 1993, *A&A*, 270, 494
 Osherovich, V. A. 1982, *Sol. Phys.*, 77, 63
 Osherovich, V. A., & Garcia, H. A. 1989, *ApJ*, 336, 468
 Pahlke, K. D., & Wiehr, E. 1990, *A&A*, 238, 246
 Pneuman, G. W., Solanki, S. K., & Stenflo, J. O. 1986, *A&A*, 154, 231
 Schlüter, A., & Temesvary, S. 1958, in *IAU Symp. 6, Electromagnetic Phenomena in Cosmical Physics* (Cambridge: Cambridge Univ. Press), 263 (ST58)
 Skumanich, A. 1992a, in *Sunspots*, ed. J. H. Thomas & N. O. Weiss (Dordrecht: Kluwer), 121
 Skumanich, A. 1992b, in *Surface Inhomogeneities on Late Type Stars*, ed. P. B. Byrne & D. J. Mullan (Berlin: Springer), 90
 Solanki, S. K., Ruedi, I., & Livingston, W. 1992, *A&A*, 263, 339

REPORT DOCUMENTATION PAGE			Form Approved OMB No. 0704-0188	
Public reporting burden for this collection of information is estimated to average 1 hour per response, including the time for reviewing instructions, searching existing data sources, gathering and maintaining the data needed, and completing and reviewing the collection of information. Send comments regarding this burden estimate or any other aspect of this collection of information, including suggestions for reducing this burden, to Washington Headquarters Services, Directorate for Information Operations and Reports, 1215 Jefferson Davis Highway, Suite 1204, Arlington, VA 22202-4302, and to the Office of Management and Budget, Paperwork Reduction Project (0704-0188), Washington, DC 20503.				
1. AGENCY USE ONLY (Leave blank)	2. REPORT DATE June 19, 1998	3. REPORT TYPE AND DATES COVERED Interim for 7/16/97 - 6/15/98		
4. TITLE AND SUBTITLE The Structure and Dynamics of the Solar Corona - NASA Space Physics Theory Contract NAS5-96081 - Second Year Progress Report		5. FUNDING NUMBERS C-NAS5-96081 PR-01-0157-07-7650-000		
6. AUTHORS Zoran Mikic				
7. PERFORMING ORGANIZATION NAME(S) AND ADDRESS(ES) Science Applications International Corporation Mail Stop C2 10260 Campus Point Drive San Diego, CA 92121-1578		8. PERFORMING ORGANIZATION REPORT NUMBER SAIC-98/1032:APPAT-203		
9. SPONSORING/MONITORING AGENCY NAME(S) AND ADDRESS(ES) National Aeronautics & Space Administration Goddard Space Flight Center Greenbelt, MD 20771		10. SPONSORING/MONITORING AGENCY REPORT NUMBER		
11. SUPPLEMENTARY NOTES				
12a. DISTRIBUTION/AVAILABILITY STATEMENT		12b. DISTRIBUTION CODE		
13. ABSTRACT (Maximum 200 words) This report details progress during the second year of funding for our Space Physics Theory contract.				
14. SUBJECT TERMS solar corona magnetohydrodynamics numerical simulation active regions		15. NUMBER OF PAGES 16		
		16. PRICE CODE		
17. SECURITY CLASSIFICATION OF REPORT UNCLASSIFIED	18. SECURITY CLASSIFICATION OF THIS PAGE UNCLASSIFIED	19. SECURITY CLASSIFICATION OF ABSTRACT UNCLASSIFIED	20. LIMITATION OF ABSTRACT UL	